To the Graduate Council:
I am submitting herewith a dissertation written by Hui Liu entitled "Development of A Soft Robotic Approach for An Intra-abdominal Wireless Laparoscopic Camera." I have examined the final paper copy of this dissertation for form and content and recommend that it be accepted in partial fulfillment of the requirements for the degree of Doctor of Philosophy, with a major in Mechanical Engineering.

Jindong Tan, Major Professor

We have read this dissertation
and recommend its acceptance:

Committee Member 1

Committee Member 2

Committee Member 3

Accepted for the Council:

Dixie Thompson

Vice Provost and Dean of the Graduate School

To the Graduate Council:
I am submitting herewith a dissertation written by Hui Liu entitled "Development of A Soft Robotic Approach for An Intra-abdominal Wireless Laparoscopic Camera." I have examined the final electronic copy of this dissertation for form and content and recommend that it be accepted in partial fulfillment of the requirements for the degree of Doctor of Philosophy, with a major in Mechanical Engineering.

Jindong Tan, Major Professor

We have read this dissertation
and recommend its acceptance:

Committee Member 1

Committee Member 2

Committee Member 3

Accepted for the Council:

Dixie Thompson

Vice Provost and Dean of the Graduate School

(Original signatures are on file with official student records.)

Development of A Soft Robotic Approach for An Intra-abdominal Wireless Laparoscopic Camera

A Dissertation Presented for the

Doctor of Philosophy

Degree

The University of Tennessee, Knoxville

Hui Liu

August 2023

© by Hui Liu, 2023
All Rights Reserved.

I dedicate this dissertation to my parents, Peicheng Liu and Liqin Guo, and my wife, Wenqi Wang.

Acknowledgements

I would like to express my deepest gratitude and appreciation to all those who have supported me during my Ph.D. research. Their encouragement, guidance, and unwavering belief in my abilities have been invaluable, and I am truly grateful for their contributions. I extend my heartfelt appreciation to my advisor, Dr. Jindong Tan, for his exceptional expertise, dedication, and mentorship throughout the research process. His unwavering support and constructive feedback have been instrumental in shaping my work. I would like to thank my dissertation committee, Dr. Jeffrey Reinbolt, Dr. Subhadeep Chakraborty and Dr. Shuai Li for their valuable insights and critical evaluation. Their expertise and guidance have contributed significantly to the quality of my research. I extend my appreciation to my fellow lab members: Dr. Ning Li, Dr. Xiaolong Liu and Dr. Yan Li for their willingness to contribute their time and expertise, which has greatly enhanced the depth and validity of my research. To my family, I express my deepest gratitude for their unwavering support and belief in my abilities. Their love and encouragement have been my constant motivation throughout this challenging endeavor. Lastly, I acknowledge the influential work of countless authors, researchers, and scholars that has shaped my understanding and inspired my research. To all those mentioned above and to everyone else who has played a part in my academic journey, I offer my deepest gratitude. Your support and contributions have been instrumental in the successful completion of my PhD dissertation.

Abstract

In Single-Incision Laparoscopic Surgery (SILS), the Magnetic Anchoring and Guidance System (MAGS) arises as a promising technique to provide larger workspaces and field of vision for the laparoscopes, relief space for other instruments, and require fewer incisions. Inspired by MAGS, many concept designs related to fully insertable magnetically driven laparoscopes are developed and tested on the transabdominal operation. However, ignoring the tissue interaction and insertion procedure, most of the designs adopt rigid structures, which not only damage the patients' tissue with excess stress concentration and sliding motion but also require complicated operation for the insertion. Meanwhile, lacking state tracking of the insertable camera including pose and contact force, the camera systems operate in open-loop control. This provides mediocre locomotion precision and limited robustness to uncertainties in the environment.

This dissertation proposes, develops, and validates a soft robotic approach for an intra-abdominal wireless laparoscopic camera. Contributions presented in this work include (1) feasibility of a soft intra-abdominal laparoscopic camera with friendly tissue interaction and convenient insertion, (2) six degrees of freedom (DOF) real-time localization, (3) Closed-loop control for a robotic-assisted laparoscopic system and (4) untethering solution for wireless communication and high-quality video transmission. Embedding magnet pairs into the camera and external actuator, the camera can be steered and anchored along the abdominal wall through transabdominal magnetic coupling. To avoid the tissue rapture by the sliding motion and dry friction, a

wheel structure is applied to achieve rolling motion. Borrowing the ideas from soft robotic research, the main body of the camera implements silicone material, which grants it the bendability to passively attach along the curved abdominal wall and the deformability for easier insertion. The six-DOF pose is estimated in real-time with internal multi-sensor fusion and Newton-Raphson iteration. Combining the pose tracking and force-torque sensor measurement, an interaction model between the deformable camera and tissue is established to evaluate the interaction force over the tissue surface. Moreover, the proposed laparoscopic system is integrated with a multi-DOF manipulator into a robotic-assisted surgical system, where a closed-loop control is realized based on a feedback controller and online optimization. Finally, the wireless control and video streaming are accomplished with Bluetooth Low Energy (BLE) and Analog Video (AV) transmission. Experimental assessments have been implemented to evaluate the performance of the laparoscopic system.

Table of Contents

1 Introduction **1**

1.1 Minimally Invasive Surgery 1

1.2 State of the Art 3

1.3 Research Objectives 6

1.4 Challenges 7

1.4.1 Mechanical and Actuation Design 8

1.4.2 Real-time Pose Tracking 9

1.4.3 Camera-tissue Interaction 10

1.5 Contributions 11

1.5.1 Feasibility of A Novel Soft Intra-abdominal Laparoscopic Camera 11

1.5.2 Six-DOF Real-time Localization 12

1.5.3 Closed-loop Control for A Robotic-Assisted Laparoscopic System 13

1.5.4 Untethering Solution for Control Communication And High-Quality Video Transmission 14

1.6 Dissertation Outline 15

2 Design of the Soft Wheeled Structure **16**

2.1 Introduction 16

2.2 System Mechanical Design 19

2.2.1 System Overview 19

2.2.2 Design of The Intra-abdominal Wireless Laparoscope 21

2.3 Working Principle of the Magnetic-driven Laparoscope 25
2.3.1 Intra-abdominal locomotion 25
2.3.2 Insertion Procedure 27
2.4 Modeling of Bendability 29
2.5 Prototype Fabrication 33
2.6 Experiments and Results 35
2.6.1 Experimental setup 35
2.6.2 Result Analysis 38
2.7 Discussion and Conclusion 44

3 Magnetic Localization for the Wireless Laparoscopic Camera 46
3.1 Introduction 46
3.2 System Overview And Operation Principle 50
3.2.1 Design of the Intra-abdominal Wireless Laparoscope 50
3.2.2 Magnetic Actuation and Localization Principle 53
3.3 MODELING APPROACH 56
3.3.1 Coordinate frame and kinematic modeling 57
3.3.2 Modeling of Forward Magnetic Relationship 62
3.4 Localization Algorithm for the Wireless Laparoscope 63
3.4.1 Madgwick Complementary Filter 65
3.4.2 Inverse Mapping Based-on Newton-Raphson 68
3.5 EXPERIMENT AND RESULT 70
3.5.1 Platform Overview 70
3.5.2 Magnetic Relationship Evaluation 70
3.5.3 Localization Algorithm Assessment 74
3.6 CONCLUSIONS and FUTURE WORK 76

4 Robotic-Assisted Control of the Wireless Magnetic Laparoscopic System 77
4.1 Introduction 77

4.2 Tissue-Camera Interaction Model . . . 80
4.2.1 Modeling of the Multi-layer Abdominal Wall Tissue . . . 81
4.2.2 Contact and Interaction Model . . . 81
4.3 Closed-loop Control . . . 86
4.4 Experiments and Result . . . 88
4.5 Summary and Conclusion . . . 88

5 Tetherless Vision and Control for Insertable Laparoscopic Cameras 91
5.1 Introduction . . . 91
5.2 Electronic Hardware . . . 92
5.2.1 Electronic System Architecture Overview . . . 92
5.2.2 Internal Camera Board Design and Implementation . . . 92
5.2.3 External Actuator Board Design and Implementation . . . 98
5.3 Software . . . 101
5.3.1 Bluetooth Low Energy (BLE) Communication and Profile . . . 101
5.3.2 Architecture and Implementation of Real-Time Operating System (RTOS) . . . 103
5.4 Experiment Validation . . . 106
5.4.1 Wireless Communication . . . 106
5.4.2 Video Transmission . . . 106
5.5 Summary . . . 108

6 Conclusions and Future Work 110
6.1 Conclusions . . . 110
6.2 Future Work . . . 111

Bibliography 114

Vita 127

List of Tables

2.1 Notations for Bendability Modeling 30

3.1 Notations for Pose Estimation Modeling 58

3.2 Distribution of the Relative Error from the Forward Mapping Model . 73

List of Figures

1.1 Minimally invasive laparoscopic surgery 2
1.2 Multiple-port and single-port minimally invasive surgeries 2
1.3 Magnetic Anchoring and Guidance System (MAGS) 4
1.4 Start-of-the-art insertable laparoscopic camera prototypes 4

2.1 The proposed wireless laparoscopic camera works as a subsystem of the robotic surgical assistant system, including an external actuator and in vivo camera module. Made with soft material, the camera can passively bend along the abdominal wall to relief the stress on tissue. 20
2.2 Assembly exploded view of the actuator and the camera. The system design is based on double pairs of magnets, which provide stronger and stabler coupling than a single-magnet pair design. 22
2.3 The layout of the camera shows the combination of soft material and wheeled structure design. 22
2.4 The comparison between vertical layout and horizontal layout. The horizontal layout grants a larger field of view, stronger magnetic coupling, smaller diameter design, and stable panning motion free from singularity. 24
2.5 Rolling motion with wheel structure design. This feature transfers the sliding motion into rolling motion when the camera is translating along y_c and tilting around x_c. The dry friction between the camera and tissue is also replaced with ignorable rolling friction. 24

2.6 Intra-abdominal magnetic actuation principle. The camera has 4-DOF including 2-DOF translation, tilt, and pan. In the tilt motion, The coupling pairs from left to right show the tilting sequence from $+90°$ to $-90\circ$. Since the magnetic moment of IPMs always follows the magnetic moment of EPMs, the relationship between EPM tilt angle θ_E, IPM tilt angle θ_i and horizontal shift δ_s can be easily modeled. 26
2.7 The insertion procedure is challenging for existing rigid designs. a) During the insertion of the camera through the trocar, the magnetic coupling becomes weaker as the distance between the EPM and IPM increases. b) When the camera is totally inserted, the left end of the camera tends to impact the tissue while the right end turns to fall. . . 28
2.8 The simplified insertion procedure with soft structure design. a) During the insertion of the camera through a trocar, the distance between the EPM and IPM is almost constant, and the magnetic coupling is maintained stably. b) When the camera is almost totally inserted, the actuator rotates around the coupling end and establishes the coupling on the other end. 28
2.9 Loading diagram of the camera 30
2.10 Loading diagram of the soft shaft and the soft tube. 30
2.11 The prototyped actuator and camera. 34
2.12 Each mold contains three pieces, in which the bottom two pieces shape the external profile, and the top piece extrudes the internal cavity. . . 34

2.13 **a** The left figure shows the panning and tilting test. In the right figure, the belly model was separated into four regions, and the duration of the steering camera to the four regions was recorded. **b** The soft camera model (left) can bend along the curved tissue, while the rigid camera model (right) creates obvious stress concentration. **c** Our soft camera and a rigid mock-up camera were placed on the belly model to measure the pressure. Two regions with different curvatures were picked. **d** The bendability of the camera was validated by applying magnetic force, which helps plan the insertion procedure and optimize the camera design. **e** The camera was inserted through the trocar fixed with 20°. Ten trials were recorded. 36

2.14 **a** The camera has the pan motion of ±90°. The bottom-left insets indicated the images captured by the camera. **b** The camera is capable of achieving ±90° continuous tilt motion. Typically, the camera is able to observe the entire surgical scene within ±60° of tilt movement. Images taken were provided in the corner insets. **c** The camera is driven from the center to four regions and provides desired FOV. The operation time is recorded. The insets at four corners show the recorded images. **d** Box plot presenting operation time used to assess dexterity of navigation. 39

2.15 **a** Simulation comparison between soft and rigid designs in Ansys workbench. The contact area has a significant difference between the two cases. **b** Maximum stress comparison between soft and rigid designs in simulations. **c** Software client for visualizing the pressure data collected by pressure mapping sensor. **d** Pressure comparison between soft and rigid designs in different curvature cases. 41

2.16 Bendability test results were shown in (b). The attraction force and bending angle pairs were inserted at the corners. The relationship can be fitted with a linear function. 43

2.17 The four main steps of the insertion procedure were recorded. The average duration for each step is shown in the time bar. 43

3.1 Overview of a robotic surgical system. The proposed wireless laparoscopic camera works as a subsystem including an external actuator and an in vivo camera module. 51

3.2 Magnetic-based actuation and localization mechanism. The camera has 4-DOF including 2-DOF translation, tilt, and pan. The IMU is used for tracking the pitch and roll angles of the camera with respect to the world frame. Subtracting the effects from the IPMs, the MAG collects the magnetic fields B_1 and B_2 due to the EPMs. 54

3.3 Coordinate frames of the system. World frame $\{w\}$ coincides with the base frame of the manipulator, $\{a\}$, $\{c\}$ and $\{m\}$ represent the actuator, camera and MAG center frame. The poses are expressed by p_a^w, p_c^w, p_m^w, and Euler angles. Frame $\{m\}$ is fixed on the center line of the camera and has the same orientation as $\{c\}$. 58

3.4 Block diagram of proposed localization method. 64

3.5 Overview of the system. (a) and (b) display the assembled camera module and the external actuator. (c) and (d) show the details of each module including the camera board built around a Bluetooth chip, the location of two pairs of magnets, and the micromotor controlling the tilt motion. (e) introduces the layout of the system for testing locomotion ability. 71

3.6 Experiment platform for evaluating localization method. The camera is fixed and calibrated at a known pose. Steering the actuator to move in the blue work region, MAG measurements are collected for evaluating the forward mapping model and the localization error. 71

3.7 Relative error map in layers based on different actuator-camera normal distance D. x and y axis represent the relative position between $\{m\}$ and $\{a\}$ with respect to $\{m\}$. 73
3.8 Error bar plot for the proposed localization method. Position errors on each axis and the yaw angle error are expressed in $\{b\}$. The whiskers represent the maximum and minimum errors, while the bars in the boxes account for average error. 75
3.9 Trajectory tracking of the actuator for evaluating the localization method. 3500 points are recorded for each test. The green points represent the estimated position. The red line shows the ground truth of the trajectory. The red arrows are the ground truth of the directions of y_a, while the blue arrows are the estimated results for the directions of y_a. 75

4.1 Mechanical modeling of multi-layer abdominal tissue with four serial Kelvin-Voigt models. From outside to inside, the four main layers are skin, fat, muscle, and peritoneum connective tissue. 82
4.2 Sectional view of the tissue-camera contact model. 82
4.3 Free body diagram of the camera capsule in contact with the abdominal wall. The reaction force is supposed to be the combination of the tissue membrane tension F_t, stress F_s from the viscoelastic tissue model, and viscous force F_v of peritoneum fluid covering the tissue. 84
4.4 Structure of robotic-assisted control. 87
4.5 Experimental platform for robotic-assisted control. 89

4.6 Trajectory tracking of the camera for evaluating the closed-loop control. 600 points are recorded for each test. In(a), the red line shows the desired trajectory. The blue line represents the measured result. In(b), The red line is the desired path in the $x - y$ plane. The measured trajectories are denoted in other colors including two forward paths and two backward paths. 89

5.1 Overview of the electronic system architecture. The subsystem above the abdominal wall is the external actuator, while the bottom part is the internal camera. Wireless links including the BLE communication (yellow) and the AV transmission (blue) are indicated with dashed lines. 93

5.2 Implementation and layout of camera onboard modules. 95

5.3 Implementation of the actuator board and AV receiver board 100

5.4 BLE profile and application flow chart. 102

5.5 Real time framework. 105

5.6 RSSIs with respect to actuator-camera distances. 107

5.7 Wireless imaging performance test. 107

Chapter 1

Introduction

1.1 Minimally Invasive Surgery

In Minimally Invasive Surgery (MIS), Surgeons make one or more small incisions on patients' abdominal walls, inserting surgical instruments along with tiny laparoscopic camera equipment through trocars (usually $5mm$ to $22mm$). It allows surgeons to manipulate the instruments to perform surgery while watching video streaming transmitted from the camera on a monitor. Compared with traditional open surgeries, MIS excels in small trauma and scar, mild postoperative pain, minimal anesthesia, quick recovery, and shorter hospital stay [1][2]. Fig. 1.1 shows an example of a Hysterectomy with the MIS technique.

Aiming to reduce the number of, or even eliminate incisions, single-incision laparoscopic surgery (SILS) [3][4] and natural orifice transluminal endoscopic surgery (NOTES) [5][6] has been introduced. Fig. 1.2 shows the comparison between the traditional multi-port MIS and SILS. In SILS, all the devices including the laparoscope are introduced through a single incision, which results in faster recovery and nearly invisible scarring. However, crowded through the same port, the maneuverability of the rigid long-stick instruments and laparoscope is constrained in a limited conical workspace, causing counter-intuitive operation and the loss of triangulation and

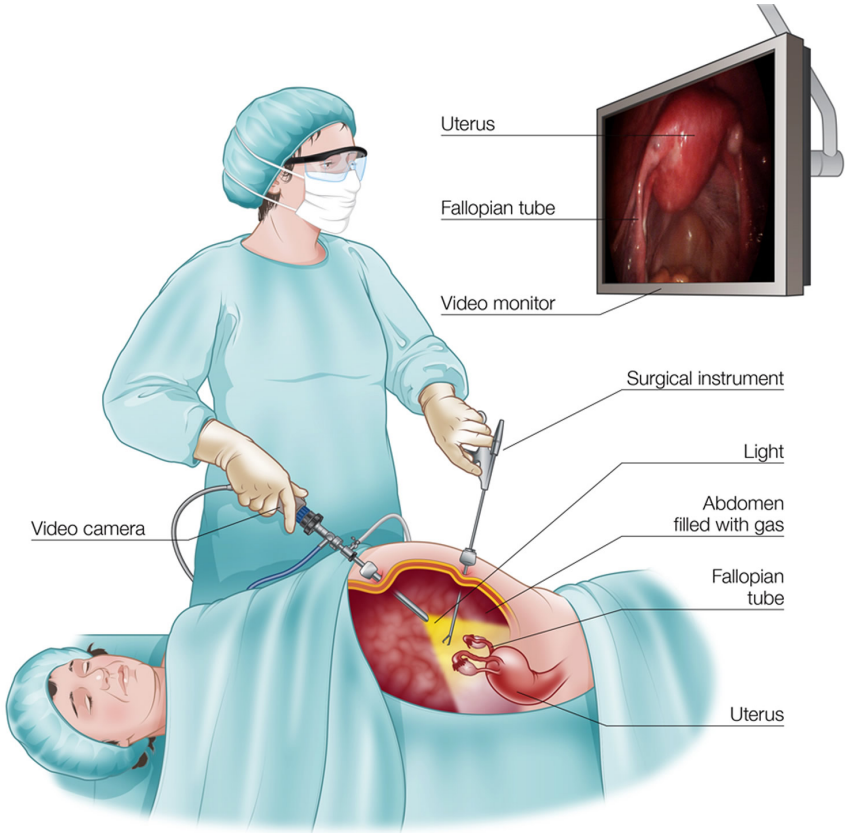

Figure 1.1: Minimally invasive laparoscopic surgery



(a) Multiple-port MIS **(b)** Single port MIS

Figure 1.2: Multiple-port and single-port minimally invasive surgeries

retraction. Consequently, it not only increases the complexity of operating surgical instruments but also hampers the field of view (FOV) of the laparoscopes.

Inspired by the concept of magnetic anchoring and guidance system (MAGS) proposed by Cadeddu [7], fully insertable laparoscopic camera systems emerged as a promising solution in SILS to relieve the problem. As illustrated in Fig. 1.3 Replacing the rigid links with magnetic coupling, the camera embedded with magnets is inserted completely into the patient's abdominal cavity, steered and anchored along the abdominal wall, locomoting in a larger workspace without occupying the entry port for other instruments [8][9].

1.2 State of the Art

Motivated by the concept of fully insertable laparoscopic devices, the current state of the art in laparoscopic camera prototypes can be categorized into different connection formats and actuation methods. These prototypes have shown potential in overcoming trocar constraints, minimizing surgical incisions, and reducing inter-device collisions. The evolution of these designs has progressed from tethered cable-driven devices to tethered devices with onboard motorized actuation, wireless devices with onboard motorized actuation, and tethered devices with pure magnetic actuation. Advancements have also been made towards pure magnetic anchoring/actuation and tetherless access, representing significant progress in the field.

In a study by Tognarelli [10], a cable-tethered endoluminal robotic platform for NOTES was developed and tested (Fig. 1.4a). The platform consisted of a miniaturized camera robot coupled with a reconfiguration anchoring frame driven by Shape Memory Alloy (SMA). The camera robot comprised roll and pitch modules joined together with passive camera support. Additional DOFs along the abdominal wall were achieved by dragging an external actuator with a set of external permanent magnets (EPMs). Another design by Rivas-Blanco [11] involved a magnetic intra-abdominal camera with two internal cable-driven DOFs (roll and tilt) based on

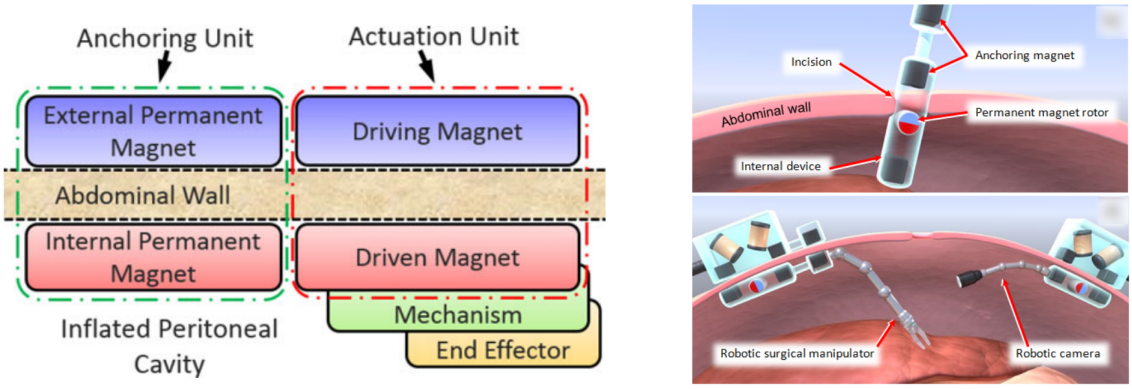

(a) Concept of MAGS [8] **(b)** Operation of MAGS [9]

Figure 1.3: Magnetic Anchoring and Guidance System (MAGS)

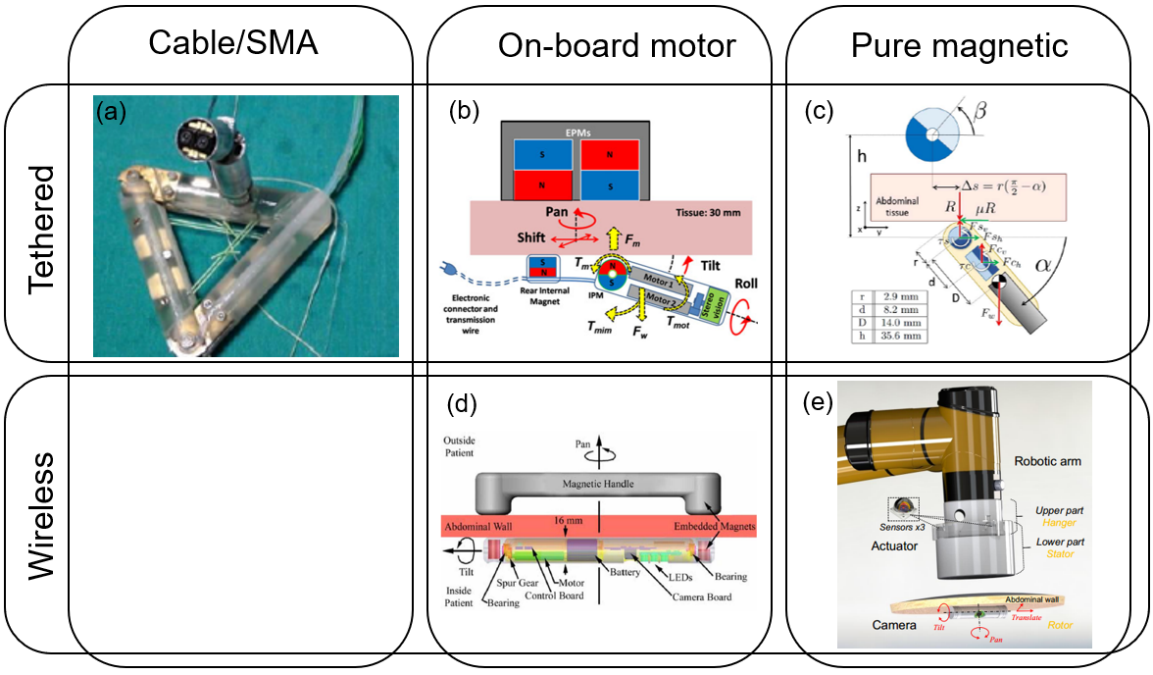

Figure 1.4: Start-of-the-art insertable laparoscopic camera prototypes

concentric mechanisms. To improve controllability and reduce the number of cables, onboard motors and peripheral mechanisms were integrated into the camera to manipulate its components. Simi [12] presented a wired and magnetically activated five-DOF camera robot with stereo vision (Fig. 1.4b). The rough pose of the camera could be determined by the external actuator with EPMs, while the internal motorized mechanism allowed fine tilt and roll adjustment.

However, these designs still required wires for the power supply, motor control, and video transmission, which introduced operational interference, pressure leakage, and dynamic disturbance. Recognizing the drawbacks of tethering wires, Platt et al. [13] proposed a wireless design of a wheeled ceiling pan/tilt robot with magnetic anchoring and improved motorized mobility (Fig. 1.4d). This platform required minimal physical connections to the camera, except for one small tether for video output. Nonetheless, the onboard motor increased the camera's weight and size, making manufacturing and assembly complex.

The work by Garbin and Valdastri [14][15] introduced a pure magnetic anchoring/actuation link for an insertable laparoscopic camera. This device, depicted in Fig. 1.4c, enables manual lateral translation and robotic tilt and pan motion using an orthogonal magnetic arrangement. The camera achieves a especially compact and light design by eliminating motors and complicated actuation mechanisms. However, a bundle of tethering wires is still required, which has been recognized as a common drawback due to operational interference [13][7]. Studies have reported that increasing the number of wires in the tether reduces its flexibility, thereby affecting the mobility of the tethered camera [16][17].

Recently, Li [18][19] proposed a tetherless insertable laparoscopic camera system called sCAM, which featured flexible in vivo mobility under pure magnetic anchoring/actuation. The system employed wireless video transmission and control communication, eliminating cumbersome tethering wires. However, the sliding motion and dry friction of the abdominal wall tissue resulted in creepy behavior that could potentially damage the tissue and complicate dynamic control modeling.

In summary, the trend in fully insertable camera robots is to adopt tetherless designs and pure magnetic actuation to avoid wire interference, achieve compactness, and reduce weight. Each solution partially met these expectations and enabled transabdominal operation and laparoscopic imaging. However, a notable drawback of existing camera systems is the lack of consideration for tissue-camera interaction. Research has shown the importance of preventing tissue overload and rupture [20]. The rigid structure design and actuation principle of current systems inevitably lead to tissue damage. Stress concentration occurs at both ends of the device, especially when anchored on a curved abdominal wall. Additionally, the sliding motion of the camera can cause tissue rupture due to dry friction. Insertion and extraction processes also pose challenges, often requiring assistance from specific tools or even another laparoscope. The development of a soft intra-abdominal camera with bendability and deformability deserves more investigation beyond the current state of the art. Furthermore, little research has been conducted on real-time spatial tracking and feedback control for these insertable laparoscopic devices, which are crucial challenges to address before these devices can be widely adopted in clinical practice.

1.3 Research Objectives

The main focus of this dissertation is to develop a soft intra-abdominal wireless laparoscopic camera system. The work aims to achieve the following four objectives:

The **first objective** is to design a novel soft robotic system that ensures friendly tissue contact and implements an intra-abdominal laparoscopic camera without physical links or tethering wires. The camera should be capable of being anchored, and steered using pure magnetic coupling from outside the patient's body. Additionally, the camera should be designed to avoid stress concentration and minimize dry friction. The other goal is to simplify the insertion procedure and enhance convenience for the surgeon.

The **second objective** is to enable real-time spacial tracking of the insertable laparoscopic camera, including its position and orientation. Accurate pose estimation of the camera is essential for closed-loop control, allowing for precise robotic manipulation and providing spatial information about the surgical environment.

The **third objective** is to develop a camera-tissue interaction model and integrate it with the pose tracking method to enable robotic-assisted closed-loop control of the in vivo laparoscopic camera. This closed-loop control system will provide surgeons with an intuitive interface, enhancing ergonomics, precision, and robustness in navigating the unstructured abdominal cavity. By automating low-level camera control tasks, surgeons can focus more on the surgical procedures themselves.

The **final objective** is to propose electronic and software solutions that facilitate high-quality tetherless streaming (HD1080p) and control communication. This involves designing an electronic system architecture based on Bluetooth Low Energy (BLE) profiles and analog video transmission. An embedded real-time operating system will also be implemented to ensure the performance and reliability of the clinical device.

By addressing these objectives, the dissertation aims to contribute to the development of a state-of-the-art soft intra-abdominal wireless laparoscopic camera system, enhancing surgical capabilities and improving the overall surgical experience.

1.4 Challenges

Fully insertable laparoscopic devices present a distinct departure from conventional surgical robots, which are positioned external to the patient's anatomy, often come with exorbitant costs running into millions of dollars, and occupy substantial space within the operating room (OR). In contrast, these fully insertable devices must undergo miniaturization to operate effectively inside the patient's body, while also ensuring space efficiency, affordability, and clinical safety. The development and acceptance of these devices are met with complex technological and engineering

challenges that stem from the combined constraints imposed by physical and medical factors. Achieving miniaturization is imperative to accommodate narrow access points such as trocars or natural orifices. Furthermore, optimizing space efficiency becomes crucial to minimize interference with other surgical instruments and maximize OR utilization. Cost-effectiveness is another critical consideration, as affordable solutions are vital for widespread adoption and accessibility. Ensuring clinical safety is of utmost importance, necessitating designs that minimize tissue trauma, mitigate infection risks, and adhere to stringent medical device regulations and standards. The successful realization of fully insertable laparoscopic devices demands interdisciplinary expertise spanning robotics, materials science, miniaturization techniques, wireless communication, and bioengineering. By addressing these intricate challenges, fully insertable laparoscopic devices have the potential to revolutionize minimally invasive surgery and significantly enhance patient outcomes.

1.4.1 Mechanical and Actuation Design

The successful functioning of the fully insertable laparoscopic robot relies on effective anchoring and actuation to support the intended surgical operations. Due to the need for flexible maneuverability within the abdominal cavity, physical actuation linkages from outside the patient's anatomy are not feasible. Therefore, the robot must either utilize onboard actuators or explore non-contact transabdominal actuation technologies. One such innovative approach is magnetic coupling, which enables non-contact transabdominal actuation. However, modeling and controlling this method pose significant challenges.

To ensure reliable manipulation of the camera using an external magnetic field from the actuator, the magnetic coupling between the camera and actuator must generate sufficient force and torque for the camera's translation and rotation. In the surgical setting, there is a considerable air gap between the camera and the actuator due to the thickness of the patient's abdominal wall, typically ranging from $20mm$ to

$40mm$ [21]. As the distance between the camera and actuator increases, the magnetic force and torque rapidly diminish. Therefore, this work will thoroughly study the design and analysis of the magnetic driving unit and external actuator to achieve reliable camera actuation.

Another critical consideration during the mechanical design phase is the prevention of tissue overload and rupture. The motion pattern of the camera and the interaction between the camera and tissue are influenced by various factors such as component selection, layout, material, and structure. While some research has implemented force measurement to avoid excessive contact force, it is important to address the issue of stress concentration, particularly when a rigid-stick structured camera is anchored on a curved abdominal wall. Additionally, most prototypes rely on sliding motion with dry friction for camera translation, which is unsafe and hampers dynamic control due to creep behavior and slow response.

The insertion procedure also presents challenges for cameras with rigid structural designs. As the camera is inserted through a trocar, the coupling between the actuator and camera weakens. This often necessitates the use of a strong electromagnetic positioning system (EPM) or specialized instruments, which can be either unsafe or time-consuming. Therefore, the mechanical design of the camera should facilitate the insertion procedure and provide a simple solution.

1.4.2 Real-time Pose Tracking

In the operating room (OR), surgeons rely on direct vision to perceive spatial information and utilize various references for depth perception. However, LS presents an inherent problem of depth information loss, as the traditional laparoscopic vision provides a monocular 2D video [22]. Consequently, the 3D structural information of the surgical area are incomplete, while the poses of the internal devices are also inaccessible. This requires surgeons to mentally align instrument operation with the laparoscopic vision through hand-eye coordination during surgical tasks.

In contrast to the prevailing open-loop control systems found in most prototype devices, the lack of camera pose tracking in such systems leads to suboptimal precision in locomotion and limited resilience in uncertain environments [13][12][23][19]. Consequently, the camera may deviate from its intended trajectory and disconnect from the actuator's magnetic coupling. To address this issue and enable efficient manipulation of these devices from an external perspective, accurate pose restoration becomes crucial for effective feedback control. Various localization techniques have been proposed as potential solutions for transabdominal operations under the influence of strong magnetic fields [24], including electromagnetic wave and radiofrequency-based methods [25][26], X-rays [27][28], and video localization [29]. However, each of these methods faces technical challenges and practical implementation limitations. Consequently, the development of a practical and reliable localization method with reasonably low estimation error is of utmost importance. Such a method would greatly enhance the overall performance and usability of tetherless camera systems for medical applications.

1.4.3 Camera-tissue Interaction

After the insertion procedure, the manipulation of the camera becomes critical to focus on the operative area. Monitoring and controlling the magnetic coupling during this process is essential to maintain it within a specific range. This range should be carefully determined to ensure that the magnetic attraction is sufficient to counteract both gravitational force and tissue contact force. Maintaining this balance is crucial to prevent tissue damage and ensure safe and effective operation.

The interaction between the camera and the surrounding tissue, along with the distribution of stress, is a fundamental aspect that demands thorough examination. Developing a contact model that considers the deformability of both the camera and the tissue is imperative. Analyzing this contact model will provide valuable

insights and lay the groundwork for devising dynamic control strategies with robotic assistance.

Through the study of contact force and stress distribution, it will be possible to optimize the design and functioning of the laparoscopic camera system. This optimization will guarantee that the camera interacts with the tissue in a controlled and safe manner, minimizing the risk of tissue damage and enhancing the overall system performance.

1.5 Contributions

This work represents a significant advancement in the field of laparoscopic surgical instrumentation, with the development of a groundbreaking laparoscopic robot system. The research conducted in this study has successfully achieved the objectives outlined in Section 1.3, leading to several fundamental contributions that are summarized as follows:

1.5.1 Feasibility of A Novel Soft Intra-abdominal Laparoscopic Camera

A novel and innovative structure design for the tetherless fully insertable laparoscopic camera is proposed, incorporating principles from soft robotics and a wheel structure. The camera is constructed using soft silicone material, allowing it to passively bend along the curved abdominal wall. This design helps to alleviate stress concentration by increasing the contact area between the camera and the tissue. The deformability of the soft camera enables a simple insertion and anchoring procedure, which has been introduced and successfully demonstrated.

To assess the bendability of the camera and select suitable components, the relationship between the bending angle and the magnetic coupling force has been established. This analysis results help optimize selection of the components and

layout of the design to grant the camera desired flexibility while maintaining a reliable magnetic coupling for manipulation and control.

Additionally, a wheeled structure design has been implemented in the camera. This design facilitates a transition from sliding motion to rolling motion during translation, reducing the risk of tissue rupture. The rolling motion also contributes to smoother tilting and translating motions of the camera, enhancing the overall performance and safety of the device.

By combining the soft silicone material, passive bending capability, and wheeled structure design, the proposed camera achieves improved maneuverability and functionality within the abdominal cavity. This innovative design offers significant advantages over conventional sliding motion-based cameras, leading to a safer and more efficient laparoscopic surgical procedure.

1.5.2 Six-DOF Real-time Localization

A 6-DOF magnetic localization method has been developed for a magnetically driven laparoscope, which integrates an Inertial Measurement Unit (IMU), magnetic sensor, and double permanent magnet pairs. This method allows for accurate localization and tracking of the laparoscope's position and orientation within the abdominal cavity.

The roll and pitch angles of the camera without drift are obtained from a complementary filter based the IMU measurement. To ensure reliable localization, the laparoscope is designed with double magnet pairs. This configuration enables the camera to operate within a specific region where the magnetic coupling force is sufficient for accurate localization. Furthermore, the mapping relationship between the relative pose of the camera and the magnetic field measurements can be accurately modeled using two single dipole models.

Using this localization method, the laparoscope's 3-DOF position (x, y, and z coordinates) and yaw angle (rotation around the vertical axis) are obtained through an inverse mapping process and the Newton-Raphson method. This approach

avoids drift and provides robust and accurate measurements. The average error in position detection is reported to be $2.9mm$, indicating precise localization capability. Additionally, the error for angular motion, represented by the yaw angle, is below $5.5°$, demonstrating accurate tracking of the camera's orientation.

Overall, this 6-DOF magnetic localization method offers reliable and accurate positioning and orientation information for the magnetically driven laparoscope. It provides a valuable feedback for surgeons during laparoscopic procedures, enhancing precision and control within the surgical environment.

1.5.3 Closed-loop Control for A Robotic-Assisted Laparoscopic System

The development of a robotic-assisted closed-loop camera control system has been achieved by incorporating force and pose feedback. A camera-tissue contact model has been established to analyze the distribution of stress and deformation during camera-tissue interaction. This model allows for a comprehensive understanding of the forces exerted on the tissue and the resulting deformations.

In conjunction with the pose estimation method, a closed-loop control scheme has been implemented to enable precise control of the surgical view. The controller utilizes real-time feedback from the estimation of the contact force and camera pose to continuously update and optimize the control inputs. This closed-loop control approach ensures that the camera remains securely in place and avoids any potential damage to the tissue.

By utilizing the camera-tissue contact model and the closed-loop control scheme, surgeons are provided with a high level of control over the surgical view. They can manipulate the camera with confidence, knowing that it will maintain its position and orientation without dislodging or causing harm to the surrounding tissue. This closed-loop control system enhances the overall precision and safety of laparoscopic

procedures, allowing surgeons to focus on their tasks without concerns about camera stability or tissue damage.

1.5.4 Untethering Solution for Control Communication And High-Quality Video Transmission

To eliminate the need for tethering wires, the laparoscopic system has implemented dedicated wireless links for laparoscopic vision and control communication, powered onboard. A customized Bluetooth Low Energy (BLE) application profile has been developed specifically for this purpose. This profile enables seamless wireless communication between the laparoscopic camera and external devices, providing real-time transmission of video and control signals.

In addition, a real-time operating system (RTOS) based multitask programming framework has been proposed to efficiently manage the various tasks and processes within the laparoscopic system. This framework ensures precise timing and coordination of data transmission, image processing, and control algorithms, enhancing the overall performance and responsiveness of the system.

The implementation of this wireless solution has been realized using rapid prototyping technologies. Through rigorous testing and evaluation, the system has demonstrated its technical feasibility and capability to perform basic functions effectively. This untethered intra-abdominal laparoscopic camera solution not only addresses the issue of tethering wires but also showcases the potential for future development and integration of wireless technology in other insertable surgical instruments.

Furthermore, the proposed Bluetooth application profile and RTOS-based programming framework serve as valuable references for the design of embedded software in similar medical devices. They provide a solid foundation for achieving reliable and efficient wireless communication and control in various surgical instruments, fostering innovation and advancement in the field of minimally invasive surgery.

1.6 Dissertation Outline

The dissertation is organized as follows:

Chapter 2 presents approaches to the soft inserable camera including the tissue-contact friendly structure design, actuation principle, simplified insertion, modeling and evaluation of the bendability.

Chapter 3 propose the real-time pose estimation and evaluation for the inseratable camera based on multi-sensor fusing and Newton-Raphson iteration.

Chapter 4 details robotic-assisted control for the camera based on the tissue-camera interaction model and state estimations from Chapter 3.

Chapter 5 introduces electronic and software solution which enable high quality tetherless video streaming and control communication.

Chapter 6 concludes the dissertation and shares some vision into the future.

Chapter 2

Design of the Soft Wheeled Structure

2.1 Introduction

The paradigm shift from open surgery to single-incision laparoscopic surgery (SILS) has allowed surgeons to perform complex operations inside the human body cavity through a single keyhole incision, typically at the umbilicus. This technique offers several advantages, including minimal scarring and faster recovery [30]. However, the crowded nature of multiple laparoscopic instruments sharing a single port presents challenges for the maneuverability of rigid long-stick instruments, such as the laparoscope, within a limited conical workspace. In addition, this technique increases the complexity of operating surgical instruments and restricts the laparoscopes' field of view (FOV).

To address the issues of clutter in the surgical workspace and enhance the field of view (FOV) of the laparoscope, Cadeddu [7] proposed the concept of magnetic anchoring and guidance system (MAGS). In MAGS, a camera embedded with magnets is inserted into the patient's abdominal cavity and anchored against the abdominal wall with a magnetic actuator outside the body. By utilizing magnetic coupling

to replace rigid linkages, the actuator can steer the intra-abdominal camera to a desired position, freeing up the port for other instruments. Inspired by MAGS, several concept designs related to magnetically driven laparoscopes have been developed and evaluated in trans-abdominal operations [13][31][10][32][12][11].

Micro direct current (DC) motors have been integrated into the camera for precise tilting and panning, which can achieve an improved field of view (FOV), as described in [10][32][12]. In addition, Stephen proposed a motorized wheeled design to enhance the camera's mobility in slick, hilly, and deformable environments [13]. However, it should be noted that this design requires a larger space and an additional transmission mechanism, which consequently increases the weight and size of the camera. Furthermore, many wires are necessary to tether the camera due to the high power consumption of the onboard motors. These floating wires not only result in operational interference with other instruments and pressure leakage[32] but also apply dynamic disturbances to the locomotion of the camera.

Recent research has focused on developing intra-abdominal laparoscopes driven by magnetic interaction [15][33][23][18][19]. Garbin implemented an auto-flip feature on a laparoscopic camera using an orthogonal magnet arrangement and pure magnetic link [15]. Cheng established a visual servo control for a magnetic endoscope[33]. Our group has designed and prototyped an untethered robotic surgical laparoscope system in which the camera has four degrees of freedom (DOFs), wireless video transmission, and control communication[23][18][19].

One major drawback of the above camera systems is that they often need to pay more attention to the interaction between the camera and the soft tissues. Therefore, it is crucial to prevent overload and rupture of the tissue [20]. However, most designs follow a rigid stick form, which results in stress concentration on both ends of the device, mainly when anchored on a curved abdominal wall. Moreover, the sliding motion of the camera along the abdominal wall, caused by dry friction between the camera and the tissue, may lead to tissue rupture. Another challenge with rigid designs is the insertion and extraction process, which usually requires specific

tools or even another laparoscope to assist. Thus, developing a design that provides safer tissue interaction and deformability to fit in unstructured environments and deployments is essential.

Soft robotics has emerged as a promising field that offers compliance and adaptability to uncertain environments and enables safer interactions. Composed of flexible and stretchable materials, primarily silicone rubber, soft robots have several advantages, such as lightweight, low stiffness, cost-effectiveness, and safety, making them ideal candidates for next-generation instruments for SILS [34]. Pneumatic actuation is the most popular method among the designs, as it is lightweight, has good power density, and offers quick response. Furthermore, by pressurizing the internal chambers of the soft bodies through channels, the devices can expand, twist, bend, and elongate [35][36][37][38][39]. However, this method requires space in the trocar for inserting tubes and extra space in the surgical room for pressure sources and control devices. Additionally, it carries the risk of puncture or gas escape, which may cause damage.

Magnetic actuation provides a better approach for soft wireless devices, as the actuating fields can easily and harmlessly penetrate most biological materials and do not require tethers [40]. This technique has been successfully used in endoscope designs for drug delivery and gastrointestinal tract applications [41][42]. Cheng presented a soft MAGS endoscope that consists of a silicone rubber structure and a wireless camera module [43]. The design is purely driven by magnetic coupling and has four DOFs. However, the tilting and translation motions are strongly coupled and need to be controlled sequentially. In addition, the translation still relies on sliding motion, and the tissue contact and insertion process are not thoroughly discussed.

In this chapter, we propose a soft intra-abdominal wireless laparoscope. There are three main contribution of our work. First is combining the soft silicon material with our former camera designs [23][18][19], so that the camera can passively bend along the curved abdominal wall to relieve the stress concentration. The relationship between bending angle and the magnetic coupling force are established to assess the bending

capacity and component selection. The performance are evaluated by simulation and experiments. Second is introducing and demonstrating an easier procedure for inserting the soft camera through a trocar and anchoring it on the tissue. Finally, applying a wheeled structure design to the camera, the contact between the tissue and device is transferred from sliding motion to rolling motion during translation. It not only helps avoid tissue rupture, but also make the tiling and translating motion smoother. The system design and operation principle are described in Section 2.2 and Section 2.3. Section 2.4 provides modeling and analysis for bending capacity and component selection. Section 2.5 shows the fabrication process. The demonstration and evaluation based on experiments are demonstrated in Section 2.6. Conclusions and future work are presented in Section 2.7.

2.2 System Mechanical Design

2.2.1 System Overview

Robotic-assisted surgery (RAS) has undoubtedly emerged as a prominent field in modern medical science, offering numerous benefits in terms of precision, control, and improved surgical outcomes. As the field continues to advance, it is crucial to integrate robotics into the development of next-generation laparoscopic cameras to further enhance the precision and intuitiveness of surgical imaging [44][45].

The wireless laparoscope is designed to be a RAS system subsystem, illustrated in Fig. 2.1. The RAS system consists of a fully insertable wireless camera, an external actuator, a force-torque sensor, and a multi-DOF manipulator. This RAS system uses a collaborative lightweight robotic arm with force sensing and collision detection capabilities to manipulate the external actuator. This robotic arm provides automation and interacts safely with surgeons during surgery. It is designed to stop in milliseconds in case of an overload or collision, preventing potential injuries or accidents. The surgeon can manually drag the collaborative robotic arm to take

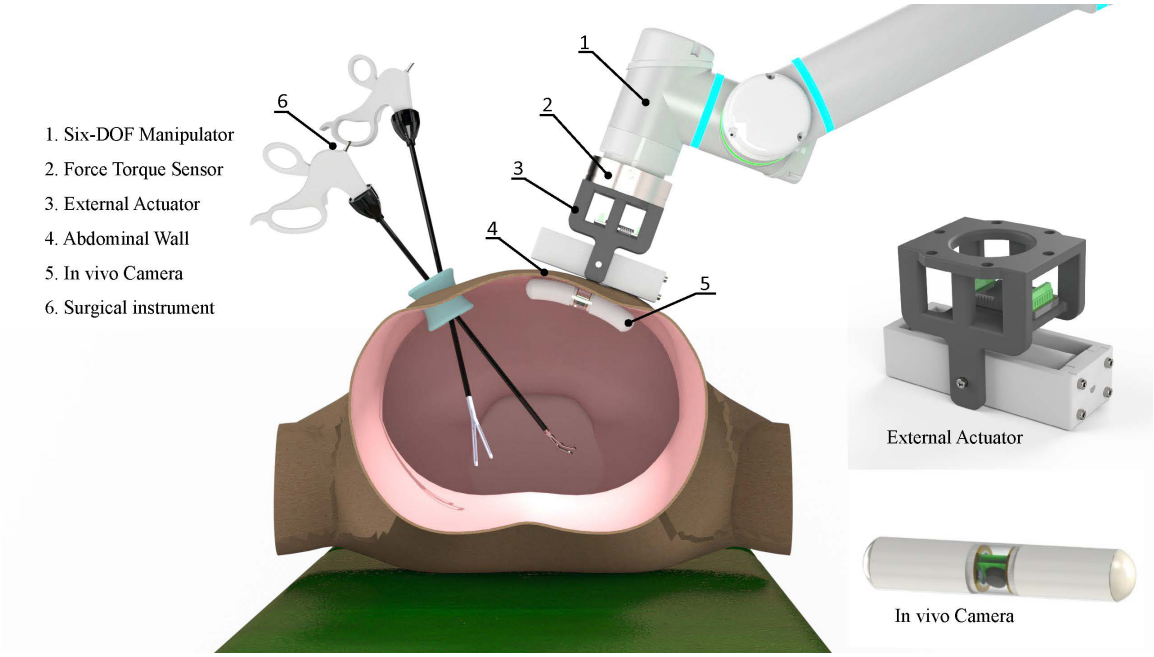

Figure 2.1: The proposed wireless laparoscopic camera works as a subsystem of the robotic surgical assistant system, including an external actuator and in vivo camera module. Made with soft material, the camera can passively bend along the abdominal wall to relief the stress on tissue.

control of the external actuator at any time during the surgery in case of an incident and reposition it to a desired safe pose, avoiding secondary harm. The robotic arm will follow the manual dragging passively until automatic control is re-enabled.

The camera and actuator are integrated with two permanent magnet pairs, which generate a magnetic solid coupling force that allows the camera to be anchored and navigated against the abdominal wall after being inserted through a trocar. The force-torque sensor (Axia80-M20, ATI) monitors the magnetic coupling force and estimates the contact force between the camera and the patient's tissue to avoid excess pressure and ensure sufficient coupling. During the surgery, the camera is inserted into the insufflated abdominal cavity through a SILS port and steered to the desired anchor position, leaving the port free for other surgical instruments.

2.2.2 Design of The Intra-abdominal Wireless Laparoscope

Fig. 2.2 in the illustration shows the assemblies of actuator and the wireless camera. The compact camera measures $20mm$ in diameter and $100mm$ in length. The camera design is made up of two internal permanent magnets (IPM), ball bearings, soft shafts and tubes made with silicone rubber, battery packages, sleeve bearings, a PCB board, a lens, and a clear PVC tube. The camera's internal structure is symmetric, and the layout of each component is shown in Fig. 2.3. The IPMs are diametrically magnetized identical ring magnets and made with Grade 42 NdFeB. They are located at each end to couple with external permanent magnets (EPMs) that are embedded in the external actuator. The $75mm$ gap between the IPMs aims to provide higher rotating torque and avoid magnetic interaction. The camera board embedded with sensors and chips is fixed with two sleeve bearings. Two soft shafts made with silicone rubber, carrying the IPMs and the battery packages, are supported by ball bearings and sleeve bearings. They work with soft tubes to grant the camera bendability, allowing it to bend passively along the curved abdominal wall to create a larger contact area as it is anchored against it.

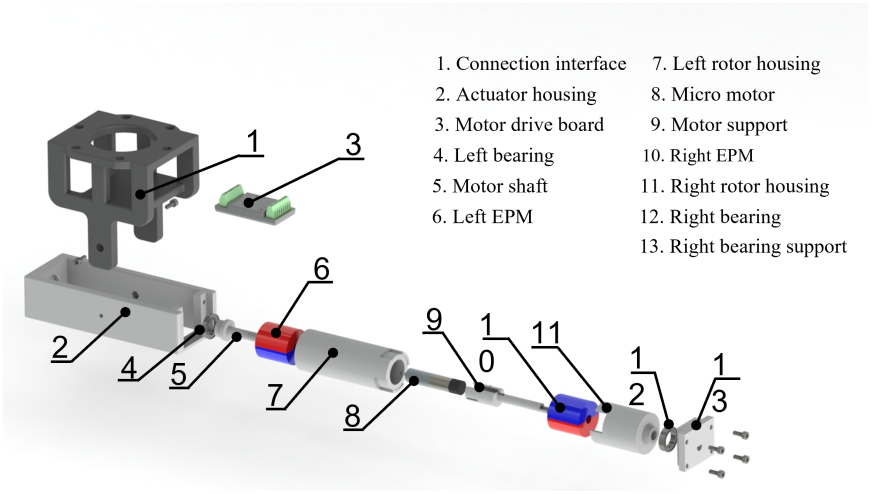

(a) Actuator module

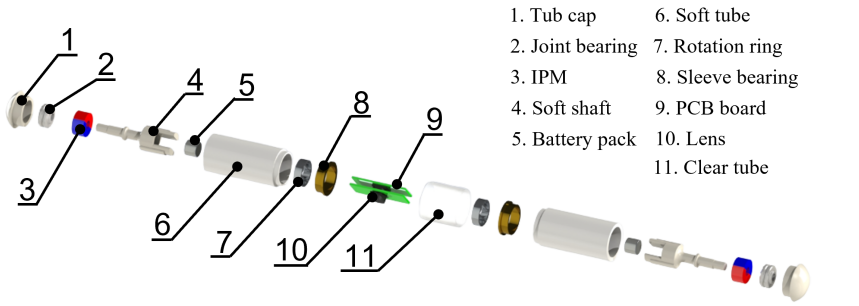

(b) Camera module

Figure 2.2: Assembly exploded view of the actuator and the camera. The system design is based on double pairs of magnets, which provide stronger and stabler coupling than a single-magnet pair design.

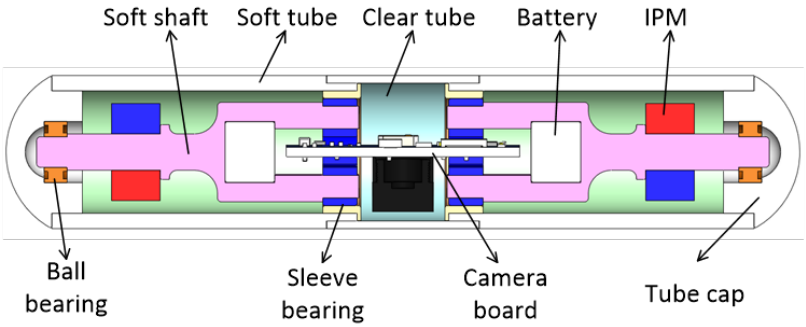

Figure 2.3: The layout of the camera shows the combination of soft material and wheeled structure design.

On the other hand, the external actuator ($length \times width \times height = 126mm \times 63mm \times 86.5mm$) contains a connection interface part that is used to mount the housing onto the force-torque sensor and then connect it with the manipulator. All the structure components are 3D printed with photopolymer by an SLA printer (Form 3+, Formlabs). Two EPMs are inserted into the rotor housing, which is supported by two ball bearings and can rotate inside the actuator housing. The axial distance between the EPMs is identical to that of the IPMs in the camera. A 24V micromotor (1016M009SR, FAULHABER) is also integrated into the rotor to control the rotation of the EPMs concerning the housing. The motor is integrated with a 256:1 ratio gearhead, which allows it to generate 1Nm of torque. The motor is connected and controlled by a driver board through a flexible flat cable mounted onto the connection interface part.

In this design, the internal components are deployed horizontally. Compared with the vertical layout, the horizontal layout has the following advantages: 1) it provides extra space for double pairs magnets that generate stronger coupling strength. 2) Replacing one pair of wide magnets with two pairs of magnets with smaller diameters, the camera can be designed in a smaller diameter by choosing smaller IPMs, which requires a smaller incision and trocar for the insertion with even stronger coupling. 3) As shown in Fig. 2.4, in a vertical layout, the panning motion DOF around z_c is lost when the magnetic moments of the IPM and EPM are aligned in singularity position. This situation can be avoided in a horizontal layout with two pairs of magnets. 4) Designing with a horizontal layout, the CMOS and the lens are further to the target area, which offers a larger FOV.

Meanwhile, the PCB board, IPMs, and battery packages can be combined as a whole piece and rotate freely around x_c inside the tubes, as shown in Fig. 2.5. As a result, when the external actuator drives the camera to translate along y_c and tilts around x_c, the tubes work as a wheel rolling along the abdominal wall. This feature transfers the sliding motions, that are common in most of the existing designs, into rolling motions. The dry friction between the camera and tissue is also replaced with

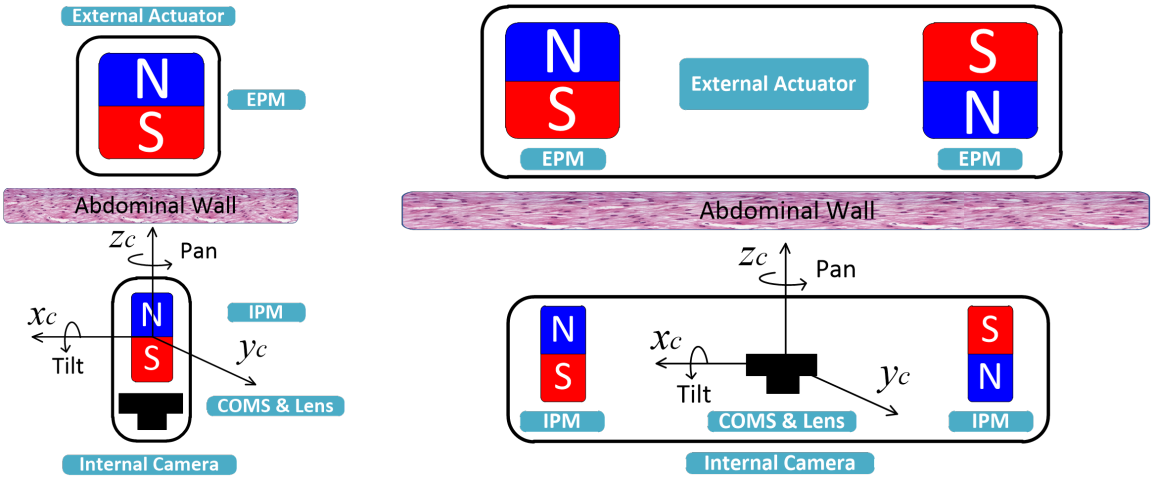

Figure 2.4: The comparison between vertical layout and horizontal layout. The horizontal layout grants a larger field of view, stronger magnetic coupling, smaller diameter design, and stable panning motion free from singularity.

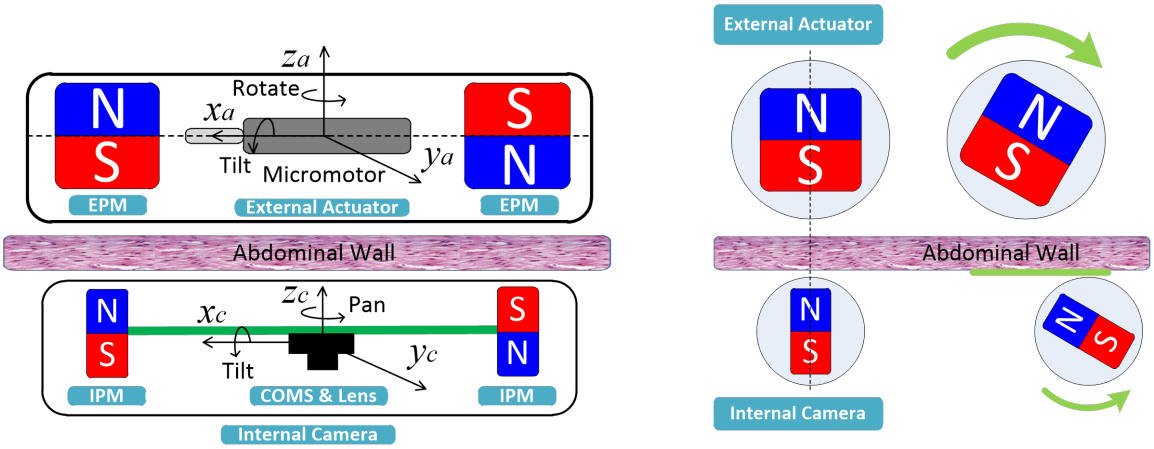

Figure 2.5: Rolling motion with wheel structure design. This feature transfers the sliding motion into rolling motion when the camera is translating along y_c and tilting around x_c. The dry friction between the camera and tissue is also replaced with ignorable rolling friction.

ignorable rolling friction. It not only protects the tissue from being ruptured by the camera but also simplifies the friction model and grants fast response in dynamic control.

Finally, composed of soft shafts and soft tubes, the camera is capable of bending around z_c and y_c. The bendability of camera is modeled and discussed in Section 2.4 Attracted by the EPMs, the camera can passively bend along the abdominal wall, which relieve the stress concentration by increasing the contact area. The material of the soft tube is selected softer than the abdominal tissue. The deformation of the tubes on the one hand increase the contact area which further reducing the stress on the tissue, on the other hand boosts rolling friction. The camera-tissue interaction model analyzed in Chapter 4 will facilitate find a balance.

2.3 Working Principle of the Magnetic-driven Laparoscope

2.3.1 Intra-abdominal locomotion

The magnetic actuation mechanism and the layout of the components inside the modules are shown in Fig. 2.6. The actuator and the camera frames $\{a\}$ and $\{c\}$ are fixed with the centers of the actuator roller, and the camera board. z_a and z_c are parallel to the pole directions of the magnets. The camera-actuator distance affects the pressure on tissue and the magnetic coupling force. The stress distribution on tissue generated by our magnetic laparoscope is analyzed in [46], concluding that the desired distance should be between $35mm$ to $55mm$.

Dragged by the manipulator, the EPMs can drive the camera to translate along the abdominal wall and rotate around z_c. The tilt motion around x_c is realized by actuating the micromotor inside the actuator. Thanks to the wheel structure, the camera board, and IPMs as one whole piece can rotate freely around x_c with respect to the camera tube. The rolling motion makes the tilt and translation much smoother

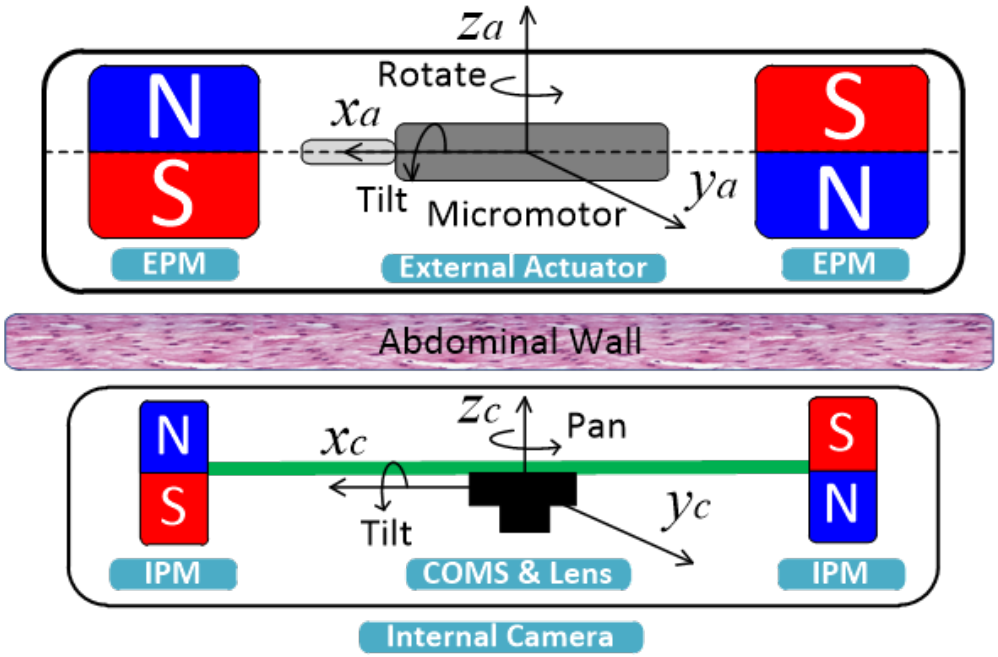

(a) Front view

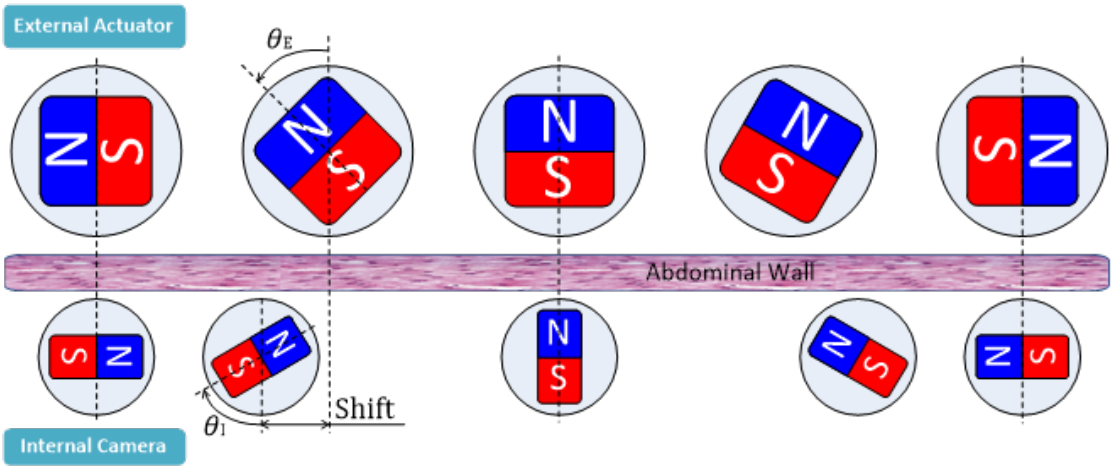

(b) The sequence of camera tilting viewed from a direction parallel to x_a.

Figure 2.6: Intra-abdominal magnetic actuation principle. The camera has 4-DOF including 2-DOF translation, tilt, and pan. In the tilt motion, The coupling pairs from left to right show the tilting sequence from $+90°$ to $-90\circ$. Since the magnetic moment of IPMs always follows the magnetic moment of EPMs, the relationship between EPM tilt angle θ_E, IPM tilt angle θ_i and horizontal shift δ_s can be easily modeled.

and less laggy, and the magnetic coupling is more stable. The tilt motion has a range of $\pm 90^{\circ}$ without singularity. Oppositely, due to the rolling motion, the camera will shift along the abdominal wall when it is tilting Although the tilt and translation motion is coupled, as long as the relative pose between the IPMs and EPMs, the kinematics of the tilt motion can be easily modeled based on the single dipole model by assuming that the magnetic moment of IPMs is always aligned with the magnetic moment of EPMs.

2.3.2 Insertion Procedure

The insertion procedure is a challenge for most of the existing rigid camera designs. Fig. 2.7 shows a general problem for the insertion. In Fig. 2.7a, during the insertion of the camera through a trocar, the magnetic coupling becomes weaker as the distance between the EPM and IPM increases. A strong EPM is required to maintain the coupling, which is apparently unsafe in OR. Even the magnetic coupling can be kept till the camera is fully inserted, the coupled end of the camera tends to impact the tissue while the non-coupled end turns to fall, shown in Fig. 2.7b. To avoid the unacceptable situation, special instruments accompanied by an extra laparoscope are used to assist the procedure.

The simplified insertion procedure with soft structure design is shown in Fig. 2.8, the magnetic coupling between one pair of EPM and IPM is built as the far end of the camera comes out from the trocar. During the insertion, the camera is passively bent by the magnetic attraction, thus the distance between the coupled EPM and IPM is almost constant, and the magnetic coupling is stable. When the camera is almost fully inserted, the actuator rotates around the coupling end of the actuator and establishes the coupling on the other end. The whole process is totally independent of other custom instruments. The force-torque sensor monitors the coupling force to guarantee it's sufficiently strong to overcome the friction and bending force and stays beneath the threshold value for not damaging the tissue.

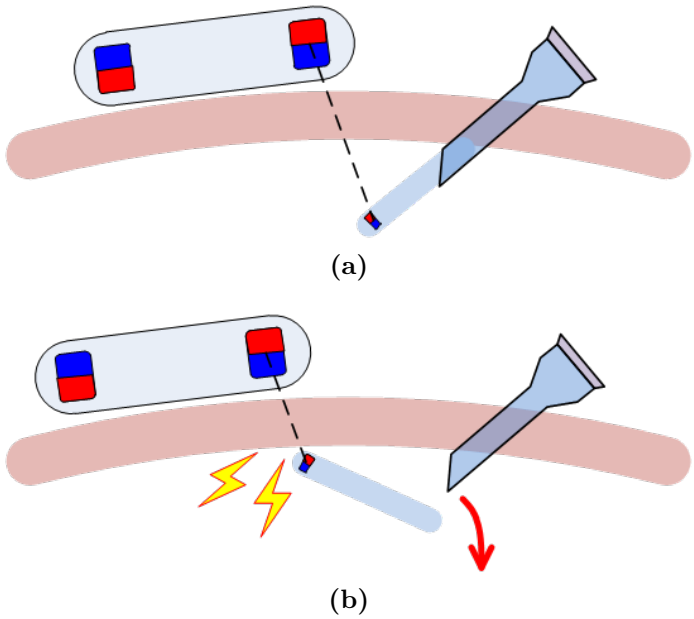

Figure 2.7: The insertion procedure is challenging for existing rigid designs. a) During the insertion of the camera through the trocar, the magnetic coupling becomes weaker as the distance between the EPM and IPM increases. b) When the camera is totally inserted, the left end of the camera tends to impact the tissue while the right end turns to fall.

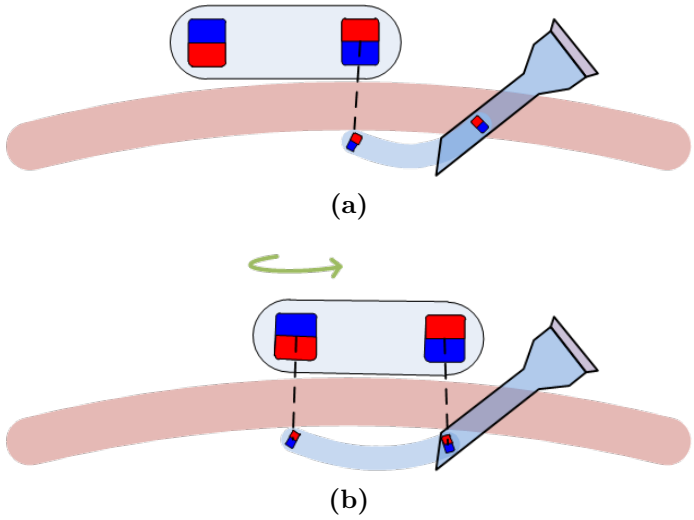

Figure 2.8: The simplified insertion procedure with soft structure design. a) During the insertion of the camera through a trocar, the distance between the EPM and IPM is almost constant, and the magnetic coupling is maintained stably. b) When the camera is almost totally inserted, the actuator rotates around the coupling end and establishes the coupling on the other end.

2.4 Modeling of Bendability

In this section, the bendability of the camera is modeled based on the cantilever beam model. Assisted with the proposed model, we notice the bendability of the camera is affected by the magnetic moment of the IPM, the material of the soft tube and soft shaft, and the position of the IPMs and ball bearings. The relationship between the magnetic coupling force and the bending angle and vertical displacement is formulated. Table 2.1 shows the nomenclature used in this section.

As shown in Fig. 2.9, assuming the tube and shaft can not rotate around the x axis, they can be modeled with a cantilever beam, where one end of the beam is fixed while the other end is free. M_1 and M_2 represent the reaction moment from the sleeve bearings applied to the soft tube and the soft shaft respectively. R_1 and R_2 are the reaction force also generated by the sleeve bearing. F_m is the magnetic force applied to the IPM. F_1 and F_2 are the reaction force between the soft tube and the soft shaft on the free end passed by the ball bearings. θ and y represent the bending angle and displacement of the free end relative to the fixed end.

Given the loading diagram the shaft and the tube in Fig. 2.10, the reaction forces and moments R_1, R_2, M_1 and M_2 can be solved by

$$\begin{aligned} \sum F_y &= 0 \\ \sum M_O &= 0 \end{aligned} \tag{2.1}$$

$$\begin{cases} R_1 = F_1 \\ M_1 = F_1 l_1 \end{cases} \tag{2.2}$$

$$\begin{cases} R_2 = F_m - F_2 \\ M_2 = F_m l_2 - F_2 l_1 \end{cases} \tag{2.3}$$

where l_1 and l_2 represent the positions of the free end and the IPM relative to the fixed end of the tube.

Table 2.1: Notations for Bendability Modeling

Symbol(s)	Meaning
F_1	Regular font refers to scalar.
$< x - a >^{-2}$	Singularity function representing Moment load
$< x - a >^{-1}$	Singularity function representing Concentrated load

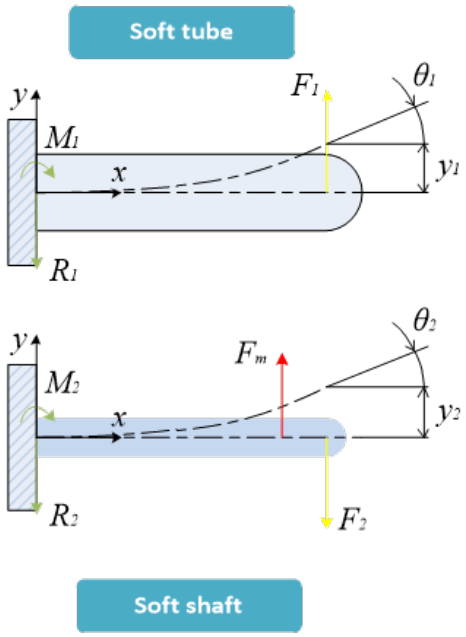

Figure 2.9: Loading diagram of the camera

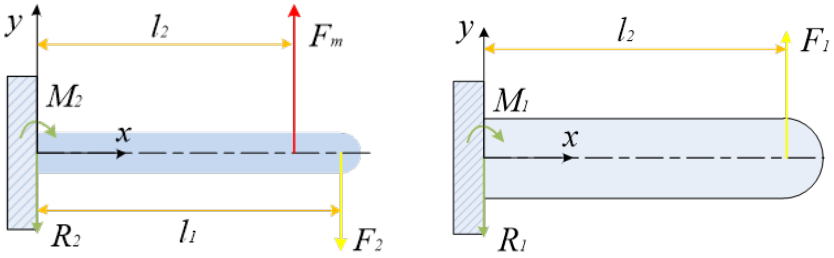

(a) Loading diagram of the soft shaft.

(b) Loading diagram of the soft tube.

Figure 2.10: Loading diagram of the soft shaft and the soft tube.

Because the loads on beams typically consist of collections of discrete entities, such as point loads or segments of distributed loads that can be discontinuous over the beam length, it is difficult to represent these discrete functions with equations that are valid over the entire continuum of beam length. A special class of functions called singularity functions was invented to deal with these mathematical situations. In this paper, the singularity functions are denoted by a binomial in angled brackets as shown in Table. 2.1. x is the distance along the beam length. a denotes where in x the singularity function either acts or begins to act. Accordingly, the loading, shear, moment, bending angle and displacement of any point on the soft shaft relating to x are obtained as

$$
\begin{aligned}
q(x) &= M_2 < x-0 >^{-2} - R_2 < x-0 >^{-1} + F_m < x-l_2 >^{-1} - F_2 < x-l_1 >^{-1} \\
V(x) &= \int q(x) = M_2 < x-0 >^{-1} - R_2 < x-0 >^{0} + F_m < x-l_2 >^{0} - F_2 < x-l_1 >^{0} \\
M(x) &= \int V(x) = M_2 < x-0 >^{0} - R_2 < x-0 >^{1} + F_m < x-l_2 >^{1} - F_2 < x-l_1 >^{1} \\
\theta_2(x) &= \int \frac{M(x)}{E_2 I_2} dx \\
&= \frac{1}{E_2 I_2} \left[M_2 < x-0 >^{1} - \frac{R_2}{2} < x-0 >^{2} + \frac{F_m}{2} < x-l_2 >^{2} - \frac{F_2}{2} < x-l_1 >^{2} \right] \\
y_2(x) &= \int \theta(x) dx \\
&= \frac{1}{E_2 I_2} \left[\frac{M_2}{2} < x-0 >^{2} - \frac{R_2}{6} < x-0 >^{3} + \frac{F_m}{6} < x-l_2 >^{3} - \frac{F_2}{6} < x-l_1 >^{3} \right]
\end{aligned}
\tag{2.4}
$$

where E_2 is the young's modulus of the shaft that relates to the material. I_2 is the inertia moment of the shaft which relates to the shape and bending direction.

Similarly, the singularity functions of the soft tube are expressed as

$$
\begin{aligned}
q(x) &= M_1 < x-0 >^{-2} - R_1 < x-0 >^{-1} + F_1 < x-l_1 >^{-1} \\
V(x) &= \int q(x) = M_1 < x-0 >^{-1} - R_1 < x-0 >^{0} + F_1 < x-l_1 >^{0} \\
M(x) &= \int V(x) = M_1 < x-0 >^{0} - R_1 < x-0 >^{1} + F_1 < x-l_1 >^{1} \\
\theta_1(x) &= \int \frac{M(x)}{E_1 I_1} dx = \frac{1}{E_1 I_1}\left[M_1 < x-0 >^{1} - \frac{R_1}{2} < x-0 >^{2} + \frac{F_1}{2} < x-l_1 >^{2} \right] \\
y_1(x) &= \int \theta(x) dx = \frac{1}{E_1 I_1}\left[\frac{M_2}{2} < x-0 >^{2} - \frac{R_1}{6} < x-0 >^{3} + \frac{F_1}{6} < x-l_1 >^{3} \right]
\end{aligned}
\tag{2.5}
$$

where E_1 is the Young's modulus of the tube that relates to the material. I_1 is the inertia moment of the tube which relates to the shape and bending direction.

Since the free ends of the tube and the shaft are connected by the ball bearings, we can assume the reaction forces and the displacements at the free end are equal, which gives

$$
\begin{cases}
y_1(l_1) = y_2(l_1) \\
F_1 = F_2
\end{cases}
\tag{2.6}
$$

The reaction forces F_1 and F_2 at free end are solved as

$$
F_1 = F_2 = \frac{E_1 I_1 F_m (3 l_1 l_2^2 - l_2^3)}{2 l_1^3 (E_1 I_1 + E_2 I_2)}
\tag{2.7}
$$

Substituting F_1 into $y_1(l_1)$ and $\theta_1(l_1)$, the bending angle and displacement of the camera free end are solved as

$$
\begin{aligned}
y_1(l_1) &= \frac{F_m (3 l_1 l_2^2 - l_2^3)}{6 (E_1 I_1 + E_2 I_2)} \\
\theta_1(l_1) &= \frac{F_m (3 l_1 l_2^2 - l_2^3)}{4 l_1 (E_1 I_1 + E_2 I_2)}
\end{aligned}
\tag{2.8}
$$

2.5 Prototype Fabrication

The prototyped actuator and camera are demonstrated in Fig. 2.11. Our camera design has the advantages of simple fabrication and assembly. It relies on a pure magnetically driven method. Our design contains fewer components than others with onboard motors and transmission mechanisms. The ball bearings, IPMs, and clear tubes are all on-shelf products. The sleeve bearings ($ID \times OD \times length = 14mm \times 16mm \times 5mm$) are made with 932 bearing bronze. The camera board is developed around a Texas Instruments cc2541 wireless microcontroller unit (MCU), a low-cost and power-efficient system-on-chip (SOC) solution for Bluetooth Low Energy (BLE) application. The cc2541 provides wireless communication and an interface for managing onboard resources. A digital CMOS sensor (IMX323, SONY) is embedded to offer HD1080p video. Preprocessed by an image signal processor (ISP, NVP2441), the digital images are transferred into analog video and sent to the AV transmitter module (RTC6701). Additionally, an MPU-9250 inertial sensor and a 3D linear Hall-effect magnetometer (ALS31313) are embedded to collect motion and magnetic field data, which can be further forwarded through cc2541 and utilized for pose estimation [25].

The soft shafts and tubes are prototyped by silicone rubber mold casting, which is economical and easy. In order to bear the heaviest parts, including IPMs and batteries with relatively more minor section area and inertia moment, the shafts should use stiffer material ($Smooth - Sil^{TM}945$, SMOOTH-ON). The soft tubes, directly contacting patients' tissue, are made with biocompatible silicone rubber ($DragonSkin^{TM}20$, SMOOTH-ON). Fig. 2.12 shows the fabrication parts. Firstly, the mold parts are created in CAD software (SOLIDWORKS R2019, Dassault Systèmes) and 3D printed by the SLA printer. Typically, each mold assembly has three pieces for easier demolding, in which the bottom two pieces shape the external profile, and the top piece extrudes the internal cavity. Several holes are created at the top and bottom of the mold to ensure that the silicone material fills the mold

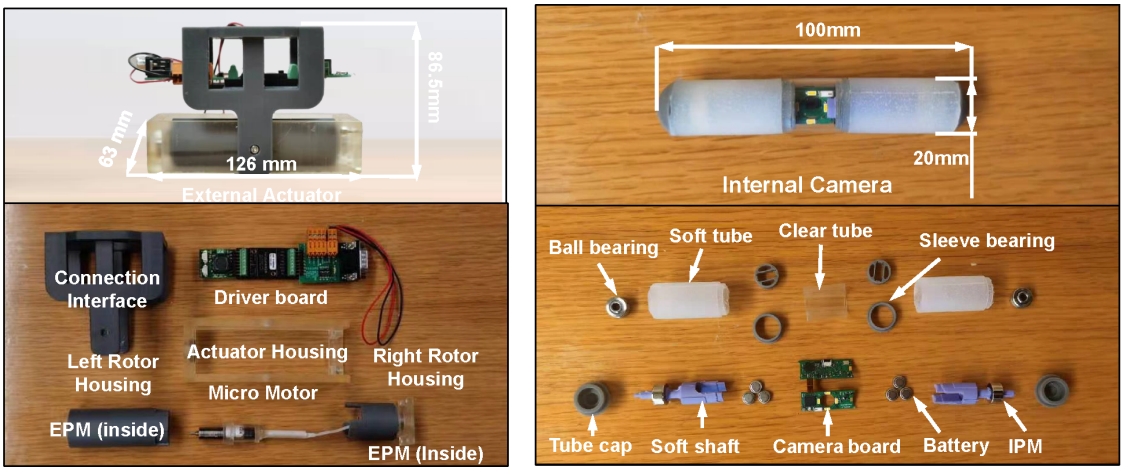

(a) The prototyped actuator. **(b)** The prototyped camera.

Figure 2.11: The prototyped actuator and camera.

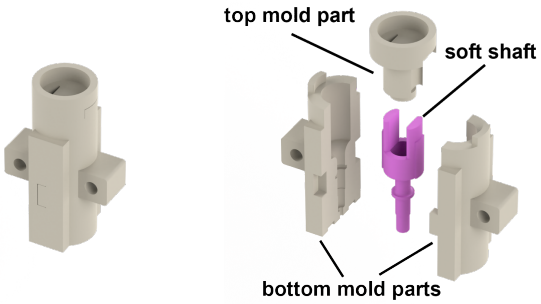

(a) Fabrication of soft shaft.

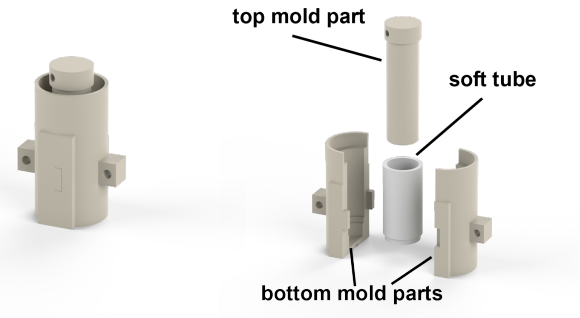

(b) Fabrication of soft tube.

Figure 2.12: Each mold contains three pieces, in which the bottom two pieces shape the external profile, and the top piece extrudes the internal cavity.

thoroughly and builds an intact shape. Secondly, measure and mix the liquid rubber into the mixing container at room temperature according to the instruction. Vacuum degassing is performed to eliminate entrapped air in the liquid. Then, apply some petroleum jelly to the inside of the mold, pour the mixture into the bottom mold pieces, and insert the top piece on the top. The mold is bundled with thread tightly to keep the mixture inside and left to cure for 4 to 6 hours. Finally, trim the extra material on the soft parts due to leakage after demolding.

The camera board, IPMs, bearings, and soft shafts can be assembled as a whole piece and inserted into the tubes. The soft tubes, clear PVC tubes, and tube caps form an enclosure space, sealing all the components inside the camera. All the components except for the camera board are low-cost and can be treated as surgical consumables to simplify the preparation and sterilization procedure.

2.6 Experiments and Results

2.6.1 Experimental setup

With the above design and implementation, four ex vivo experiments were conducted to evaluate the function and performance of the system. The scenarios are illustrated in Fig. 2.13. First, a simulated surgical scenario was built to investigate locomotion's dexterity, including translation, panning, and tilting. Second, the stress distribution applied on the abdominal wall from our soft camera and a rigid mock-up device was compared and analyzed based on both simulations and experiments. Then, the bendability of the camera was assessed by measuring the relationship between the bending angle and the applied magnetic coupling force. Finally, the insertion procedure for the soft design was demonstrated to validate the feasibility.

In the locomotion test, the camera was put into a 3-Dmed synthetic human belly model and anchored against the interior abdominal wall by the external actuator shown in Fig. 2.13a. The external actuator was mounted onto and manipulated by a

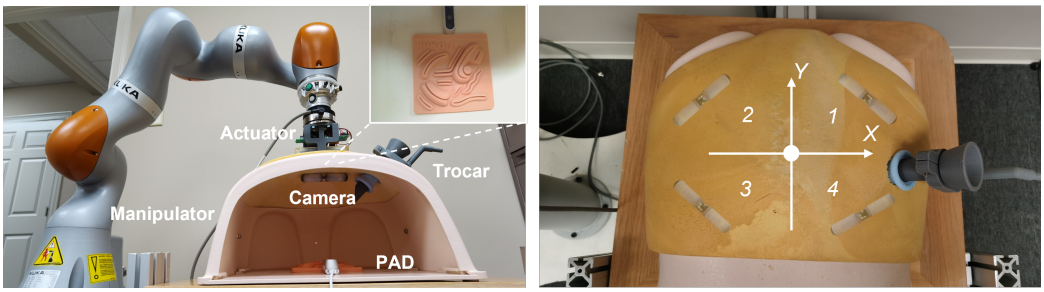

(a) Locomotion dexterity test.

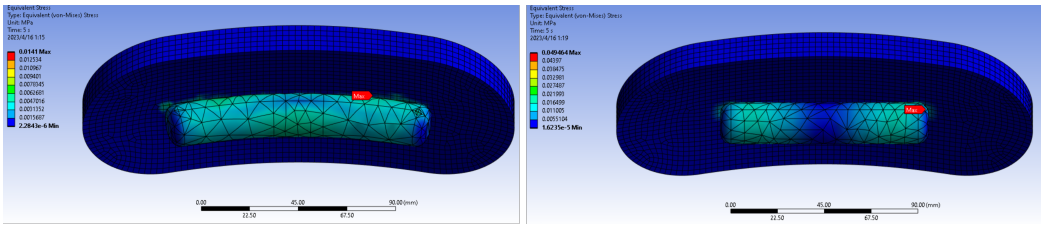

(b) Stress distribution analysis in simulation.

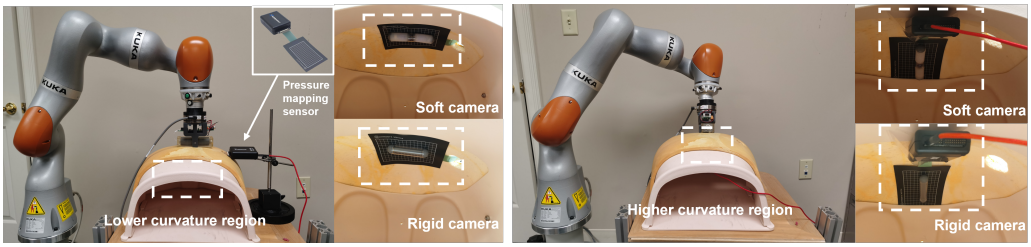

(c) Stress distribution analysis with sensor measurement.

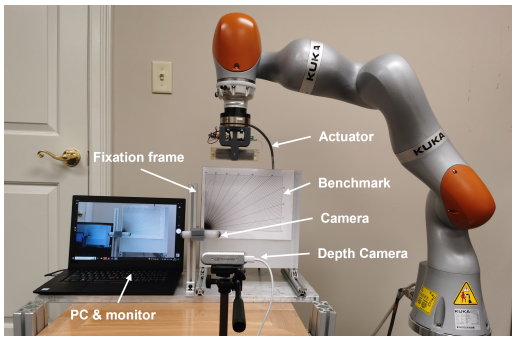

(d) Bendability test.

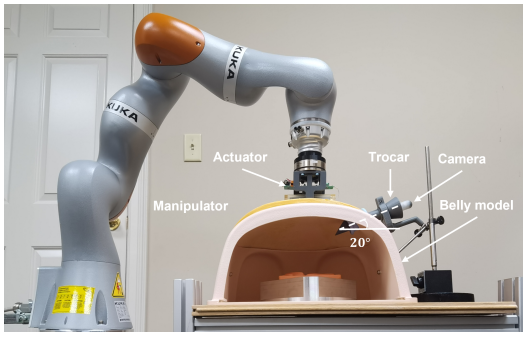

(e) Insertion demonstration.

Figure 2.13: **a** The left figure shows the panning and tilting test. In the right figure, the belly model was separated into four regions, and the duration of the steering camera to the four regions was recorded. **b** The soft camera model (left) can bend along the curved tissue, while the rigid camera model (right) creates obvious stress concentration. **c** Our soft camera and a rigid mock-up camera were placed on the belly model to measure the pressure. Two regions with different curvatures were picked. **d** The bendability of the camera was validated by applying magnetic force, which helps plan the insertion procedure and optimize the camera design. **e** The camera was inserted through the trocar fixed with 20°. Ten trials were recorded.

7-DOF collaborative robot (LBR iiwa 7 R800, KUKA) through a force-torque sensor (Axia80-M20, ATI). First, the camera was controlled to perform panning within ±90∘ and tilting within ±90° repeatedly to prove the motion range. Meanwhile, the wireless video received by the AV receiver module was connected to a video converter for display, storage, and processing on a PC. A soft tissue suture pad (3-DMED) was placed in the FOV of the camera, working as a reference. Secondly, the abdominal wall was separated into four regions. The camera was maneuvered to move from the center of the frame to the four regions in sequence and adjust to proper poses to provide a stable vision field. After the reference tissue pad was shown close to the center of the image, the video and the operation time were recorded for further discussion.

The stress distribution analysis compares the stress applied to the tissue by the standard design with a rigid structure and our soft camera. We created several simulations with Finite Element Analysis software (Ansys Workbench 2022 R2, Ansys) shown in Fig. 2.13b, where a piece of tissue was fixed in the workspace, and a rigid stick and a deformable soft stick were pressed against the tissue, respectively. The press forces were used to express the magnetic coupling force, increasing from $2N$ to $8N$ by $2N$ in each step. The stress distribution and the maximum stress expressed by von Mises stress were collected for comparison. Meanwhile, a scenario was built with the synthetic human belly model to measure the pressure applied to the model. We designed and fabricated a mock-up camera with a rigid structure. It integrated the same IPMs with the soft camera and had similar dimensions and weight. Two regions in which the curvatures of the belly model were quite different were picked for anchoring the cameras. A pressure mapping sensor (MP2508 Plus with MS9724, Kitronyx) was placed between the camera and the belly model to measure the pressure data. The setup is shown in Fig. 2.13c.

The bendability of the camera structure helps us understand the device's property and better define the operation and insertion procedure as shown in Fig. 2.13e. The experiment showed in Fig. 2.13d contained a fixation frame to mount the camera

module. An aluminum profile structure supports a benchmark showing angles from 0° to 90°. The origin was aligned with the bending center of the camera. During the experiment, the manipulator controlled the actuator to approach the camera module vertically and utilize one EPM embedded in the actuator to attract the IPM inside the camera. The force-torque sensor kept measuring the coupling force. Meanwhile, a depth camera ($RealSense^{TM}D435$, Intel) was placed in front of the scenario to record the bending angle. The maximum bending angle and the relationship between the bending angle and coupling force were noted.

The insertion procedure started with inserting the camera module into the trocar. The trocar could be fixed with an angle lower than the maximum bending angle of the camera. Then, following the pre-defined procedure, the actuator was steered to move toward the camera and built coupling between the magnets. Finally, the camera was moved to a proper position and left the trocar was free for other instruments. Each step's whole procedure and consumption time were recorded to estimate the performance.

2.6.2 Result Analysis

Dexterity of locomotion

The results of the dexterity test are summarized in Fig. 2.14. Anchored at the center of the belly model, the camera could pan stably within ±90° at angular speed $20°s$. For the tilting motion, the camera could rotate within ±90° smoothly with a fast response. During the tilting, the camera's shell rolled like a wheel and slightly shifted along the belly model, which was expected for this wheeled structure design. When the tilting angle approaches ±90°, the camera board tends to flip over and go across the singularity. Thus, it was constrained to operate within ±60°. Aided by the camera's 60° FOV, it was sufficient to observe the whole abdominal cavity.

The duration to navigate the camera from the center of the frame to the four regions and provide proper FOV are presented in Fig. 2.14d. The actuator operation

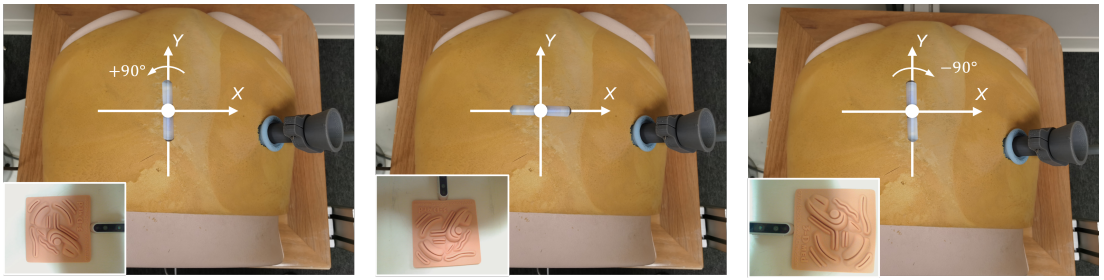

(a) Pan motion test.

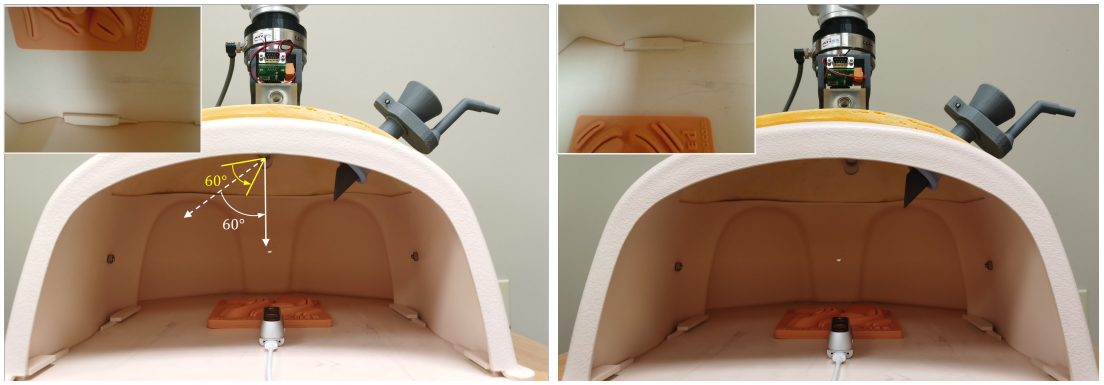

(b) Tilt motion test.

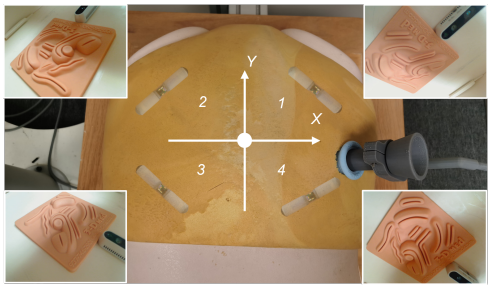

(c) General locomotion dexterity test.

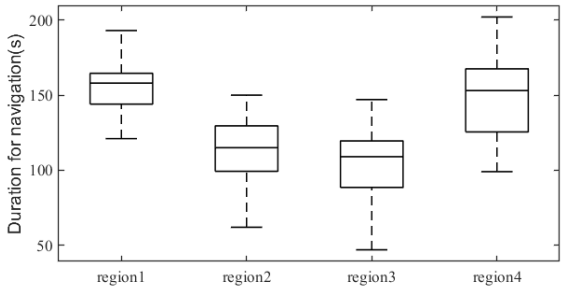

(d) Box plot of locomotion duration.

Figure 2.14: **a** The camera has the pan motion of ±90°. The bottom-left insets indicated the images captured by the camera. **b** The camera is capable of achieving ±90° continuous tilt motion. Typically, the camera is able to observe the entire surgical scene within ±60° of tilt movement. Images taken were provided in the corner insets. **c** The camera is driven from the center to four regions and provides desired FOV. The operation time is recorded. The insets at four corners show the recorded images. **d** Box plot presenting operation time used to assess dexterity of navigation.

used a hybrid mode, where the manipulator was manually dragged under hand-guiding mode and a client on PC. Fifteen trials were recorded for each region. The average duration for the four cases was 156 seconds, 111 seconds, 103 seconds, and 148 seconds. The average duration to navigate it to region 2 and 3 are 30% lower than the other two situations. This is affected by the position of the trocar. The camera had to be manipulated to bypass the trocar's position and avoid collision with the trocar in the adjustment.

Stress distribution

Fig. 2.15 compares the stress distribution in both simulations and experiments. In the simulations (Fig. 2.15a), with the same press force, the contact area between the tissue and the device with the soft design was all larger than the rigid design. As the pressing force increased from $2N$ to $8N$, the contact area also raised apparently in the soft design cases, while it did not significantly change in the rigid design cases. The maximum stresses on the tissue were illustrated in Fig. 2.15b. With the most significant press force ($8N$), the maximum stresses were $14.1Kpa$ and $49Kpa$, respectively. As the pressing force grew from $2N$ to $8N$, the maximum stresses in soft design cases were 54%, 67%, 71%, and 71% lower than those in rigid design cases.

The experiment results for our soft camera and a rigid mock-up camera are shown in Fig. 2.15d. Applying $8N$ magnetic coupling force, the pressure information measured with the pressure mapping sensor in different belly curvature cases was displayed and recorded by the visualization software (SNOWFORCE3, Kitronyx). The contact area with the soft camera was larger than the area with the rigid design. The average maximum pressure results with the soft camera were $19.9Kpa$ and $32.6Kpa$ in lower and higher curvature cases individually, while they were $47.4Kpa$ and $64.2Kpa$ with the rigid camera. In lower curvature cases, the pressure was almost evenly distributed on two ends of the camera. However, larger contact areas and stress occurred at the lower end of the camera in higher curvature cases. This is because

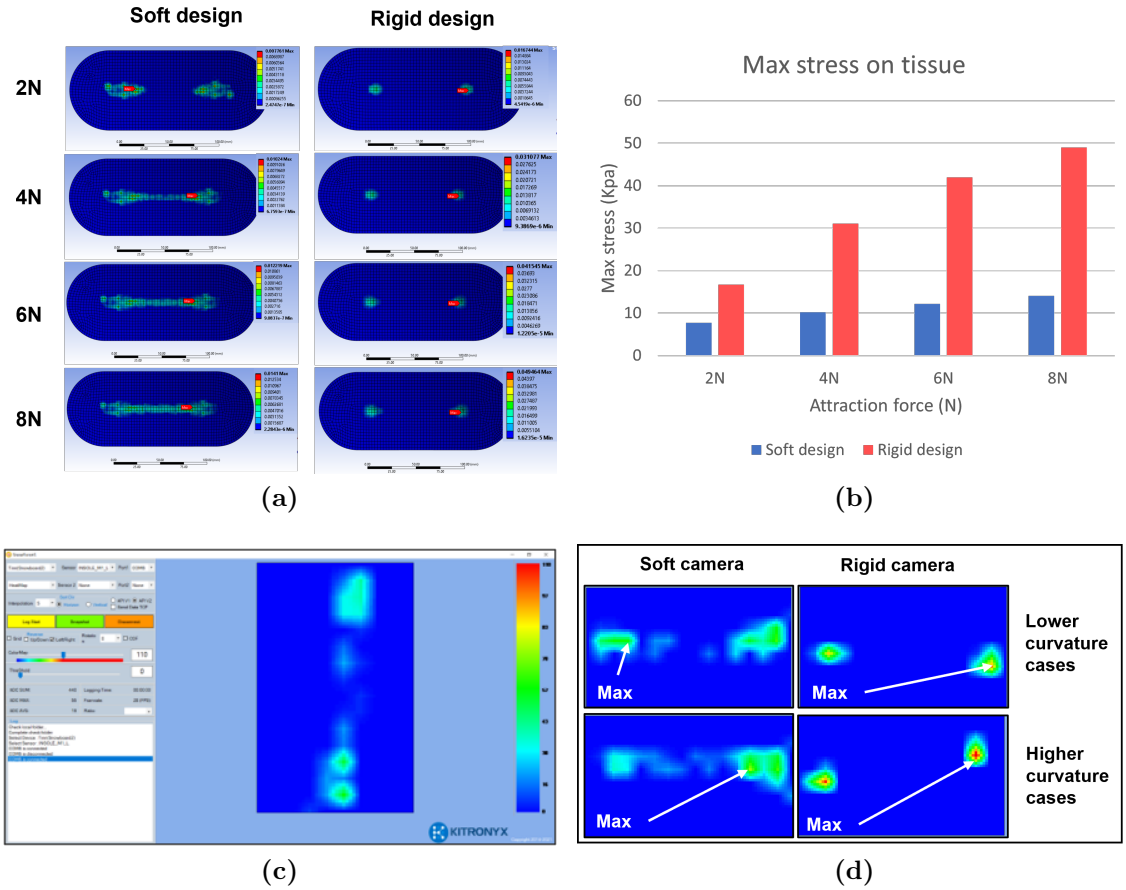

Figure 2.15: **a** Simulation comparison between soft and rigid designs in Ansys workbench. The contact area has a significant difference between the two cases. **b** Maximum stress comparison between soft and rigid designs in simulations. **c** Software client for visualizing the pressure data collected by pressure mapping sensor. **d** Pressure comparison between soft and rigid designs in different curvature cases.

the component force of the camera gravity generates an additional effect at the lower end of the camera.

Bendability of soft structure

The bendability test results are shown in Fig. 2.16. As the coupling force increased from $0N$ to $10.82N$, the camera's bending angle reached the maximum angle of 20°. The Maximum displacement of the tube cap along the vertical direction was $16.4mm$. Ten points were recorded and fitted into a linear function to establish the relationship between the bending angle and the coupling force. This provides a meaningful reference to understand the property of the design and optimize the design.

Demonstration of insertion procedure

The demonstrations of the insertion procedure were performed ten times. The total average operation time was 118 seconds. The process of one of the trials and the average duration of the four main steps were recorded and shown in Fig. 2.17. In the first step, the camera was supposed to slide into the trocar slowly and approach the EMP of the actuator. The second step took an average of 45 seconds, in which the actuator was controlled to attract the camera and drag it gently until the other end of the camera reached the exit of the trocar. The operation of the manipulator was constrained to a relatively low speed, and the force-torque sensor kept monitoring the coupling force in case of breaking the connection. The next step took an average of 33 seconds to rotate the actuator around the coupling end until the magnetic coupling on both ends was established. In the deployment step, the camera was thoroughly dragged out from the trocar and steered to the center of the belly model, providing a proper FOV, which took an average of 22s.

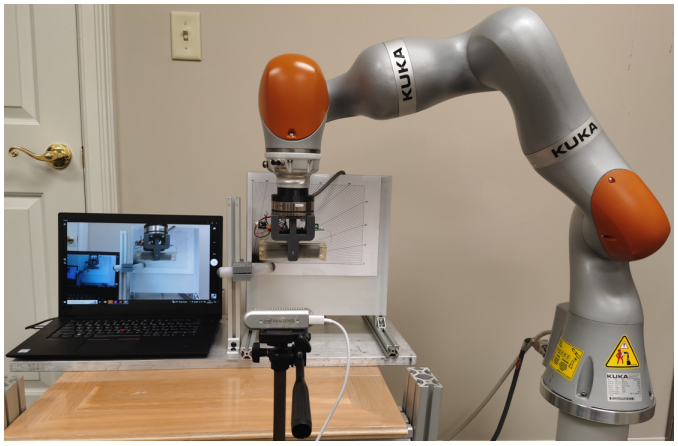

(a) Bendability test platform.

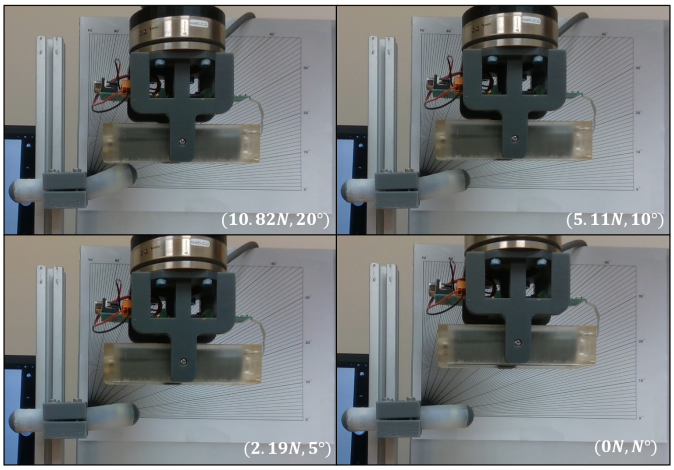

(b) Bendability test results.

Figure 2.16: Bendability test results were shown in (b). The attraction force and bending angle pairs were inserted at the corners. The relationship can be fitted with a linear function.

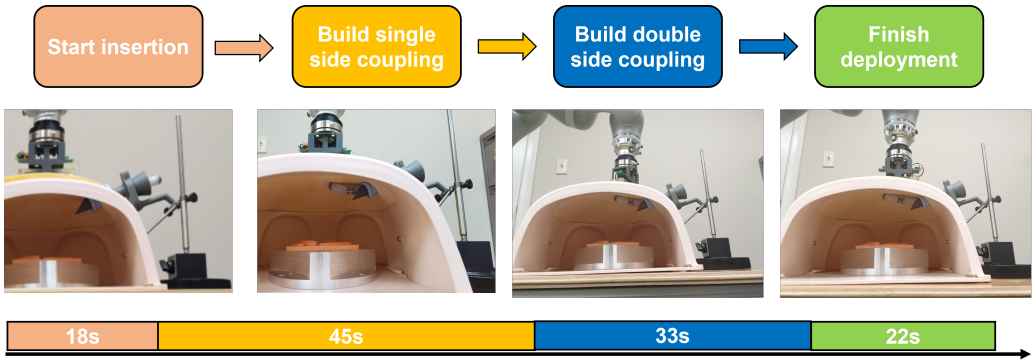

Figure 2.17: The four main steps of the insertion procedure were recorded. The average duration for each step is shown in the time bar.

2.7 Discussion and Conclusion

In the present study, we show the dexterous locomotion of the novel wireless laparoscope. The pure magnetic driven method grants the camera four DOF with significant panning and tilting motion range. After the insertion, the camera can be placed far away from the trocar, leaving the trocar for other instruments and offering a larger workspace. Thanks to the wheel structure design, the translation and tilting become much smoother. Compared with other existing systems [31][10][32], where the camera in the process of moving often appears suddenly shift due to dry friction, the video stream in our system is continuous and stable. Meanwhile, the operation with the assistance of the manipulator becomes more intuitive. As a result, the camera can be maneuvered to the work regions easily and provide desired FOV for the surgery, which takes no more than three minutes on average. The traditional laparoscope systems always require an assistant to handle it during surgery, which is exhausting. In our system, after the deployment, the manipulator can hold the external actuator still, contributing to keeping the camera steady for an extended period. Besides, the core components were well sealed by the silicone rubber and the transparent tube, and the device can be sterilized using low-temperature ethylene oxide. All the components, except for the camera board, are inexpensive and can be treated as disposable surgical consumables, streamlining the preparation and sterilization process. The above advantages suggest that the proposed system has the potential to outperform current laparoscopes in SILS.

Another improvement is the soft property of the camera design. Most of the MAGS [15][33][23][18][19] are developed based on rigid structures with sharp edges. The device will irreversibly damage the tissue when it is squeezed for a long time. When the camera is anchored on the curved abdominal wall, the two ends of the rigid frame will generate significant stress concentration. Our experiments show that this phenomenon is pronounced in places with higher curvature. The surgeons must keep adjusting the camera's position to avoid this issue, which consumes time and

distracts surgeons' attention. Our soft design gains the ability to passively bend along the curved tissue to create a larger contact area. Results from the simulations and experiments prove that the maximum stress generated by our soft structure can be diminished by 71% and 64%. The design is more friendly to tissue contact.

Meanwhile, the insertion procedure is a challenge that must be addressed. [10] introduced an endoluminal robot with a reconfigurable anchor frame design. However, the docking process was time-consuming and took about 30mins. In [32], the deployment had to be assisted by another inserted instrument and a standard laparoscope. The bending characteristics of our camera simplified the insertion, and the whole process took less than 2 minutes on average without the assistance of an additional instrument and laparoscope. This feature saves the preoperative preparation time of the laparoscope system and is vital for the practical application of the system from prototype to product.

The study has certain limitations. First, the prototype design of the external actuator is still relatively rudimentary. The Control board and wiring need to be better sealed, and in practice, the sterilization process may damage the electrical parts. Second, in the locomotion test, we observed that the camera was limited in operation in some regions, such as the area near the trocar, to avoid collision and interference. Moreover, the relative position information of the trocar and camera is missing, so we set aside an area to restrict the camera's access according to our estimation. The camera loses some working space as a result. Finally, the prototype of the present camera has a limited bending capability, only 20 degrees at the maximum magnetic attraction. Under this condition, the position and angle of trocar insertion are thus limited to a limited area, impacting the surgical protocol's flexibility. As a part of future work, we plan to (a) design a new external actuator with an enclosed frame, (b) explore the technical solution for 3D environmental reconstruction of the cavity, and (c) optimize the selection and layout of the components inside the camera and actuator to improve the bendability of the camera.

Chapter 3

Magnetic Localization for the Wireless Laparoscopic Camera

3.1 Introduction

Minimally invasive surgery (MIS) has experienced a significant surge in popularity over the past few decades [47], revolutionizing surgical instrumentation and enhancing patient comfort and surgeons' ease of operation. This progress has led to the emergence of single incision laparoscopic surgery (SILS) and computer-assisted robotic surgical systems as viable options for an expanding range of procedures [48][49]. SILS allows surgeons to perform delicate laparoscopic operations through a single entry port, typically located in the patient's navel, resulting in minimized trauma, reduced postoperative pain, and nearly invisible scarring. Simultaneously, robotic surgical systems offer unparalleled precision and intuitiveness, compensating for the increased complexity associated with SILS, such as device clashing and loss of triangulation [50]. Collectively, these techniques have provided superior surgical outcomes and improved operative experiences compared to traditional multi-port laparoscopic surgery. However, the movements of the laparoscope and other instruments remain confined within trocar channels, limiting their mobility and

subjecting them to the inherent fulcrum effect. Even with advanced systems like the *da Vinci* surgical robot, a dedicated trocar is still required for the laparoscope. In some instances, an additional incision becomes necessary to replace the laparoscope and achieve a preferred viewing angle during surgery [51].

A potentially promising concept involves the utilization of miniaturized imaging devices [52] and other functional surgical units [53] that can be entirely placed within the abdominal cavity through robotic means. These *in vivo* robots provide vision and task assistance within a larger workspace, free from the constraints of trocars, through appropriate magnetic or motorized actuation. Several proof-of-concept prototypes of insertable laparoscopic imaging devices have been proposed to demonstrate their capabilities, kinematic flexibility, and technical feasibility to varying extents. These designs primarily consist of magnetic anchoring and guidance systems (MAGS) [54], either with tethering wires for power and communication [55][32][56][13] or without them [23][19][57]. Compared to motorized solutions that require mechanical attachment [58] or suturing onto the abdominal wall [59], magnetic coupling enables more flexible mobility of *in vivo* cameras through non-contact transabdominal actuation. However, it is important to note that although the magnetic field can penetrate the human body with minimal attenuation, its strength diminishes exponentially with distance. This inherent limitation hampers camera controllability [60]. Particularly when dealing with morbidly obese patients and complex viscoelastic interactions between the camera and tissue, there is a risk of losing track of the camera due to backlash and sluggish effects, further exacerbating the challenges associated with precise motion control.

Regrettably, most of the current state-of-the-art works in this field operate using open-loop control, lacking the capability to track the pose of the camera. Consequently, these approaches suffer from mediocre locomotion precision and limited robustness to environmental uncertainties [13][12][23][19]. The camera often deviates from the intended trajectory, leading to a disconnection between the magnetic coupling and the actuator. It is important to emphasize that spatial information

plays a critical role in surgical workflow, as reported in the literature [61][62]. Optical techniques based on laparoscopic vision have demonstrated the ability to reconstruct 3D organ surfaces [62][63] and track surgical instruments relative to the camera's coordinate frame [64]. Therefore, having knowledge of camera motion and pose can not only help stabilize laparoscopic imaging and provide feedback for precise camera control but also facilitate operation planning and enhance intraoperative navigation by registering the recovered in-situ data with the robot's coordinate frame or preoperative medical images. Li proposed a visual servo control method; however, it relies on weak assumptions and simplified models, where it is assumed that the magnets are always aligned, and the dynamics of tissue contact are disregarded [65]. Similar research has been demonstrated for wireless capsule endoscopes (WCE) in the gastrointestinal tract [66], where the camera locomotes slowly and the camera pose, tracked either by a vision system or a magnetic sensor, is utilized for closed-loop control and model predictive control [67][68][69]. The localization of our laparoscope encounters specific technical challenges. Firstly, the accurate orientation of the untethered camera must be estimated in a wireless manner under dynamic magnetic interference from multiple movable permanent magnets. Secondly, unlike localization systems for wireless capsule endoscopes (WCE), which can afford to have their localization data post-processed offline by a human reviewer, our laparoscope localization system must operate in real-time, with an acceptable update rate. This real-time tracking enables immediate and responsive closed-loop control, enhancing the effectiveness and safety of the surgical procedure.

Several localization techniques have been explored as feasible solutions for transabdominal operations compatible with magnetic manipulation [24], including electromagnetic waves[25], emission markers[28], and image processing [29]. However, these methods suffer from signal attenuation or impractical implementation, making magnetic localization the most practical and reliable method with minimal estimation errors. Magnetic localization techniques can be categorized into external sensor arrays [70] or internal sensor integration [68][69][71][72][73]. External sensor arrays

require additional setup steps in the operating room and have a limited measurement range. On the other hand, the internal sensor method involves embedding sensors into the in vivo device to track the camera's pose relative to the external magnetic actuator.

The current internal sensor method faces challenges in design and drift problems. In [71], a wireless capsule endoscope (WCE) is actuated by a rotating permanent magnet (RPM), and six linear Hall-effect sensors are placed around the internal magnet for localization. The error is within $7mm$ and $5°$. However, the sensor configuration requires a camera design with a large diameter and a wide access port, making it less suitable for current magnetic laparoscopic designs. Additionally, the localization algorithm relies on RPM actuation, which results in unstable video, further limiting its applicability. Another approach proposed by Natali [73][74] overcomes the limitations of the single dipole model by establishing a pre-calculated magnetic field map based on finite-element solutions. They use an iterative method to achieve real-time pose estimation of the internal capsule without relying on the dipole model assumption. However, the yaw angle estimation tends to drift over time due to the iterative integration based on IMU sensing.

In this Chapter, we propose a 6-DOF magnetic localization method for a magnetically driven laparoscope integrated IMU, magnetic sensor, and double permanent magnet pairs. The roll and pitch angle of the camera without drift is acquired by a complementary filter based on IMU measurement. Designed with double magnet pairs, the internal camera works within a relative region where the coupling force is sufficient and the mapping relationship from the relative pose to magnetic field measurement can be accurately modeled by two single dipole models. The 3-DOF position and yaw angle are obtained directly by the inverse mapping and Newton-Raphson method without suffering from drift. The remaining of this paper is organized as follows: Section 3.2 described the system design and operation principle; Section 3.3 and Section 3.4 respectively provide technical details on the kinematic modeling approach and the localization algorithm; and Section 3.5

presents experiments conducted for localization performance and result analysis; finally, concluding remarks with the vision into the future are made in Section 3.6.

3.2 System Overview And Operation Principle

The wireless laparoscope is designed as a subsystem of a RAS system. To ensure a clear understanding of the pose estimation problem for the insertable laparoscopic camera, an overview of the RAS system will be provided first in this section followed by the operation principle of actuation and localization. The main objective of the RAS system is to enable flexible camera mobility within the abdominal cavity, enhancing surgical vision assistance. It is designed with a focus on transabdominal magnetic actuation, eliminating the need for cumbersome tethering wires connected to the camera. The feasibility of this design concept has been validated through initial experimental results obtained from the prototype. These experiments were conducted in an *ex vivo* synthetic abdominal setting, showcasing the system's capability to perform various basic laparoscopic functions in Section 2.

3.2.1 Design of the Intra-abdominal Wireless Laparoscope

Fig. 3.1 provides a conceptual illustration of the RAS system, highlighting its key components and their interactions. The system consists of a wireless camera, an external actuator, a force-torque sensor, and a multi-degree-of-freedom collaborative manipulator. The camera and actuator are equipped with two pairs of permanent magnets. which generates a robust magnetic coupling force that serves to anchor and navigate the camera against the abdominal wall. Borrowing the principle of spherical motors, the camera rotor is actuated to rotate (yaw, pitch, and roll) in a three-dimensional (3D) space by appropriately adjusting magnetic fields generated by the actuator. The force-torque sensor plays a vital role in monitoring the contact

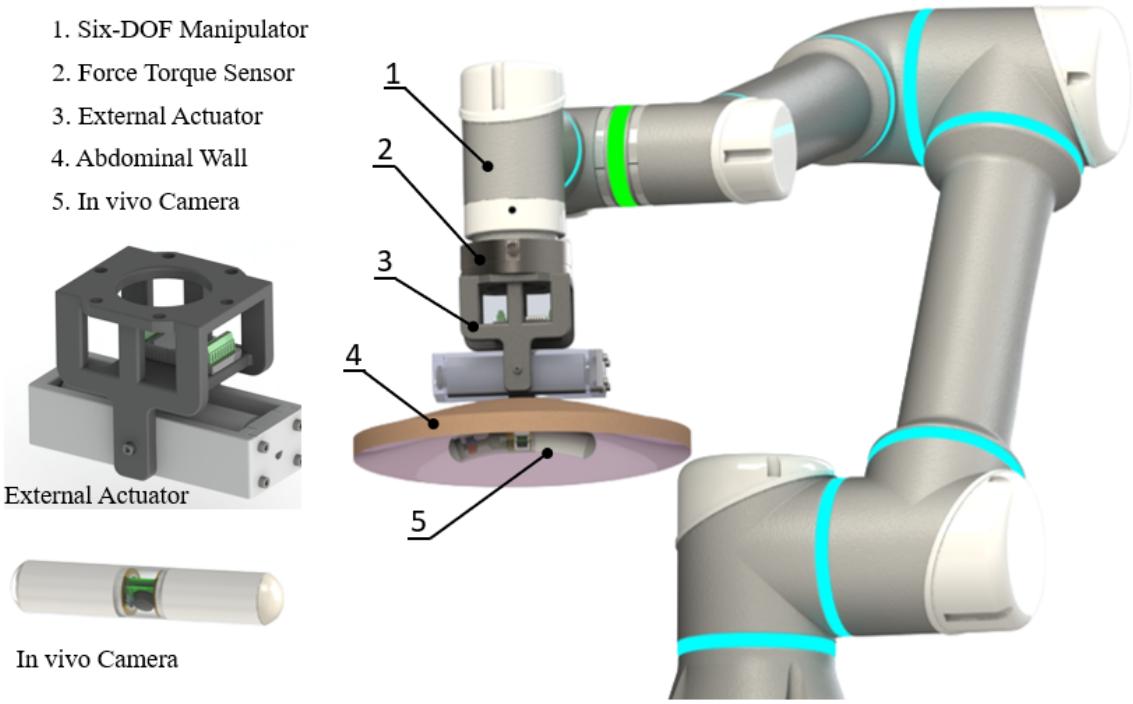

Figure 3.1: Overview of a robotic surgical system. The proposed wireless laparoscopic camera works as a subsystem including an external actuator and an in vivo camera module.

force between the camera and the patient's tissue. It ensures that the camera exerts an appropriate level of pressure while maintaining sufficient coupling with the abdominal wall. During the surgical operation, the camera can be introduced into the insufflated abdominal cavity through a SILS port after the patient gets appropriate anesthesia, then steered to the desired anchor position. The SILS port becomes available for the introduction of other surgical instruments, maximizing the surgical workspace and minimizing the number of incisions required.

The camera design is compact, with dimensions of $20mm$ in diameter and $100mm$ in length. The camera features a soft structure and a wheeled-structure design to establish friendly contact between the camera and the tissue, minimizing the potential for tissue damage or discomfort during the surgical procedure. The internal structure of the camera is symmetric and consists of several components, including two internal permanent magnets (IPM), ball bearings, soft shafts and tubes made with silicone rubber, battery packages, sleeve bearings, a PCB board, a lens, and a clear PVC tube. The IPMs are identical ring magnets, diametrically magnetized, and made with Grade 42 NdFeB. They are positioned at each end of the camera to couple with the external permanent magnets (EPMs) embedded in the external actuator. The $75mm$ gap between the IPMs is designed to provide high rotating torque while avoiding magnetic interaction. The camera board is powered by an FDA-approved onboard power source and enables video streaming and control communication through wireless approaches. Multiple onboard sensory abilities have been integrated for camera state monitoring, including an embedded miniature IMU (MPU-9250) comprising a 3-axis gyroscope and a 3-axis accelerometer, as well as a 3D linear Hall-effect magnetometer (MAG). The camera board is fixed with two sleeve bearings. Two soft shafts made with silicone rubber, carrying the IPMs and battery packages, are supported by ball bearings and sleeve bearings.

The camera board, IPMs, bearings, and soft shafts can be assembled as an internal module and inserted into the tubes. The two pairs of bearings create the wheeled structure, enabling the internal module to rotate freely with respect to the camera

tube. The soft tubes, clear PVC tubes, and tube caps form an enclosure space, sealing all the components inside the camera. Except for the camera board, all the components are low-cost and can be treated as surgical consumables, simplifying the preparation and sterilization procedure.

Moving on to the external actuator, it is 3D printed with photopolymer using an SLA printer. It features a connection interface part used to mount the housing onto the force-torque sensor and establish a connection with the manipulator. The actuator housing accommodates two EPMs, which are inserted into the rotor housing and supported by two ball bearings. The rotor housing can rotate inside the actuator housing. To control the rotation of the EPMs with respect to the housing, a 24V micromotor (1016M009SR, FAULHABER) is integrated into the rotor. The motor is equipped with a 256:1 ratio gearhead, enabling it to generate $1Nm$ of torque. The motor is connected and controlled by a driver board through a flexible flat cable mounted onto the connection interface part.

3.2.2 Magnetic Actuation and Localization Principle

Fig. 3.2 illustrates the magnetic actuation mechanism and the layout of components inside the modules. The actuator, camera frame $\{a\}$, and camera frame $\{c\}$ are fixed with the centers of the actuator roller and the camera board, respectively. The directions z_a and z_c are parallel to the pole directions of the magnets. The camera-actuator distance D affects the pressure on the tissue and the magnetic coupling force.

Driven by the manipulator, the EPMs can enable the camera to translate along the abdominal wall and pan around z_c. The tilt motion around y_c is achieved by actuating the micromotor inside the actuator to rotate around y_a. With the wheeled structure design, when the external actuator drives the camera to translate along x_c and tilt around y_c, the tubes function as wheels rolling along the abdominal wall. This design replaces the common sliding motions found in existing designs with rolling

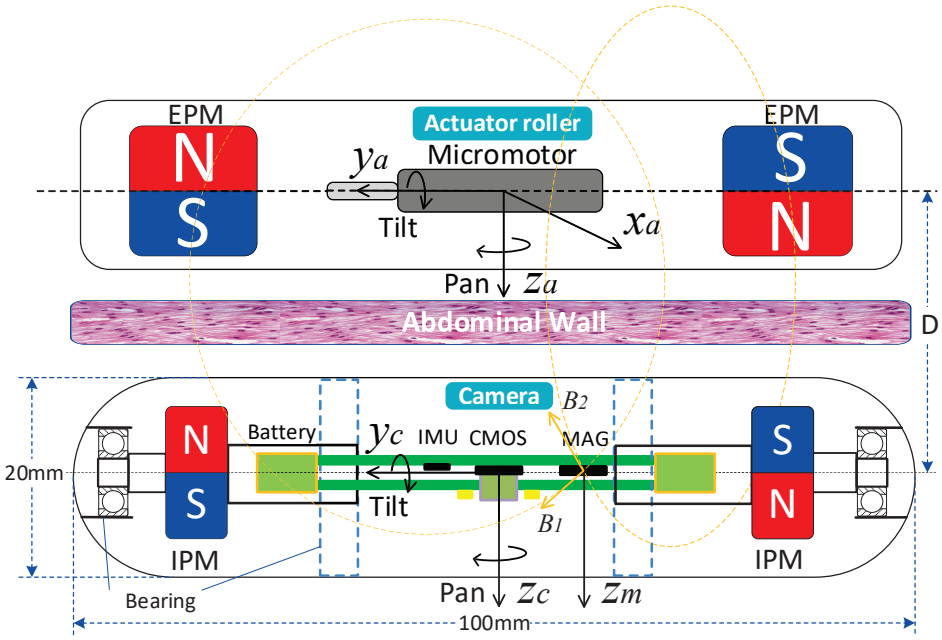

Figure 3.2: Magnetic-based actuation and localization mechanism. The camera has 4-DOF including 2-DOF translation, tilt, and pan. The IMU is used for tracking the pitch and roll angles of the camera with respect to the world frame. Subtracting the effects from the IPMs, the MAG collects the magnetic fields B_1 and B_2 due to the EPMs.

motions. The rolling motion achieves smoother and less laggy tilt and translation motions, which in turn expedite accurate pose tracking due to the stable coupling. The dry friction between the camera and tissue is minimized, and the rolling friction is considered negligible. This feature not only protects the tissue from potential damage but also simplifies the friction model and facilitates fast response in dynamic control.

In terms of localization, real-time pose feedback with respect to the actuator is critical for the robotic precise motion control of this novel surgical camera. As is indicated in Fig. 3.1, the actuator is held by the robotic arm as an end effector whose pose with respect to the robot base could be conveniently computed using forward kinematics. Meanwhile, the robot base is mounted at a known location in the operating room. Thus, the camera pose, once established, could be easily transformed between the actuator coordinate frame and the world coordinate frame. Many other surgical augmentations could be achieved after the camera pose is registered into the world coordinate frame in the operating room.

Although various implementations of attitude and heading reference systems (AHRS) based on an IMU aided with a 3-axis magnetometer have been documented [75], they are typically suitable for applications where the geomagnetic field can be reliably observed as a heading reference. However, in the presence of a strong magnetic field generated by the EPMs, calculating the yaw angle becomes challenging without an absolute reference. Natali proposed an estimation method that utilizes the axis-angle method for rotational matrices applied to gyroscope outputs [74]. Unfortunately, this approach is prone to error accumulation over time, thus impacting the precision of localization. To address these limitations and enable real-time control feedback in a robust manner within a strong dynamic magnetic environment, an effective approach must fulfill the following requirements: (i) the estimation method should possess the ability to counteract magnetic interference effectively, ensuring reliable and accurate results, and (ii) the pose update rate should be sufficiently high to meet the demands of feedback-intensive control tasks, such as image stabilization.

In the proposed design, the arrangement of the double external permanent magnets (EPMs) involves placing their magnetic poles in an antiparallel configuration. This arrangement ensures that every position point below the EPMs exhibits a unique magnetic field vector, except for the singularity plane known as the $x_a z_a - plane$. By utilizing the onboard magnetic field (MAG) measurement, it becomes possible to determine the yaw angle and the relative position between the camera and the actuator. The MAG center frame, denoted as m, is positioned along the center line of the camera board, between the two internal permanent magnets (IPMs). The frame $\{m\}$ remains aligned with the frame $\{c\}$, which represents the camera module. To avoid a singularity issue during initialization, the MAG is not placed in the middle plane between the two IPMs. Instead, an offset is introduced between the c and m frames. Since the MAG rotates along with the IPMs, the bias reading caused by the IPMs remains constant.

Furthermore, the IPMs' magnetic poles are arranged in an antiparallel manner to align with the EPMs. The magnetic field vectors generated by the IPMs at the $\{m\}$ frame coincide with the z_m axis and point in opposite directions, effectively minimizing the bias reading. By subtracting the bias reading, the MAG can measure the magnetic fields B_1 and B_2 resulting from the two EPMs, which depend on the relative pose between each EPM and the MAG. By establishing a relationship mapping from the relative pose to the MAG measurement, it becomes possible to solve for the position and yaw angle of the camera using an inverse solution, where the pose of the actuator is known through the forward kinematics of the manipulator.

3.3 MODELING APPROACH

A stable pose estimation technique has been implemented using an IMU attitude reference system in conjunction with robotic kinematic reference and magnetic observation. The IMU is positioned on the camera body to capture motion-related

data, such as angular rates and linear accelerations. In addition, the MAG is utilized to gather magnetic field information generated by two EPMs.

The camera's pose is supposed to be expressed in a selected world frame. The orientation is formulated with Euler angles and quaternions. The relationship between the camera's pose, and the MAG measurement is established by formulating a magnetic model based on the design of the double magnet pairs, employing the single dipole model. Table 3.1 shows the nomenclature used in this section.

3.3.1 Coordinate frame and kinematic modeling

According to the design and application environment, the camera is essentially a rigid body levitated inside the 3D abdominal cavity against soft tissues with six DOFs (3D translation and 3D rotation). In order to mathematically depict the kinematic model of the RAS system, a series of coordinate frames have been determined as is shown in the schematic Fig. 3.3. The world coordinate frame in the operating room is referred to as the inertial coordinate frame $\{w\}$ which coincides with the base frame of the manipulator.

The robotic end effector frame $\{a\}$ is assigned to the center of actuator housing, where x_a sits on the center line of the actuator, z_a is parallel to the magnetic pole direction of the left EPM, and y_a is determined by the right-hand rule. $\boldsymbol{T_a^w}$ represents the transition of the frame $\{a\}$ with respect to the $\{w\}$ which is obtained from the forward kinematic of the manipulator with known joint angles. Two EPM frames $\{a_1\}$ and $\{a_2\}$ are at the centers of the EPMs and have the same orientation as $\{a\}$.

Table 3.1: Notations for Pose Estimation Modeling

Symbol(s)	Meaning
m_a	Lowercase regular font refers to scalar.
$\boldsymbol{p^w}$	Lowercase bold font refers to a vector expressed in frame $\{w\}$.
$\boldsymbol{\hat{p}}$	Normalized unit vector.
$\boldsymbol{R_a^w}, \boldsymbol{T_a^w}$	Rotation and transformation matrix represent the orientation and transformation of $\{a\}$ with respect to $\{w\}$.
$\boldsymbol{I_n}$	Matrix refers to $n \times n$ identity matrix.
$Rot_k(\theta)$	Matrix represents the rotation of θ degrees around the $+k$ axis.
$\otimes$	Kronecker product.

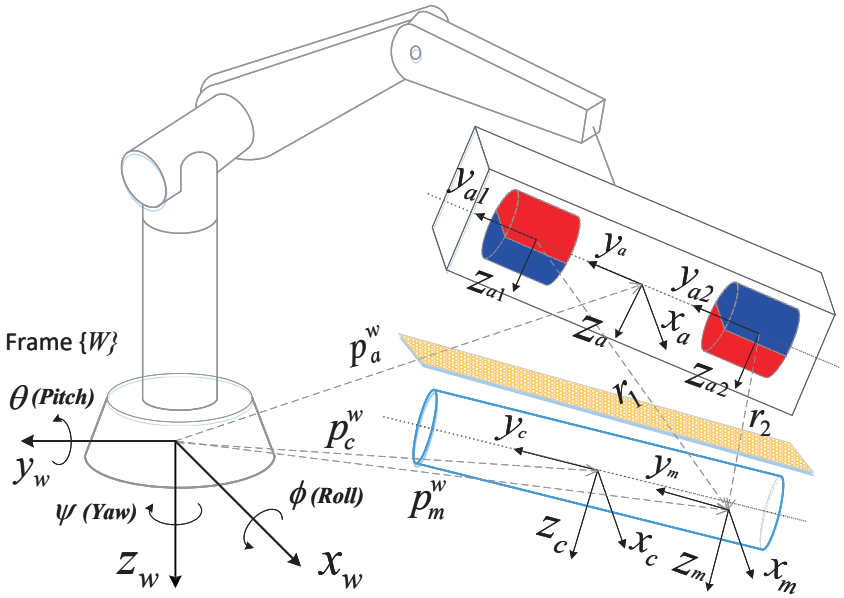

Figure 3.3: Coordinate frames of the system. World frame $\{w\}$ coincides with the base frame of the manipulator, $\{a\}$, $\{c\}$ and $\{m\}$ represent the actuator, camera and MAG center frame. The poses are expressed by p_a^w, p_c^w, p_m^w, and Euler angles. Frame $\{m\}$ is fixed on the center line of the camera and has the same orientation as $\{c\}$.

$l = 37.5mm$ defines the distance between $\{a_i\}$ and $\{a\}$. Vector $\boldsymbol{p}_{\boldsymbol{a_1}}^{\boldsymbol{a}} = \begin{bmatrix} l & 0 & 0 \end{bmatrix}^T$ and $\boldsymbol{p}_{\boldsymbol{a_2}}^{\boldsymbol{a}} = \begin{bmatrix} -l & 0 & 0 \end{bmatrix}^T$ represent the position of each EPM with respect to $\{a\}$, which can be used to calculate $\boldsymbol{T}_{\boldsymbol{a_1}}^{\boldsymbol{w}}$ and $\boldsymbol{T}_{\boldsymbol{a_2}}^{\boldsymbol{w}}$ with

$$\boldsymbol{T}_{\boldsymbol{a_i}}^{\boldsymbol{w}} = \boldsymbol{T}_{\boldsymbol{a}}^{\boldsymbol{w}} \boldsymbol{T}_{\boldsymbol{a_i}}^{\boldsymbol{a}} = \begin{bmatrix} \boldsymbol{R}_{\boldsymbol{a_i}}^{\boldsymbol{w}} & \boldsymbol{p}_{\boldsymbol{a_i}}^{\boldsymbol{w}} \\ 0 & 1 \end{bmatrix} \tag{3.1}$$

where $\boldsymbol{T}_{\boldsymbol{a_i}}^{\boldsymbol{a}}$ are given by:

$$\boldsymbol{T}_{\boldsymbol{a_i}}^{\boldsymbol{a}} = \begin{bmatrix} \boldsymbol{I_3} & \boldsymbol{p}_{\boldsymbol{a_i}}^{\boldsymbol{a}} \\ 0 & 1 \end{bmatrix}, \ i = 1, 2 \tag{3.2}$$

The body frame of the camera $\{c\}$ locates at the center of the camera board, in which x_c is the sliding direction and points to the center of the left IPM, and z_c is parallel to the magnetic pole direction of the IPMs and the view direction of the CMOS sensor. Matrix $\boldsymbol{T}_{\boldsymbol{c}}^{\boldsymbol{w}}$ describes the pose of frame $\{c\}$ in $\{w\}$,

$$\boldsymbol{T}_{\boldsymbol{c}}^{\boldsymbol{w}} = \begin{bmatrix} \boldsymbol{R}_{\boldsymbol{c}}^{\boldsymbol{w}} & \boldsymbol{p}_{\boldsymbol{c}}^{\boldsymbol{w}} \\ 0 & 1 \end{bmatrix} \tag{3.3}$$

where the vector $\boldsymbol{p}_{\boldsymbol{c}}^{\boldsymbol{w}}$ and the rotation matrix $\boldsymbol{R}_{\boldsymbol{c}}^{\boldsymbol{w}}$ express the camera's position and orientation relative to $\{w\}$.

For the orientation description of the camera in a 3D space, Euler angles are intuitive and easy to use in terms of control purposes. According to different rotation sequences, there exist 12 sets of Euler angels. Unless specified otherwise, the Z-Y-X set of Euler angels (ϕ, θ, ψ), which is so-called aerospace sequence set, will be used in this work for depicting roll, pitch (tilt), and yaw (pan) of the camera. Then, the rotation matrix $\boldsymbol{R}_{\boldsymbol{c}}^{\boldsymbol{w}}$ can be expressed with the direction cosine matrix (DMC)

$$
\begin{aligned}
\boldsymbol{R}_{\boldsymbol{c}}^{\boldsymbol{w}} &= Rot_z(\psi_c)Rot_y(\theta_c)Rot_x(\phi_c) \\
&= \begin{bmatrix} cos\theta cos\psi & sin\phi sin\theta cos\psi - cos\phi sin\psi & cos\phi sin\theta cos\psi + sin\phi sin\psi \\ cos\theta sin\psi & sin\phi sin\theta sin\psi + cos\phi cos\psi & cos\phi sin\theta sin\psi - sin\phi cos\psi \\ -sin\theta & sin\phi cos\theta & cos\phi cos\theta \end{bmatrix}
\end{aligned} \tag{3.4}
$$

With angular rate vector $\boldsymbol{\omega^c} = \begin{bmatrix} \omega_x^c & \omega_y^c & \omega_z^c \end{bmatrix}^T$ measured in the rotor coordinate frame, the rotation differential equation of Euler angles could be given as (3.5). However, as $cos\theta$ approaches zero, solution accuracy of (3.5) degrades quickly, which implies this equation is not able to work in the full orientation space. Besides, Euler angles are computational costs by computing massive trigonometric functions.

$$
\begin{bmatrix} \dot{\phi} \\ \dot{\theta} \\ \dot{\psi} \end{bmatrix} = \frac{1}{cos\theta} \begin{bmatrix} cos\theta & sin\theta sin\phi & sin\theta cos\phi \\ 0 & cos\theta cos\phi & -cos\theta sin\phi \\ 0 & sin\phi & cos\phi \end{bmatrix} \begin{bmatrix} \omega_x^c \\ \omega_y^c \\ \omega_z^c \end{bmatrix} \tag{3.5}
$$

To eliminate the singularity problem with (3.5) and reduce the computational burden, quaternions mathematics have been used for the formulation of the rotation differential equation, which works in the full attitude space with only algebraic computations. The orientation of the camera with respect to the frame $\{w\}$ can be expressed by a quaternion

$$
\boldsymbol{q}_{\boldsymbol{c}}^{\boldsymbol{w}} = \begin{bmatrix} q_0 \\ \boldsymbol{q_r} \end{bmatrix} = \begin{bmatrix} cos\frac{\vartheta}{2} \\ \hat{\boldsymbol{r^w}} sin\frac{\vartheta}{2} \end{bmatrix} \tag{3.6}
$$

where q_0 is the real-scalr part and $\boldsymbol{q_r} = q_1\boldsymbol{i} + q_2\boldsymbol{j} + q_3\boldsymbol{k}$ is the vector-imaginary part. $\hat{\boldsymbol{r^w}} \in \mathbb{R}^3$ is the unit rotation vector expressed in frame $\{w\}$ and ϑ is the rotation angle. Any three dimensional vector $\boldsymbol{v^c}$ described in frame $\{c\}$ can be expressed as $\boldsymbol{v^w}$ in frame $\{w\}$ with a rotation transformation

$$
\begin{aligned}
\begin{bmatrix} 0 \\ \boldsymbol{v^w} \end{bmatrix} &= \boldsymbol{q_c^w} \otimes \begin{bmatrix} 0 \\ \boldsymbol{v^c} \end{bmatrix} \otimes \boldsymbol{q_c^{w*}} \\
&= \begin{bmatrix} 1 & 0 & 0 & 0 \\ 0 & 1-2q_2^2-2q_3^2 & 2q_1q_2-2q_0q_3 & 2q_0q_2+2q_1q_3 \\ 0 & 2q_1q_2+2q_0q_3 & 1-2q_1^2-2q_3^2 & 2q_2q_3-2q_0q_1 \\ 0 & 2q_1q_3-2q_0q_2 & 2q_0q_1+2q_2q_3 & 1-2q_1^2-2q_2^2 \end{bmatrix} \begin{bmatrix} 0 \\ \boldsymbol{v^c} \end{bmatrix}
\end{aligned} \tag{3.7}
$$

where $\boldsymbol{q_c^{w*}} = \begin{bmatrix} q_0 & \boldsymbol{q_r} \end{bmatrix}^T$ is the conjugate transpose of the quaternion (3.6). $\otimes$ denotes the Kronecker product. Given the angular rate vector $\boldsymbol{\omega^c}$, the rotation differential equation of the quaternion can be solved with equation (3.8) and equation (3.9) that found in [76]

$$
\frac{d\boldsymbol{q_c^w}(t)}{t} = f\left(\boldsymbol{q_c^w}(t), \omega^c(t)\right) \tag{3.8}
$$

$$
\dot{\boldsymbol{q}}_{\boldsymbol{c}}^{\boldsymbol{w}} = \frac{1}{2}\boldsymbol{q_c^w} \otimes \begin{bmatrix} 0 \\ \boldsymbol{\omega^c} \end{bmatrix} = \frac{1}{2}\begin{bmatrix} 0 & -\omega_x^c & -\omega_y^c & -\omega_z^c \\ \omega_x^c & 0 & -\omega_z^c & \omega_y^c \\ \omega_y^c & \omega_z^c & 0 & -\omega_x^c \\ \omega_z^c & -\omega_y^c & \omega_x^c & 0 \end{bmatrix} \begin{bmatrix} q_0 \\ q_1 \\ q_2 \\ q_3 \end{bmatrix} \tag{3.9}
$$

After the orientation is calculated, it's easy to convert quaternions and Euler angles to each other. The orientation described by $\boldsymbol{q_c^w}$ is equivalent to the rotation matrix $\boldsymbol{R_c^w}$ defined in equation (3.4). The conversions between quaternions and Euler angles are as follows:

$$
\begin{bmatrix} \phi \\ \theta \\ \psi \end{bmatrix} = \begin{bmatrix} arctan\left(\dfrac{2(q_0q_1+q_2q_3)}{q_0^2+q_3^2-q_1^2-q_2^2}\right) \\ arcsin\left(2(q_0q_2-q_1q_3)\right) \\ arctan\left(\dfrac{2(q_0q_3+q_1q_2)}{q_0^2+q_2^2-q_1^2-q_3^2}\right) \end{bmatrix} \tag{3.10}
$$

$$\begin{bmatrix} q_0 \\ q_1 \\ q_2 \\ q_3 \end{bmatrix} = \begin{bmatrix} cos\frac{\phi}{2}cos\frac{\theta}{2}cos\frac{\psi}{2} + sin\frac{\phi}{2}sin\frac{\theta}{2}sin\frac{\psi}{2} \\ sin\frac{\phi}{2}cos\frac{\theta}{2}cos\frac{\psi}{2} - cos\frac{\phi}{2}sin\frac{\theta}{2}sin\frac{\psi}{2} \\ cos\frac{\phi}{2}sin\frac{\theta}{2}cos\frac{\psi}{2} + sin\frac{\phi}{2}cos\frac{\theta}{2}sin\frac{\psi}{2} \\ cos\frac{\phi}{2}cos\frac{\theta}{2}sin\frac{\psi}{2} - sin\frac{\phi}{2}sin\frac{\theta}{2}cos\frac{\psi}{2} \end{bmatrix} \tag{3.11}$$

3.3.2 Modeling of Forward Magnetic Relationship

Forward magnetic relationship establishes the mapping from the camera pose in world frame $\{w\}$ to the MAG measurement, laying the foundation for solving the inverse mapping. In forward mapping, we assume $\boldsymbol{T_c^w}$ is known for calculating the MAG data. The MAG center frame $\{m\}$ is placed on the axis X_c with a known offset $\boldsymbol{p_m^c} = \begin{bmatrix} 0 & -d & 0 \end{bmatrix}^T$ for avoiding singularity issue, where $d = 8mm$. Then the pose of the MAG can be described in $\{w\}$ as

$$\boldsymbol{T_m^w} = \boldsymbol{T_c^w T_m^c} \begin{bmatrix} \boldsymbol{R_m^w} & \boldsymbol{p_m^w} \\ 0 & 1 \end{bmatrix} \tag{3.12}$$

where $\boldsymbol{T_m^c}$ is known according to the layout of the MAG inside te camera and is given by:

$$\boldsymbol{T_m^c} = \begin{bmatrix} \boldsymbol{I_3} & \boldsymbol{p_m^c} \\ 0 & 1 \end{bmatrix} \tag{3.13}$$

In [77], the error of dipole approximation for the magnetic field of cylinder magnets drops to below 2% when the distance is larger than 1.5 radii of the minimum bounding sphere of the magnets. Considering the pressure on the tissue and the coupling force, the actuator-camera distance is controlled from $35mm$ to $55mm$ for our system [46]. This is sufficient for the assumption that the point-dipole model can accurately represent the magnetic field generated by each EPM. According to [78], the field $\boldsymbol{b^w}$ at any camera pose expressed in $\{w\}$ can be obtained with:

$$\boldsymbol{b^w} = \sum_{i=1}^{n} \left[\frac{\mu_0}{4\pi} \left(\frac{3\boldsymbol{r_i}\left(\boldsymbol{m_i} \cdot \boldsymbol{r_i}\right)}{\|\boldsymbol{r_i}\|^5} - \frac{\boldsymbol{m_i}}{\|\boldsymbol{r_i}\|^3} \right) \right] \tag{3.14}$$

where $\boldsymbol{m_i}$ is the magnetic moment of the ith EPM expressed in $\{w\}$, which always points from the south pole to the north pole inside the magnets and can be calculated by

$$\boldsymbol{m_1} = \boldsymbol{R}^{\boldsymbol{w}}_{\boldsymbol{a_1}} \begin{bmatrix} 0 \\ 0 \\ -m_a \end{bmatrix}, \ \boldsymbol{m_2} = \boldsymbol{R}^{\boldsymbol{w}}_{\boldsymbol{a_2}} \begin{bmatrix} 0 \\ 0 \\ m_a \end{bmatrix} \tag{3.15}$$

where m_a is the magnitude of the EPM dipole. $\boldsymbol{r}^{\boldsymbol{w}}_{\boldsymbol{i}} = \boldsymbol{p}^{\boldsymbol{w}}_{\boldsymbol{m}} - \boldsymbol{p}^{\boldsymbol{w}}_{\boldsymbol{a_i}}$ represents the position vector points from each EPM to the MAG center frame $\{m\}$, in which $\boldsymbol{p}^{\boldsymbol{w}}_{\boldsymbol{a_i}}$ and $\boldsymbol{p}^{\boldsymbol{w}}_{\boldsymbol{m}}$ can be found in equation (3.1) and (3.13). μ_0 is the permeability of free space. The last step is to transfer the $\boldsymbol{b^w}$ to $\{m\}$, and the MAG measurement can be expressed by

$$\begin{bmatrix} \boldsymbol{b^m} \\ 1 \end{bmatrix} = \boldsymbol{T}^{\boldsymbol{w}}_{\boldsymbol{m}} \begin{bmatrix} \boldsymbol{b^w} \\ 1 \end{bmatrix} \tag{3.16}$$

3.4 Localization Algorithm for the Wireless Laparoscope

The magnetic localization algorithm based on multiple sensors is demonstrated in Fig. 3.4. The inputs contain the actuator pose, the acceleration and gyro measurement from IMU, and the magnetic field vectors provided by the MAG. The core of the algorithm is composed of a Madgwick complementary filter and iteration algorithm based on the Newton-Raphson method. Affected by the strong magnetic fields generated by the EPMs dynamically, the Madgwick complementary filter fails to find a magnetic field vector as an absolute reference for solving the yaw angle without drift, while it can provide fast and accurate estimations for the roll and pitch angle

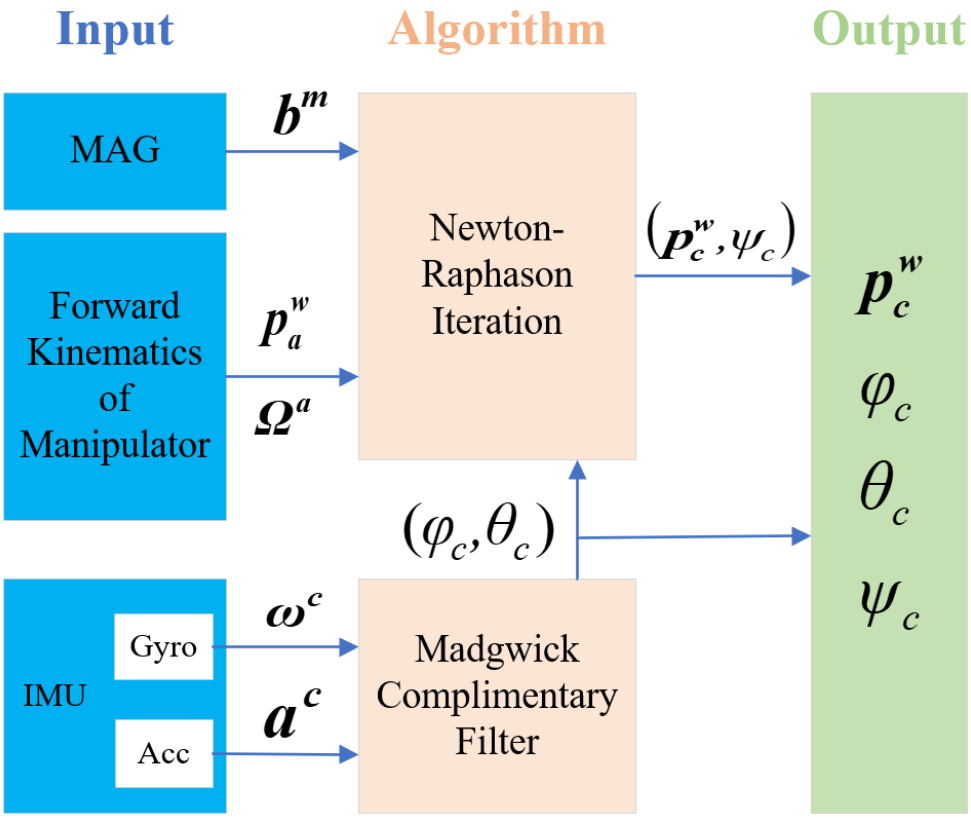

Figure 3.4: Block diagram of proposed localization method.

of the camera. The yaw angle and the position of the camera are directly solved by the inverse mapping from the magnetic field measurement to the relative pose between the sensor frame and EPM frames. The roll and pitch angles estimated by Madgwick filter are input into the iteration method to make it converge faster.

3.4.1 Madgwick Complementary Filter

According to the kinematic analysis, quaternions of the camera have been chosen as state variables for solving the roll and pitch angle. Since we have redundant measurements to update the same state variables of interest independently, the Madgwick filter has been applied for fusing these data from multiple sensors. The Madgwick filter is a glorified complementary filter with significant improvements to accuracy without significant markup in computation time. It is simple to tune and suitable for real-time applications. The general idea is to estimate by fusing/combining attitude estimates $\boldsymbol{q}_{\boldsymbol{c}}^{\boldsymbol{w}}$ by integrating gyro measurements $\boldsymbol{q}^{\boldsymbol{c}}$ and direction obtained by the accelerometer measurements. In essence, the gyro estimates of attitude are used as accurate depictions in a small amount of time and faster movements, and the acceleration estimates of attitude are used as accurate directions to compensate for long-term gyro drift by integration.

The tri-axis gyroscope measures the angular rate $\boldsymbol{\omega}^{\boldsymbol{c}}$ in camera frame $\{c\}$. In one sampling period Δt, the updating orientation of the camera frame ${}^{\boldsymbol{\omega}}\boldsymbol{q}_{\boldsymbol{c}}^{\boldsymbol{w}}(t+\Delta t)$ can be solved by the first order Runge-Kutta method (RK1) with equation (3.17) and (3.18), where ${}^{\boldsymbol{est}}\hat{\boldsymbol{q}}_{\boldsymbol{c}}^{\boldsymbol{w}}(t)$ denotes the normalized previous estimation of orientation. This time update process gives accurate state prediction based on the integration of angular rates in a short time but drifts due to cumulative integration errors. Therefore, the measurement update process which could correct integration errors is necessary for a stable estimation in the long run.

$$^{\omega}\dot{\boldsymbol{q}}_{\boldsymbol{c}}^{\boldsymbol{w}}(t+\Delta t)=\frac{1}{2}{}^{\boldsymbol{est}}\hat{\boldsymbol{q}}_{\boldsymbol{c}}^{\boldsymbol{w}}(t)\otimes\begin{bmatrix}0\\ \boldsymbol{\omega^{c}}(t)\end{bmatrix} \tag{3.17}$$

$$^{\omega}\boldsymbol{q}_{\boldsymbol{c}}^{\boldsymbol{w}}(t+\Delta t)={}^{\boldsymbol{est}}\hat{\boldsymbol{q}}_{\boldsymbol{c}}^{\boldsymbol{w}}(t)+{}^{\omega}\dot{\boldsymbol{q}}_{\boldsymbol{c}}^{\boldsymbol{w}}(t+\Delta t)\Delta t \tag{3.18}$$

In the context of an orientation filter, it is assumed that the accelerometer will measure only gravity. Since gravity vector $\boldsymbol{g^{w}}$ is always known in the world frame $\{w\}$, the orientation of the camera frame $\{c\}$ respective to the world frame can be calculated from the accelerometer measurement of the gravity. The attitude estimation is done by using a gradient descent algorithm to solve a minimization problem expressed with equation (3.19) and (3.20), where $\hat{\boldsymbol{q}}_{\boldsymbol{c}}^{\boldsymbol{w}*}$ is the conjugate of $\hat{\boldsymbol{q}}_{\boldsymbol{c}}^{\boldsymbol{w}}$. $\hat{\boldsymbol{g}}^{\boldsymbol{w}}=\begin{bmatrix}0 & 0 & 0 & 1\end{bmatrix}^{T}$ denotes the normalized gravity vector and $\hat{\boldsymbol{a}}^{\boldsymbol{c}}=\begin{bmatrix}0 & a_x^c & a_y^c & a_z^c\end{bmatrix}^{T}$ is the normalized accelerometer measurements.

$$\min_{\hat{\boldsymbol{q}}_{\boldsymbol{c}}^{\boldsymbol{w}}\in\mathbb{R}^{4\times 1}}\boldsymbol{f}\left(\hat{\boldsymbol{q}}_{\boldsymbol{c}}^{\boldsymbol{w}},\hat{\boldsymbol{g}}^{\boldsymbol{w}},\hat{\boldsymbol{a}}^{\boldsymbol{c}}\right) \tag{3.19}$$

$$\boldsymbol{f}\left(\hat{\boldsymbol{q}}_{\boldsymbol{c}}^{\boldsymbol{w}},\hat{\boldsymbol{g}}^{\boldsymbol{w}},\hat{\boldsymbol{a}}^{\boldsymbol{c}}\right)=\hat{\boldsymbol{q}}_{\boldsymbol{c}}^{\boldsymbol{w}*}\otimes\hat{\boldsymbol{g}}^{\boldsymbol{w}}\otimes\hat{\boldsymbol{q}}_{\boldsymbol{c}}^{\boldsymbol{w}}-\hat{\boldsymbol{a}}^{\boldsymbol{c}} \tag{3.20}$$

Following the gradient descent algorithm, equation (3.21) calculates the updating orientation ${}^{\nabla}\boldsymbol{q}_{\boldsymbol{c}}^{\boldsymbol{w}}(t+\Delta t)$ based on the previous estimate of orientation ${}^{\boldsymbol{est}}\hat{\boldsymbol{q}}_{\boldsymbol{c}}^{\boldsymbol{w}}(t)$ at time t and the gradient of cost function $\nabla\boldsymbol{f}$ calculated in equation (3.22). $\boldsymbol{J}^{T}\left(\hat{\boldsymbol{q}}_{\boldsymbol{c}}^{\boldsymbol{w}},\hat{\boldsymbol{g}}^{\boldsymbol{w}}\right)$ is the Jacobian of the cost function. μ_t defines the step-size and affects the convergence rate. The calculation can be simplified by expressing the cost function and its Jacobian with equation (3.23) and (3.24).

$${}^{\nabla}\boldsymbol{q}_{\boldsymbol{c}}^{\boldsymbol{w}}(t+\Delta t)={}^{\boldsymbol{est}}\hat{\boldsymbol{q}}_{\boldsymbol{c}}^{\boldsymbol{w}}(t)-\mu_t\frac{\nabla\boldsymbol{f}}{\|\nabla\boldsymbol{f}\|} \tag{3.21}$$

$$\nabla \boldsymbol{f}\left({}^{\boldsymbol{est}}\hat{\boldsymbol{q}}_{\boldsymbol{c}}^{\boldsymbol{w}}(t), \hat{\boldsymbol{g}}^{\boldsymbol{w}}, \hat{\boldsymbol{a}}^{\boldsymbol{c}}(t+\Delta t)\right) = \boldsymbol{J}^{T}\left({}^{\boldsymbol{est}}\hat{\boldsymbol{q}}_{\boldsymbol{c}}^{\boldsymbol{w}}(t), \hat{\boldsymbol{g}}^{\boldsymbol{w}}\right) \boldsymbol{f}\left({}^{\boldsymbol{est}}\hat{\boldsymbol{q}}_{\boldsymbol{c}}^{\boldsymbol{w}}(t), \hat{\boldsymbol{g}}^{\boldsymbol{w}}, \hat{\boldsymbol{a}}^{\boldsymbol{c}}(t+\Delta t)\right) \tag{3.22}$$

$$\boldsymbol{f}\left({}^{\boldsymbol{est}}\hat{\boldsymbol{q}}_{\boldsymbol{c}}^{\boldsymbol{w}}(t), \hat{\boldsymbol{g}}^{\boldsymbol{w}}, \hat{\boldsymbol{a}}^{\boldsymbol{c}}(t+\Delta t)\right) = \begin{bmatrix} 2\left(q_1 q_3 - q_0 q_3\right) - a_x \\ 2\left(q_0 q_1 + q_2 q_3\right) - a_y \\ 2\left(\frac{1}{2} - q_1^2 - q_2^2\right) - a_z \end{bmatrix} \tag{3.23}$$

$$\boldsymbol{J}\left({}^{\boldsymbol{est}}\hat{\boldsymbol{q}}_{\boldsymbol{c}}^{\boldsymbol{w}}(t), \hat{\boldsymbol{g}}^{\boldsymbol{w}}\right) = \begin{bmatrix} -2q_2 & 2q_3 & -2q_0 & 2q_1 \\ 2q_1 & 2q_0 & 2q_3 & 2q_2 \\ 0 & -4q_1 & -4q_2 & 0 \end{bmatrix} \tag{3.24}$$

The last step is the fusion algorithm to calculate the estimation of the orientation of the camera frame relative to the world frame, ${}^{\boldsymbol{est}}\boldsymbol{q}_{\boldsymbol{c}}^{\boldsymbol{w}}(t+\Delta t)$, using ${}^{\boldsymbol{\omega}}\boldsymbol{q}_{\boldsymbol{c}}^{\boldsymbol{w}}(t+\Delta t)$ and ${}^{\boldsymbol{\nabla}}\boldsymbol{q}_{\boldsymbol{c}}^{\boldsymbol{w}}(t+\Delta t)$, obtained by equation (3.18) and (3.21). Eqaution (3.25) describes the fusion process, where ${}^{\boldsymbol{est}}\boldsymbol{q}_{\boldsymbol{c}}^{\boldsymbol{w}}$ is updated by numerically integrating the estimation of orirentation rate ${}^{\boldsymbol{est}}\dot{\boldsymbol{q}}_{\boldsymbol{c}}^{\boldsymbol{w}}$. In equation (3.26), ${}^{\boldsymbol{est}}\dot{\boldsymbol{q}}_{\boldsymbol{c}}^{\boldsymbol{w}}$ is calculated using the orientation rate provided by gyroscope, ${}^{\boldsymbol{\omega}}\dot{\boldsymbol{q}}_{\boldsymbol{c}}^{\boldsymbol{w}}$, to subtract the estimation error solved by accelerometer measurement. β is the filter gain that determines the trade-off between estimation results calculated by the gyroscope and accelerometer. The roll and pitch angles can be solved from equation 3.10, while the calculation of the yaw angle accompanying the position will be discussed in the next section.

$${}^{\boldsymbol{est}}\boldsymbol{q}_{\boldsymbol{c}}^{\boldsymbol{w}}(t+\Delta t) = {}^{\boldsymbol{est}}\hat{\boldsymbol{q}}_{\boldsymbol{c}}^{\boldsymbol{w}}(t) + {}^{\boldsymbol{est}}\dot{\boldsymbol{q}}_{\boldsymbol{c}}^{\boldsymbol{w}}(t+\Delta t)\Delta t \tag{3.25}$$

$${}^{\boldsymbol{est}}\dot{\boldsymbol{q}}_{\boldsymbol{c}}^{\boldsymbol{w}}(t+\Delta t) = {}^{\boldsymbol{\omega}}\dot{\boldsymbol{q}}_{\boldsymbol{c}}^{\boldsymbol{w}}(t+\Delta t) - \beta\frac{\nabla \boldsymbol{f}}{\|\nabla \boldsymbol{f}\|} \tag{3.26}$$

3.4.2 Inverse Mapping Based-on Newton-Raphson

The position and yaw angle of the camera is solved according to the inverse magnetic relationship. Due to the nonlinear nature of the magnetic field equation, it would be complicated to calculate the inverse solution directly. Inspired by the application of the iteration method for finding roots of inverse kinematics of the manipulator, an iteration algorithm is proposed based on the Newton-Raphson method for solving the inverse model. According to section 3.3.2, the forward model equation can be expressed by:

$$\boldsymbol{b^m} = f(\boldsymbol{p_a}, \boldsymbol{\Omega_a}, \boldsymbol{p_c}, \boldsymbol{\Omega_c}),\ f : \mathbb{R}^{12} \longrightarrow \mathbb{R}^3 \tag{3.27}$$

where the pose of the actuator, $\boldsymbol{p_a}$ and $\boldsymbol{\Omega_a}$, is known from the kinematics of the manipulator. $\boldsymbol{p_c} = \begin{bmatrix} x_c & y_c & z_c \end{bmatrix}^T$ and $\boldsymbol{\Omega_c} = (\phi_c, \theta_c, \psi_c)$ represent the position and orientation of the camera. The roll and pitch angle ϕ_c and θ_c are solved by the Madgwick filter in section 3.4.1. We use $\boldsymbol{\sigma_c} = (x_c, y_c, z_c, \psi_c)$ to represent the unknown parameters and the forward mapping can be simplified as

$$\boldsymbol{b^m} = f(\boldsymbol{\sigma_c}),\ f : \mathbb{R}^4 \longrightarrow \mathbb{R}^3 \tag{3.28}$$

The magnetic field $\boldsymbol{b^m}$ at $\{m\}$ is obtained from the MAG. Let $\boldsymbol{b^m} = \begin{bmatrix} b_x & b_y & b_z \end{bmatrix}^T$ be the desired MAG measurement. The function for the Newton-Raphson method is defined as $g(\boldsymbol{\sigma_c}) = \boldsymbol{b^m} - f(\boldsymbol{\sigma_c})$, and the goal is to find the solution $\boldsymbol{\sigma_c}$ such that $g(\boldsymbol{\sigma_c}) = 0$.

In the first localization, an initial guess value $\boldsymbol{\sigma_{c0}}$ that is sufficiently close to the desired solution $\boldsymbol{\sigma_c}$ is picked manually according to the actuator pose. The final result of each localization is used to initialize the future localization. Write the function as a Taylor expansion with first-order linearization as

Algorithm 1 Pseudocode for calculating unknown pose parameters $\boldsymbol{\sigma_c}$ of the camera given the actuator pose $\boldsymbol{p_a}$, $\boldsymbol{\Omega_a}$, orientation angle (ϕ_c, θ_c) of camera calculated from Madgwick filter and MAG data $\boldsymbol{b^m}$.

Input: $\boldsymbol{p_a}$, $\boldsymbol{\Omega_a}$, (ϕ_c, θ_c), $\boldsymbol{b^m}$

1: Initialization: Given $\boldsymbol{b^m} \in \mathbb{R}^3$ and an initial guess $\boldsymbol{\sigma_{c_0}} \in \mathbb{R}^4$, $i = 0$.
2: **repeat**
3: Calculate error $\boldsymbol{e} = \boldsymbol{b^m} - f(\boldsymbol{\sigma_{c_i}})$
4: Update $\boldsymbol{\sigma_{c_{i+1}}}$ with $\boldsymbol{\sigma_{c_{i+1}}} = \boldsymbol{\sigma_{c_i}} + \boldsymbol{J}^{\dagger}(\boldsymbol{\sigma_{c_i}})\boldsymbol{e}$
5: $i \leftarrow i + 1$
6: **until** $\|\boldsymbol{e}\| < \varepsilon$ or $i > iteration_{max}$
7: **if** $\|\boldsymbol{e}\| < \varepsilon$ **then**
8: Update $\boldsymbol{\sigma_c} = \boldsymbol{\sigma_{c_i}}$
9: **end if**

Output: Position $\boldsymbol{p_c}$ and yaw angle ψ_c of the camera.

$$\boldsymbol{b^m} = f(\boldsymbol{\sigma_c}) \approx f(\boldsymbol{\sigma_{c_0}}) + \underbrace{\left.\frac{\partial f}{\partial \boldsymbol{\sigma}}\right|_{\boldsymbol{\sigma_{c_0}}}}_{\boldsymbol{J}(\boldsymbol{\sigma_{c_0}})} \underbrace{(\boldsymbol{\sigma_c} - \boldsymbol{\sigma_{c_0}})}_{\Delta\boldsymbol{\sigma}} \tag{3.29}$$

where $\boldsymbol{J}(\boldsymbol{\sigma_{c_0}}) \in \mathbb{R}^{3\times4}$ describes the gradient of f with respect to $\boldsymbol{\sigma_c}$ evaluated at $\boldsymbol{\sigma_{c_0}}$. Since $\boldsymbol{J}$ is not invertible, we can solve for $\Delta\boldsymbol{\sigma}$ with Moore-Penrose pseudoinverse $\boldsymbol{J}^{\dagger}$,

$$\Delta\boldsymbol{\sigma} = \boldsymbol{J}^{\dagger}(\boldsymbol{\sigma_{c_0}})\left(\boldsymbol{b^m} - f(\boldsymbol{\sigma_{c_0}})\right) \tag{3.30}$$

Then the new guess is updated as $\boldsymbol{\sigma_{c_1}} = \boldsymbol{\sigma_{c_0}} + \Delta\boldsymbol{\sigma}$. During the proposed operation, the camera follows the actuator closely due to the powerful magnetic attraction. The updated guess keeps being close to the solution. Repeating the process, the solution will converge to $\boldsymbol{\sigma_c}$. Results exceeding the maximum number of iterations are discarded. The pseudocode to implement the iteration method is given as Algorithm 1.

3.5 EXPERIMENT AND RESULT

3.5.1 Platform Overview

The intra-abdominal wireless laparoscope system is shown in Fig. 3.5, including the actuator module, the wireless camera prototype, and a 6-DOF Universal Robots URe5. Fig. 3.5a and 3.5b demonstrate the camera module. The board is built around a Texas Instruments cc2541 wireless microcontroller unit, providing wireless communication and the interface for managing onboard resources. The MAG (ALS31313) has the range of $\pm 100mT$ and the resolution of $0.05mT$ in each direction. The design of the actuator is illustrated in Fig. 3.5c and 3.5d, which contains two diametrically magnetized PMs and a micromotor connecting with a driver board.

A PC connects to all the hardware through various communication interfaces. The robot is connected through real-time TCP/IP communication. The driver board controlling the micromotor inside the actuator is controlled through RS-232. Digital sensor data collected by the camera such as IMU and MAG data is transmitted by Bluetooth connection. Controlled by the manipulator, the camera locomotes dexterously on an abdominal tissue simulator attached to an Acrylic board. A stereo camera (MYNT EYE S1030) measures the position and yaw angle of the camera. During the translation along x_c, the tube housing of the camera scrolls smoothly instead of sliding with hysteresis, making the camera follow the actuator closely. Besides, the camera can also rotate around z_c repeatedly within $\pm 180°$. The tilt motion is able to reach $\pm 90°$ with a fast response due to the two bearings inside the camera.

3.5.2 Magnetic Relationship Evaluation

The proposed localization method relies on the magnetic relationship described in Section 3.3.2. The setup shown in Fig. 3.6 is used to evaluate the error of the forward mapping from the camera pose to MAG measurement. First, the bias reading of the

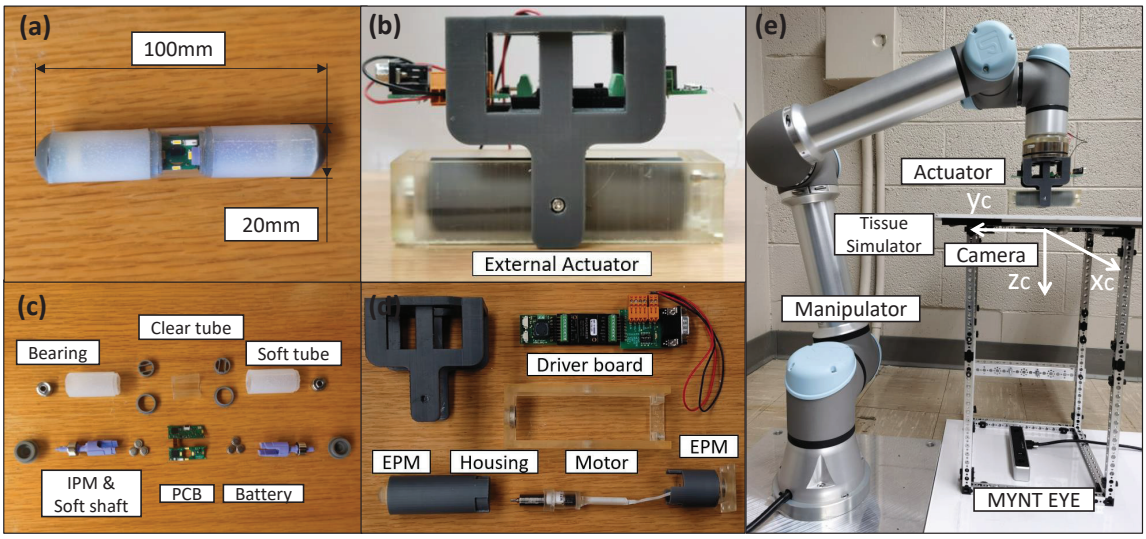

Figure 3.5: Overview of the system. (a) and (b) display the assembled camera module and the external actuator. (c) and (d) show the details of each module including the camera board built around a Bluetooth chip, the location of two pairs of magnets, and the micromotor controlling the tilt motion. (e) introduces the layout of the system for testing locomotion ability.

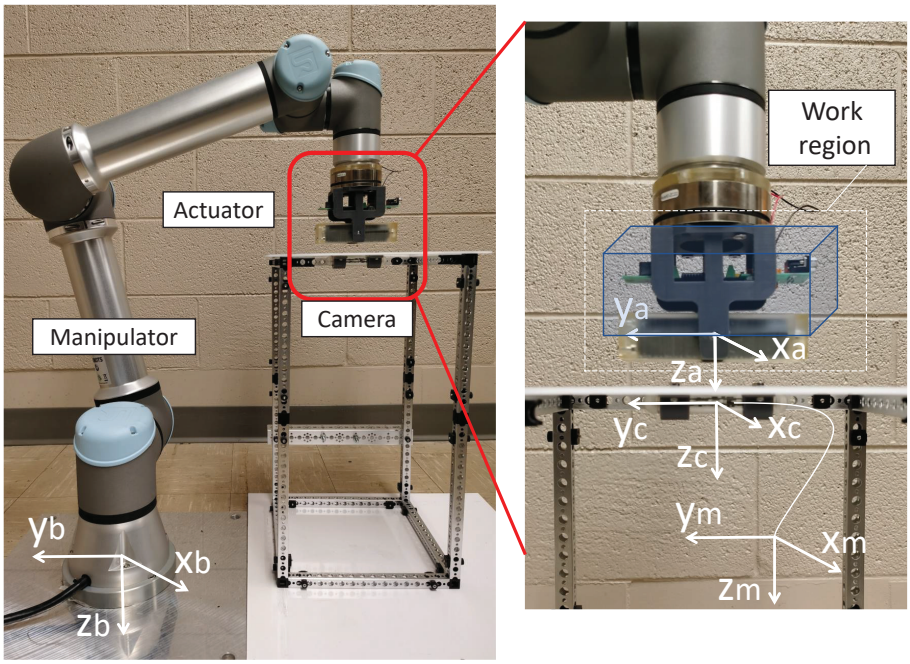

Figure 3.6: Experiment platform for evaluating localization method. The camera is fixed and calibrated at a known pose. Steering the actuator to move in the blue work region, MAG measurements are collected for evaluating the forward mapping model and the localization error.

MAG due to the IPMs is measured, which is $(0.20mT, 0.35mT, -1.20mT)$. The MAG data used in the following experiments is subtracted by the bias reading.

The actuator module is attached to the tool flange of the manipulator and the actuator pose is known from the forward kinematics of the manipulator and the dimension of the actuator design. The core idea of the evaluation is to record the relative pose between the MAG center frame $\{m\}$ and the actuator center frame $\{a\}$ and substitute it with the forward mapping model to calculate the desired MAG measurement B_d. Then compare $\boldsymbol{B_d}$ with the ground truth measured from the MAG. The camera is mounted onto an Arcylic board supported by an aluminum structure. The pose of MAG frame $\{m\}$ is fixed and known by calibration, where the position is $\boldsymbol{p_m^w}$ and the orientation aligns with base frame $\{b\}$. A $50mm \times 50mm \times 20mm$ cuboid region is allocated above the camera, which is separated into 21 layers parallel to $x_m y_m - plane$ along z_m uniformly. Steering the actuator to move along the preset scanning paths on each layer, the MAG measurements $\boldsymbol{b^m} = \begin{bmatrix} b_x & b_y & b_z \end{bmatrix}^T$ are transmitted to the PC through Bluetooth. During the scanning, the orientation of actuator frame $\{a\}$ keeps aligned with the MAG frame $\{m\}$.

Table 3.2 concludes the distribution of the relative error of the magnetic field from the forward mapping model. The estimation based on the proposed forward mapping model shows relative errors less than 5% for 79.1% of the testing region and a relative error below 10% for 97% of the region. Fig. 3.7 shows several relative error maps for magnetic field estimation in layers $D = 35mm$, $D = 40mm$, $D = 45mm$ and $D = 50mm$. In each layer, larger relative errors occurred at the edges or the corners of the test region. This might be caused by the inaccuracy of the single-dipole model for cylinder magnets which are not spherical magnets. The error tends to drop when the actuator approaches the MAG, and the cold color areas occupy over 90% of the region where x and y start from -10 to $10mm$. The estimation based on our forward mapping model shows an effective precision. As a result, better performance can be achieved when the camera keeps following the actuator closely.

Table 3.2: Distribution of the Relative Error from the Forward Mapping Model

Relative error	Portions
2% or less	36.2%
5% or less	79.1%
10% or less	97.0%
15% or less	99.6%

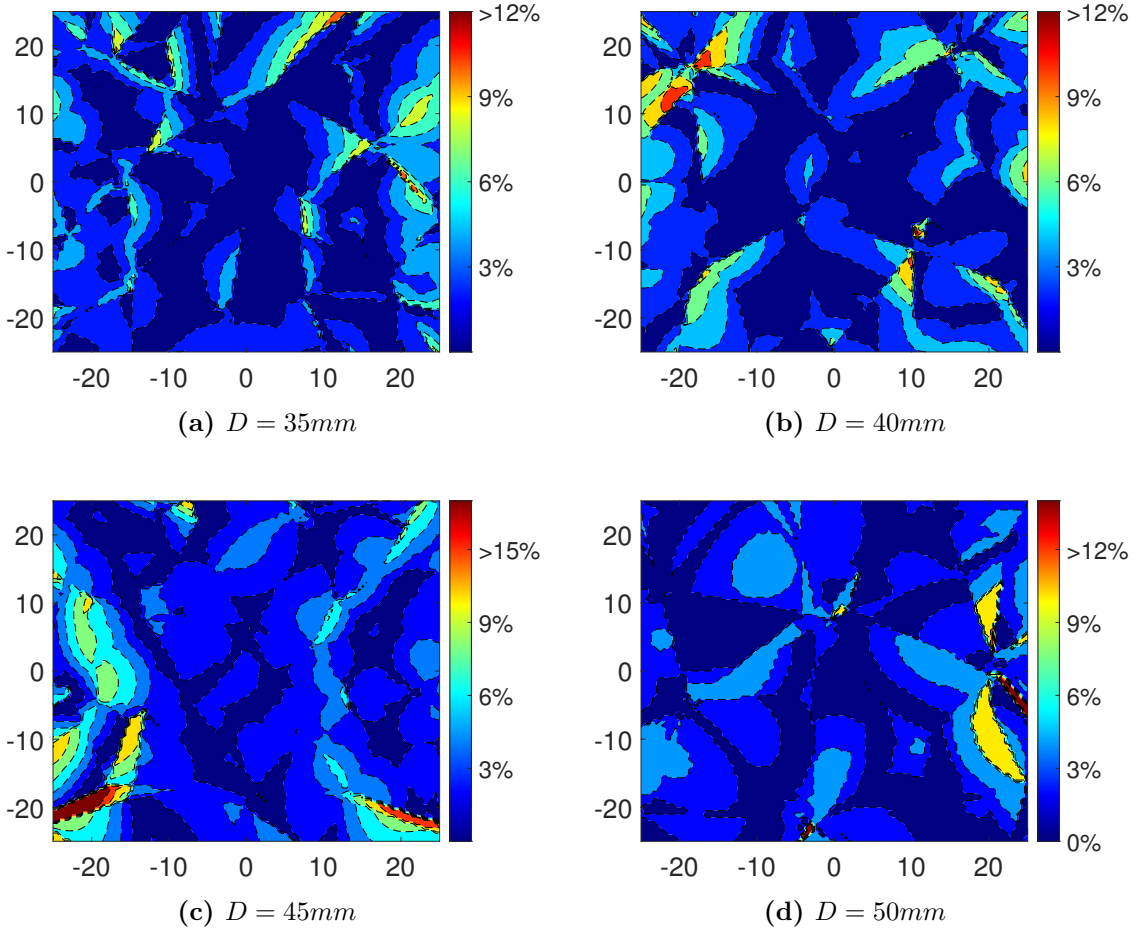

(a) $D = 35mm$ **(b)** $D = 40mm$

(c) $D = 45mm$ **(d)** $D = 50mm$

Figure 3.7: Relative error map in layers based on different actuator-camera normal distance D. x and y axis represent the relative position between $\{m\}$ and $\{a\}$ with respect to $\{m\}$.

3.5.3 Localization Algorithm Assessment

This section aims to assess the performance of the localization algorithm including the pose tracking error and drift. In the experiment, we use the same setup as Section 3.5.2, where the camera is fixed to a known position and the camera pose is calibrated to align with the base frame. Steering the actuator to move along a group of preset paths, the relative pose between the camera and the actuator is calculated with the MAG data and the algorithm. The error of the algorithm can be assessed by comparing the actuator pose and the result that combines the known camera pose and the solved relative pose.

Fifteen different trajectories are defined by the spacial Archimedean spiral function and constrained in a $15mm \times 15mm \times 15mm$ cubic space above the camera. All the trajectories start from the same point $\boldsymbol{p_s^c} = (0mm, 0mm, 35mm)$ and return the same way after reaching the endpoint. During the testing, z_a keeps being parallel to z_c, and y_a always coincides with the projection of the tangent of the trajectory on $x_c y_c - plane$. Every test takes about two minutes. The actuator pose is recorded as ground truth. The sample rate of MAG is set to be 100Hz, while the update frequency of the localization can reach to 30Hz in real-time. Fig. 3.8 reports the error for all the trajectory tests. Expressing all the error in frame $\{b\}$, the average error is $1.3mm$ for x, $1.4mm$ for y, $1.6mm$ for z and $5.2°$. 75% of the position errors on each axis stay below $2mm$. The average error of the position in space is $2.9mm$. Some extra large errors occurred but did not stop the algorithm due to the fast refresh rate. The whole testing process took about 40 minutes, during which the yaw angle error did not appear to drift.

Fig. 3.9 shows one of the trajectory testing results. The trajectory starts from $\boldsymbol{p_s^c}$ and reach to the point $\boldsymbol{p_e^c} = (12.57mm, 0mm, 50mm)$. In Fig. 3.9a, the red solid line is the ground truth of the actuator position and the green points are the estimated positions of the actuator which stay close to the true values. Fig. 3.9b shows the results projected onto the $x_c y_c - plane$. The red arrows represent the ground truth

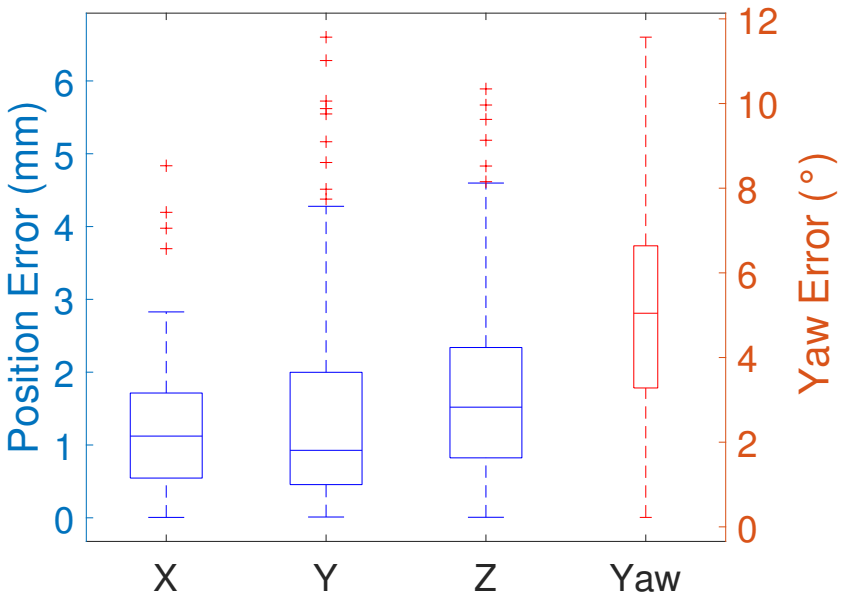

Figure 3.8: Error bar plot for the proposed localization method. Position errors on each axis and the yaw angle error are expressed in $\{b\}$. The whiskers represent the maximum and minimum errors, while the bars in the boxes account for average error.

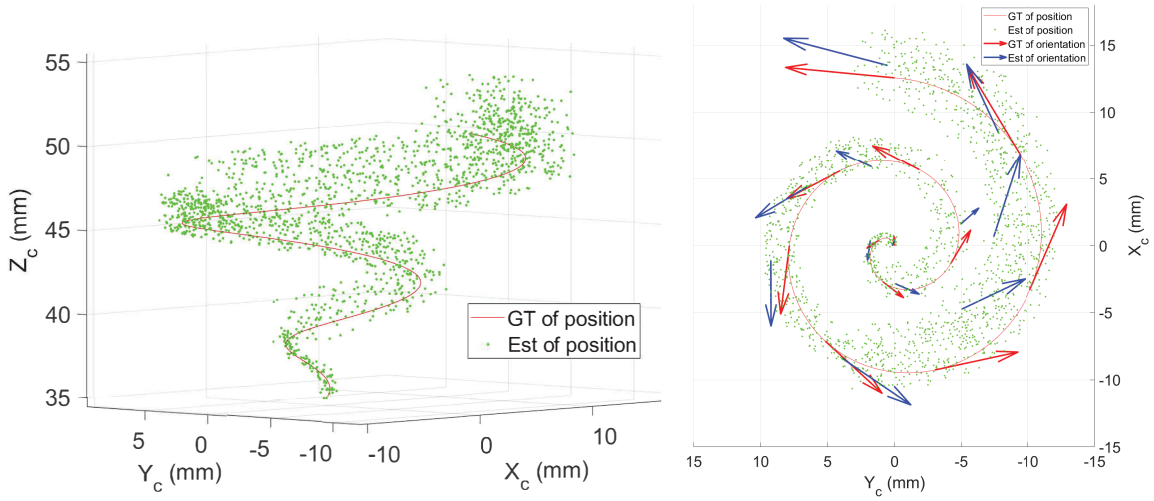

(a) Trajectory tracking in 3D space

(b) Top view of the trajectory tracking

Figure 3.9: Trajectory tracking of the actuator for evaluating the localization method. 3500 points are recorded for each test. The green points represent the estimated position. The red line shows the ground truth of the trajectory. The red arrows are the ground truth of the directions of y_a, while the blue arrows are the estimated results for the directions of y_a.

of the direction and magnitude of y_a. The blue arrows represent the estimated error of y_a. The angle between the arrows shows the yaw angle error. The average absolute error of the position is $2.5mm$. The average absolute error of the yaw is about $4.7°$. The algorithm typically converges faster in the middle region where the position errors are smaller. Larger errors occur on the edges of the space, which is consistent with the distribution of the forward mapping error.

3.6 CONCLUSIONS and FUTURE WORK

This paper describes a real-time localization method for an intra-abdominal wireless magnetic laparoscope. The two pairs of magnets aim to provide sufficient coupling force and relieve the inaccuracy of the single dipole model due to the distance. A relative working region is selected and proofed to model the magnetic relationship accurately. Arranging the magnet poles anti-parallel, unique magnetic field vectors exist for every position point in the workspace. The algorithm based on Newton-Raphson iteration and multiple sensor fusion is proposed to solve the inverse magnetic mapping and realize a 6-DOF localization of the camera. The yaw angle is solved directly without suffering from drift due to the estimation based on IMU. The proposed approach can provide an average error within $2.9mm$ in position detection and $5.5°$ for angular measurement. The refresh rate can reach to 30Hz. Currently, the method requires calibration to initiate the localization. Future work will focus on improving the robustness of the localization to initialization and upgrading the refresh frequency for real-time closed-loop control.

Chapter 4

Robotic-Assisted Control of the Wireless Magnetic Laparoscopic System

4.1 Introduction

In conventional laparoscopic surgery (LS) or minimally invasive surgery (MIS), a rigid long-stick laparoscope is inserted through a trocar and operated within a confined conical space. The laparoscope's movement is restricted, and its manual control is often counterintuitive. A highly skilled and extensively trained laparoscopist is necessary to maintain and adjust the laparoscope's position and angle throughout the procedure. This not only leads to a crowded operating table but also compromises the precision of the camera's view due to the inherent limitations of manual controls.

Robotic-assisted driving has been proven to enhance precision and control, making it indispensable for both diagnostics and therapeutics [79]. These robotic systems map complex instrument movements to an intuitive surgeon interface, allowing surgeons to concentrate on surgical tasks with improved efficiency. Some advanced robotic MIS surgical systems, such as the Da Vinci Single-Site, Da Vinci Sp [80], and Flex

Robotic System [81], address the issue of port crowding and enhance triangulation by providing additional degrees of freedom (DOFs) at the end-effectors through cable-driven mechanisms. However, the field of view (FOV) of the laparoscope is still restricted due to the limited workspace. Chapter 2 and chapter 3 introduce the structure design and pose estimation method for a robotic-assisted laparoscopic Magnetic Anchoring and Guidance System (MAGS). The external magnetic actuator is mounted on a collaborative robot with multiple DOFs, serving as the end effector, while the wireless camera module is fully inserted into the patient's abdomen and manipulated by the actuator.

Most of the current designs in this field employ open-loop control [13][12][23][19]. As a result, these approaches exhibit mediocre locomotion precision and limited robustness in the face of environmental uncertainties. Any disruptions in the path of the device, such as an uneven abdominal wall, can impede its motion and require the user to reposition the actuating magnet to reestablish magnetic coupling with the camera, which makes the procedure unsafe and time-consuming. To ensure the feasibility of the robotic-assisted system for clinical applications, closed-loop control is essential. In this control scheme, the user can intuitively specify desired camera motions through a proper user interface. The magnetic coupling is adaptively adjusted to ensure friendly tissue contact and robustness against environmental uncertainties. This approach allows for precise and controlled movements of the camera, enhancing the overall safety and effectiveness of the system during surgical procedures.

Recently, several groups have investigated close loop control for their MAGSs [43][18]. Li and Cheng proposed a visual servo control method for two different MAGS endoscopes [33][65], allowing automatic instrument tracking through marker attachments. However, without knowledge of the camera pose, it relies on weak assumptions and simplified kinematic models, where it is assumed that the magnets are always aligned, and the dynamics of tissue contact are disregarded. Salerno implements a preliminary 2-DOF localization obtaining the planar position feedback to a closed loop control of a magnetic-driven capsule endoscope for GI tract [82]. This research mainly discusses

magnetic force control instead of camera pose tracking. In Mahoney's study [67], a wireless MAGS endoscope prototype was utilized to demonstrate 3-DOF closed-loop position control and 2-DOF open-loop orientation control in a fluid-distended environment. The validation of the trajectory tracking is performed in a water-filled tank and the real-time position localization counts on an external camera. The 2-DOF orientation tracking is based on the assumption that the capsule is operated at low speed and acceleration without disturbances and that the magnet pairs keep aligned. Thus, it is challenging to transfer the method to clinical scenarios. In Taddese's study [68], the approach of closed-loop control was expanded to a tethered magnetic endoscope, enabling control of 2 degrees of freedom (2-DOF) position and 2 degrees of freedom (2-DOF) orientation in more general scenarios. The endoscope capsule remains pressed against a tissue barrier while being attracted by the external actuator. A real-time 6-DOF magnetic localization algorithm was integrated to enable trajectory following. The forces applied by the cable and tissue were considered disturbances that affect the alignment of the capsule with the desired heading directions. To improve the robustness of the camera manipulation in the hostile colon environment, a simplified dynamic model of the tethered capsule [69] was established using Euler-Lagrange equations, taking into account the interactions between the tissue and the device. This model served as the basis for an explicit model predictive control approach, which allowed the camera to adapt to the planned trajectory even when encountering folds in the tissue. It is important to note that the tissue-camera contact model in this study only considered sliding friction with manually tuned coefficients, while other contact forces such as membrane tension, shear force, and pressure force were not described in detail.

In this Chapter, a close loop control approach is proposed and applied for the pose tracking of the RAS wireless laparoscopic system. This control method aims to allow surgeons to navigate the wireless camera to provide the desired views through intuitive commands. A proper tissue-camera contact model related to the wheeled design and rolling friction elaborated in Chapter 2 is adopted and analyzed to guarantee stable

magnetic coupling and safe tissue interaction. The rest of this chapter is organized as follows. Section 4.2 introduces the tissue-camera contact model and the equation of camera motion based on the viscoelastic biological tissue model. A closed loop controller for camera pose tracking is described in Section 4.3. The experiment and validation are performed in Section 4.4. Finally, Section 4.5 concludes this Chapter.

4.2 Tissue-Camera Interaction Model

The proposed wireless camera has three decoupled DOFs including panning around the z_c axis, tilting around y_c, and translating along x_c. When the camera is in pan motion, there is mainly sliding motion between the camera and the tissue. As for the tilting and translating, the camera follows a rolling motion along the abdominal wall, which can be viewed in the general context of wheel-surface interaction on a deformable surface. For many years, researchers developed a mount of theories and analytical models to investigate the surface properties, shear stress, and wheel slip during wheel-soil interaction [83][84][85]. However, the wheel-tissue interaction can be quite different from those of soils due to the highly deformable and slick properties and the strong tissue membrane tensile force. Accordingly, a mathematical model was proposed by [86] to analyze the interaction between a wheeled mobile robot and liver tissue, where the organ tissue is considered a viscoelastic model. Furtherly, Yazdanpanah, and Li presented a generalized biomechanical model and tissue behavior of the abdominal wall by using four Kelvin-Voigt models in series to describe the tissue with multiple layers [87][46]. This section builds upon the theoretical formulations and property parameters and expanded their approaches to both sliding and rolling interactions that occurred in the proposed camera design.

4.2.1 Modeling of the Multi-layer Abdominal Wall Tissue

The behavior of living biological tissue usually displays viscoelastic, highly non-linear, inhomogeneous, and anisotropic properties [88]. The Kelvin-Voigt model is a common model to describe viscoelastic material under creep compression. As shown in Fig. 4.1, four serial Kelvin-Voigt models are used to simulate the creep behavior of the abdominal wall, which demonstrate the main layers of the tissue including skin, fat, muscle, and peritoneum connective tissues [89]. E_i and η_i represent the modulus of elasticity and viscosity of the i_{th} layer. Given a sudden constant stress σ_0, the displacement of the i_th layer ε_i will approach the deformation for the pure elastic material σ_0/E with the difference decaying exponentially shown in equation 4.1.

$$\varepsilon(t) = \frac{\sigma_0}{E_i}\left(1 - e^{-\frac{t}{\tau_i}}\right) \tag{4.1}$$

where t is time and $\tau_i = \eta_i/E_i$ is the retardation time. Then, the total displacement of the multi-layer tissue can be described by equation 4.2. The tissue property parameters were estimated by creep experiments which are proposed and detailed in [87].

$$\varepsilon(t) = \sigma_0 \sum_{i=1}^{4} \frac{1}{E_i}\left(1 - e^{-\frac{t}{\tau_i}}\right) \tag{4.2}$$

4.2.2 Contact and Interaction Model

The section view of the contact model is shown in Fig. 4.2. The tissue surface passively deforms along the camera's profile from the tail interaction point T to the head interaction point H. Beyond these two positions, the deflection profile of the membrane follows a decaying exponential function in the x-direction. r is the radius of the camera's profile. $\dot{x}_c$ and $\dot{\theta}_c$ represent the wheel rotation velocity and camera translation velocity. The vertical camera position is y_c. I_t and I_h are the contact length along x, and ϕ_t and ϕ_h are the contact angles. T is the membrane tension which relates to the tissue deformation. When the camera is actuated by the

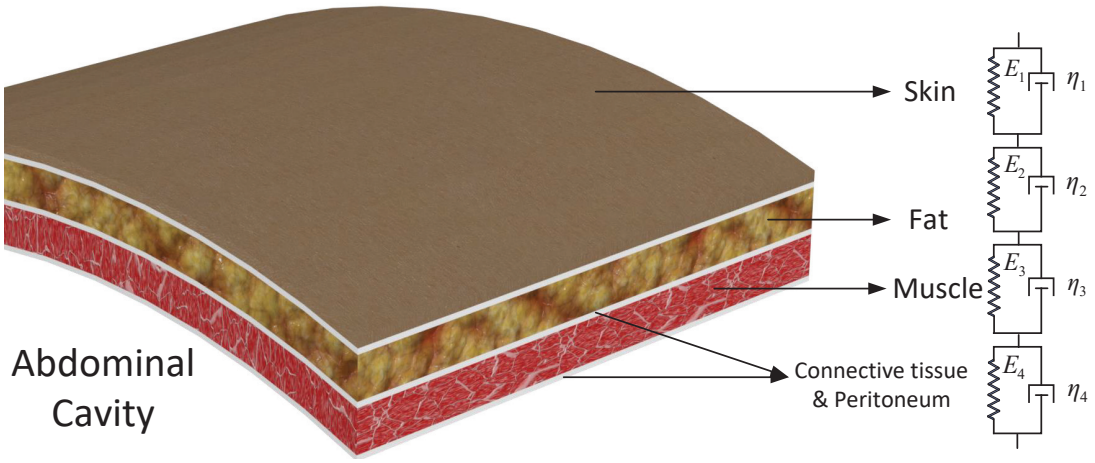

Figure 4.1: Mechanical modeling of multi-layer abdominal tissue with four serial Kelvin-Voigt models. From outside to inside, the four main layers are skin, fat, muscle, and peritoneum connective tissue.

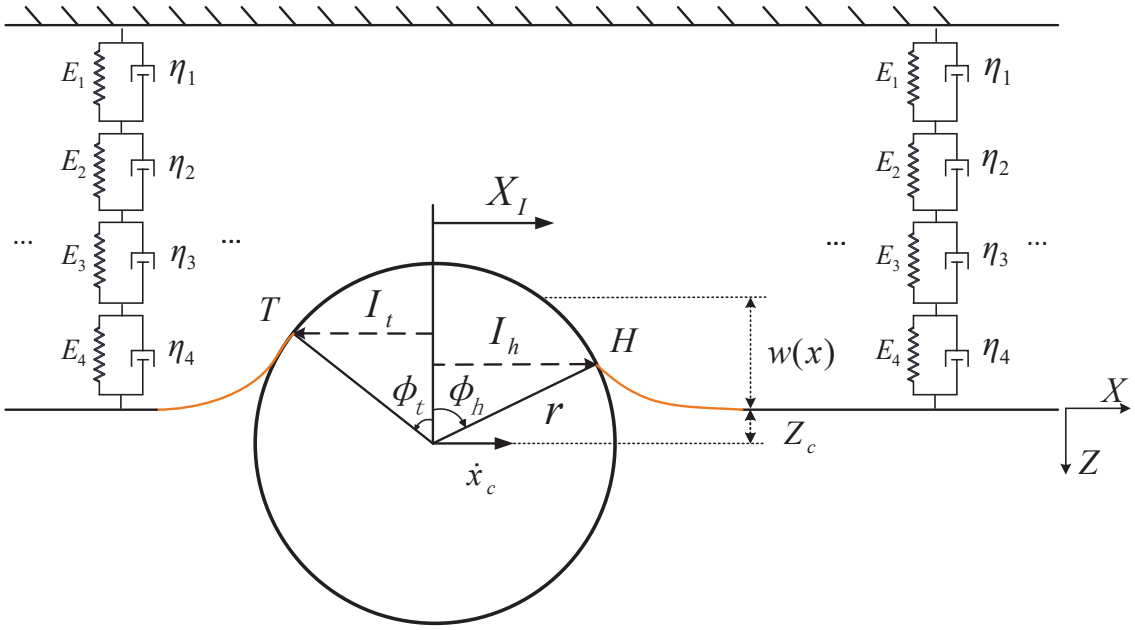

Figure 4.2: Sectional view of the tissue-camera contact model.

magnetic force, the length of contact behind the camera is less than in front of it due to the viscoelastic nature of the tissue. w defines the deformation of the tissue which can be expressed as the segmented function 4.3

$$w(x_c) = \begin{cases} Ae^{B(x-I_t)} & , x \in (-\infty, -I_t) \\ \sqrt{r^2 - x^2} - z_c & , x \in (-I_t, I_h] \\ Ce^{D(x-I_h)} & , x \in (I_h, +\infty] \end{cases} \tag{4.3}$$

where the constants A, B, C, and D are determined from the boundary conditions 4.4 at the contact points T and H.

$$\begin{cases} w(x = I_t) = rcos(\phi_t) - z_c \\ \frac{dw(x=I_t)}{dx} = -tan(\phi_t) \\ w(x = I_h) = rcos(\phi_h) - z_c \\ \frac{dw(x=I_h)}{dx_c} = -tan(\phi_h) \end{cases} \tag{4.4}$$

After solving A, B, C, and D, the tissue deflection can be updated as equation 4.5

$$w(x) = \begin{cases} (rcos(\phi_t) - z_c)e^{\frac{-tan(\phi_t)(x-I_t)}{rcos(\phi_t)-z_c}} & , x \in (-\infty, -I_t) \\ \sqrt{r^2 - x^2} - z_c & , x \in (-I_t, I_h] \\ (rcos(\phi_h) - z_c)e^{\frac{-tan(\phi_h)(x-I_h)}{rcos(\phi_h)-z_c}} & , x \in (I_h, +\infty] \end{cases} \tag{4.5}$$

The free body diagram of the camera with interaction with the tissue moving along x direction is shown in Fig. 4.3. mg represents the gravity of the camera. F_m denotes the magnetic force applied by the EMPs embedded in the external actuator, which is resolved to F_{mz} and F_{mx} along z and x direction. The reaction force generated from the tissue is F_r, which is also decomposed to two component forces F_{rz} and F_{rx}. The reaction force is supposed to be the combination of the tissue membrane tension F_t, stress F_s from the viscoelastic tissue model, and viscous force F_v of peritoneum

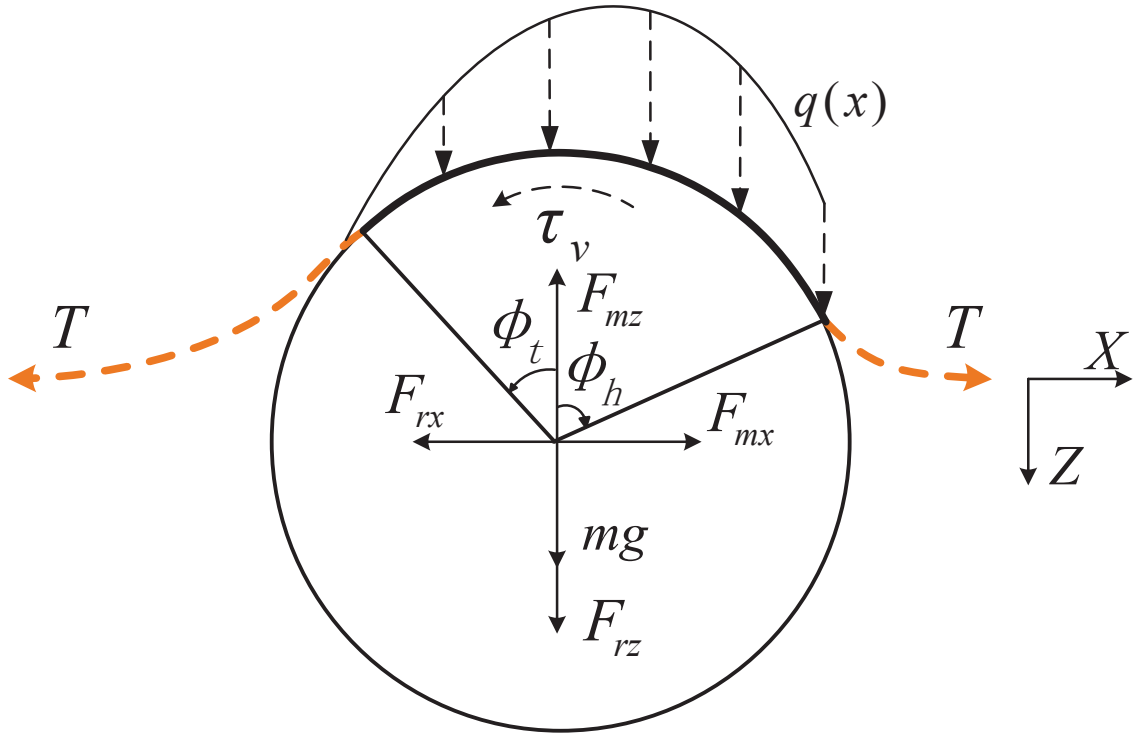

Figure 4.3: Free body diagram of the camera capsule in contact with the abdominal wall. The reaction force is supposed to be the combination of the tissue membrane tension F_t, stress F_s from the viscoelastic tissue model, and viscous force F_v of peritoneum fluid covering the tissue.

fluid covering the tissue. Therefore, the camera tissue interaction force is given by equation 4.6.

$$F_r = F_t + F_s + F_v \tag{4.6}$$

Finding equations of motion requires considering the forces acting on the camera capsule along each axis. Starting from the tissue membrane tension and stress force, the vertical force F_{t-z} and F_{s-z} can be solved by equation 4.7 and 4.8, where L is the length of the camera.

$$\begin{aligned} F_{t-z} &= T(sin(\phi_h) - sin(\phi_t)) \\ &= L(\int_{I_h}^{+\infty} q(x)\,dx - \int_{-\infty}^{I_t} q(x)\,dx) \\ &= L(\int_{I_h}^{+\infty} \frac{Ce^{D(x-I_h)}}{\sum_{i=1}^{4} \frac{1}{E_i}\left(1 - e^{-\frac{t}{\tau_i}}\right)}\,dx - \int_{-\infty}^{I_t} \frac{Ae^{B(x-I_h)}}{\sum_{i=1}^{4} \frac{1}{E_i}\left(1 - e^{-\frac{t}{\tau_i}}\right)}\,dx) \end{aligned} \tag{4.7}$$

$$F_{s-z} = L\int_{I_t}^{I_h} q(x)\,dx = L\int_{I_t}^{I_h} \frac{\sqrt{r^2 - x^2} - z_c}{\sum_{i=1}^{4} \frac{1}{E_i}\left(1 - e^{-\frac{t}{\tau_i}}\right)}\,dx \tag{4.8}$$

The horizontal stress from the tissue F_{s-x}, and the resultant force from the membrane tension F_{t-x}, is nonzero due to the asymmetry caused by the viscoelastic response. The effect of the tension in the membrane is in equation 4.9.

$$F_{t-x} = T(cos(\phi_h) - cos(\phi_t)) \tag{4.9}$$

Assuming the resultant tissue reaction force is radial to the wheel, the horizontal stress force can be estimated from equation 4.10.

$$F_{s-x} = -L\int_{\phi_t}^{\phi_h} \frac{q(\phi)}{cos\phi} r sin\phi\,d\phi = -Lr\int_{\phi_t}^{\phi_h} q(\phi) tan\phi\,d\phi \tag{4.10}$$

The shear force is generated from the viscous peritoneal fluid covering the tissue. Due to the asymmetry of contact lengths in front and backside, the shear stress generates a force on both x and z directions. Projecting the shear force along these axes the generated force can be estimated by equations 4.11 and 4.12.

$$F_{v-x} = L \int_{\phi_t}^{\phi_h} r\tau_v cos\phi \, dx \tag{4.11}$$

$$F_{v-z} = L \int_{\phi_t}^{\phi_h} r\tau_v sin\phi \, dx \tag{4.12}$$

τ_v is the shear stress at the contact surface and can be described by

$$\tau_v = \mu \frac{V_{\text{rel}}}{h} = \frac{-r\dot{\theta}_c - \dot{x}_c cos\phi}{h} \tag{4.13}$$

where V_{rel} is the relative velocity between the camera surface and the tissue, and h is the distance between the camera and tissue. μ is the viscosity of the fluid. $\dot{\theta}_c$ is the wheel rotational. $\dot{x}_c$ is the horizontal velocity of the camera center. The equations of motion can be written in equation 4.14.

$$\begin{cases} m\ddot{x}_c = F_{mx} + F_{s-x} + F_{t-x} + F_{v-x} \\ m\ddot{z}_c = F_{mz} + F_{s-z} + F_{t-z} + F_{v-z} + mg \end{cases} \tag{4.14}$$

4.3 Closed-loop Control

As shown in Fig. 4.4, the structure of robotic-assisted control is composed of the pose estimation described in chapter 3 adding a Kalman filter, camera-tissue contact model, controller for actuation, and an online optimization algorithm. The controller takes as input a desired camera position p_d and heading direction h_d, the estimated camera position $\overline{p}_c$ and orientation $\overline{h}_c$, and the estimated capsule spatial velocity $\dot{\overline{p}}_c$ and angular velocity $\dot{\overline{h}}_c$, and produces a desired change in total applied force δf_d and torque $\delta\tau_d$. The desired change in applied force δf_d and the desired change in torque

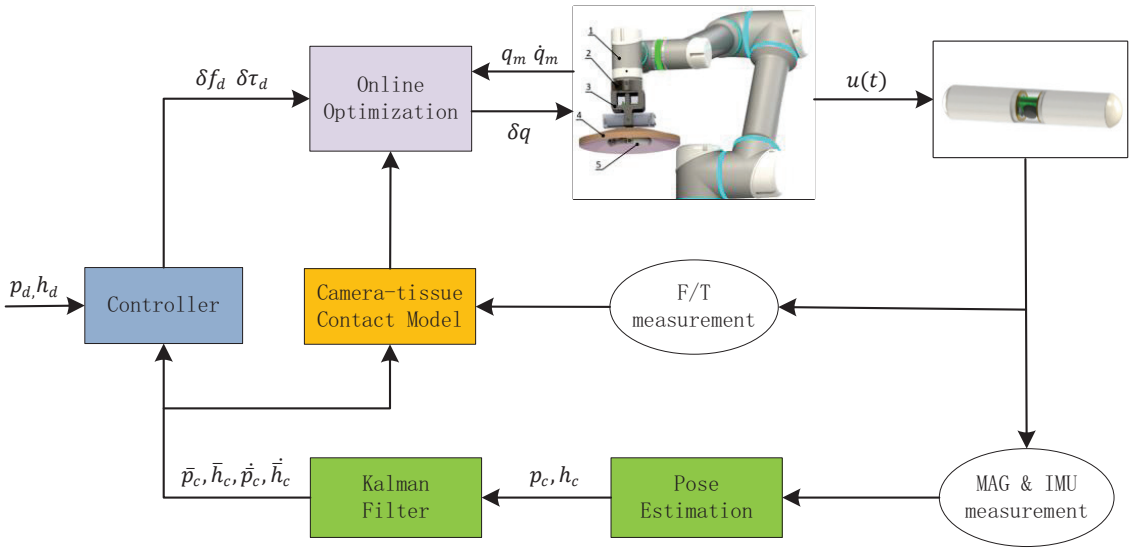

Figure 4.4: Structure of robotic-assisted control.

$\delta\tau_d$ are converted into a necessary change in robot manipulator joints δq by solving an optimization problem, where the interaction force between the camera and tissue is considered as constrain. The interaction force is acquired by the camera-tissue contact model presented by section 4.2.2. The refresh frequency is 30Hz.

4.4 Experiments and Result

A translation experiment was performed to evaluate the feasibility of the robotic-assisted control. The experiment platform is shown in Fig. 4.5. The actuator is mounted onto the tool head of the 7-DOF manipulator (KUKA GMBH, Germany) through a force-torque sensor (Axia80-M20, ATI). A piece of pork belly of around $35mm$ thickness is fixed on an aluminum frame. The internal camera was anchored onto the pork belly through magnetic coupling. Another camera is attached to the bottom of the platform to track the position of the camera capsule during the translation test.

After the initialization, the camera was supposed to follow a sin wave trajectory along the x_c. The desired stroke is $90mm$. Ten trials were conducted and two cycles of reciprocating motion were performed during each trial. The mean deviation along x_c was $4.6mm \pm 2.9mm$. One of the test results is shown in Fig. 4.6. The camera was able to follow the desired path with moderate error. Although a small deviation along the y direction was also detected, the total deviation was acceptable.

4.5 Summary and Conclusion

In this chapter, a method of robotic-assisted control for the proposed laparoscopic system is presented. The tissue-camera interaction is modeled to facilitate maintaining the reliable magnetic coupling, at the same time, avoiding excessive pressure on the tissue. Combined with the pose estimation described in Chapter 3, the structure of the robotic-assisted closed-loop control has been realized with a controller and

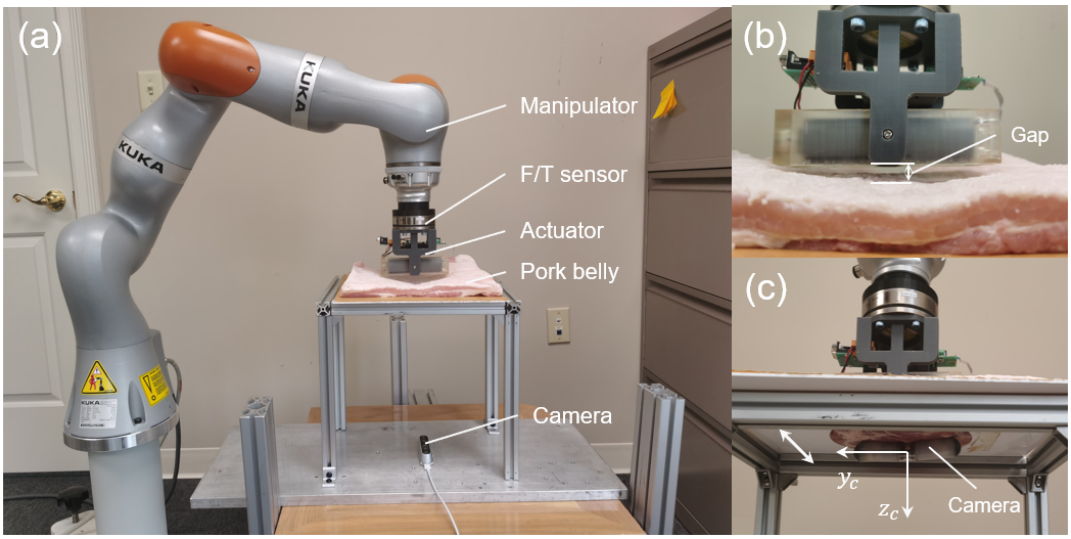

Figure 4.5: Experimental platform for robotic-assisted control.

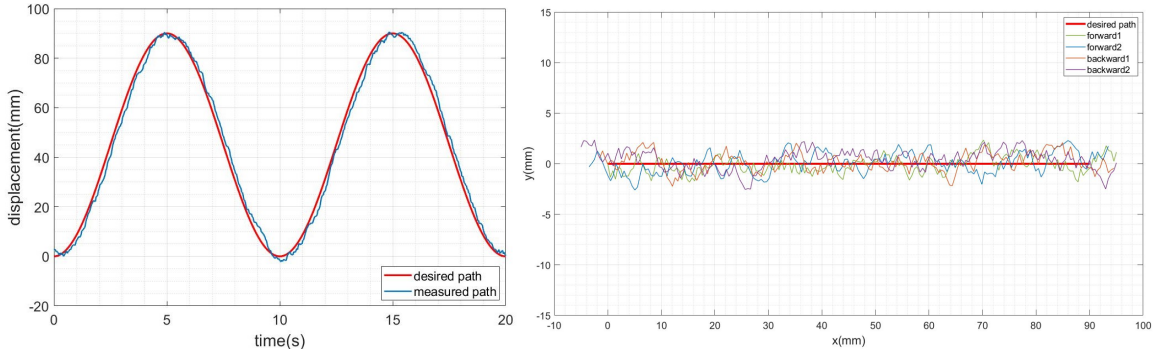

(a) Trajectory tracking in x direction. **(b)** Trajectory tracking in $x-y$ plane.

Figure 4.6: Trajectory tracking of the camera for evaluating the closed-loop control. 600 points are recorded for each test. In(a), the red line shows the desired trajectory. The blue line represents the measured result. In(b), The red line is the desired path in the $x-y$ plane. The measured trajectories are denoted in other colors including two forward paths and two backward paths.

online optimization algorithm. The feasibility has been shown with a translation trajectory tracking test. Although outcomes were promising, further work is necessary including further analysis of the tissue characterization and a better controller for robust improvement. Meanwhile, the current controller is designed for decoupled motion. The method for complex movements needs to be investigated further.

Chapter 5

Tetherless Vision and Control for Insertable Laparoscopic Cameras

5.1 Introduction

The MAGS provides a promising way for traditional laparoscopic surgery to reduce the trocar number and improve the FOV of the laparoscope, in which the internal laparoscope can be manipulated through magnetic coupling leaving the trocar free for instruments. However, most of the designs rely on tethering wires which are commonly used for video transmission, control communication, and power supply. As a result, these wires pose challenges such as operational restrictions, limited mobility of the camera, risk of gas leakage, and increased difficulties in sanitization. To overcome these limitations and enhance the clinical acceptance of insertable laparoscopic cameras, a tetherless design and implementation approach is crucial. This chapter focuses on establishing a tetherless architecture that combines practical electronic and software solutions to create a fully functional and clinically acceptable insertable laparoscopic camera system. The architecture ensures reliable wireless transmission, efficient control, and optimized power management. The integration

of these components provides surgeons with the flexibility and precision required for successful laparoscopic procedures.

The tetherless electronic solution addresses the need for wireless transmission of video and control signals, as well as the power supply for the insertable laparoscopic camera. The implementation is based on cutting-edge technologies to ensure reliable and efficient operation. By eliminating the reliance on tethering wires, the camera gains enhanced mobility and maneuverability within the surgical environment.

In addition to the electronic components, a robust software solution is essential for seamless communication and control of the insertable laparoscopic camera. The software is designed to support various functionalities, including video streaming, control commands, and feedback mechanisms. The implementation of a user-friendly interface allows surgeons to intuitively manipulate the camera and obtain real-time feedback on the surgical field.

5.2 Electronic Hardware

5.2.1 Electronic System Architecture Overview

Fig. 5.1 presents an architecture block diagram of the camera electronic system. This system is mainly composed of two main subsystems: the internal camera and the external actuator, which are separated by the abdominal wall. Wireless control communication and video streaming between the two subsystems are successfully established, as depicted by the dashed lines in the diagram.

5.2.2 Internal Camera Board Design and Implementation

The internal camera's electronic system, as depicted in the bottom half of Fig. 5.1, revolves around a cc2541 wireless microcontroller unit (MCU). This low-power system-on-chip (SoC) solution is specifically designed for Bluetooth Low Energy

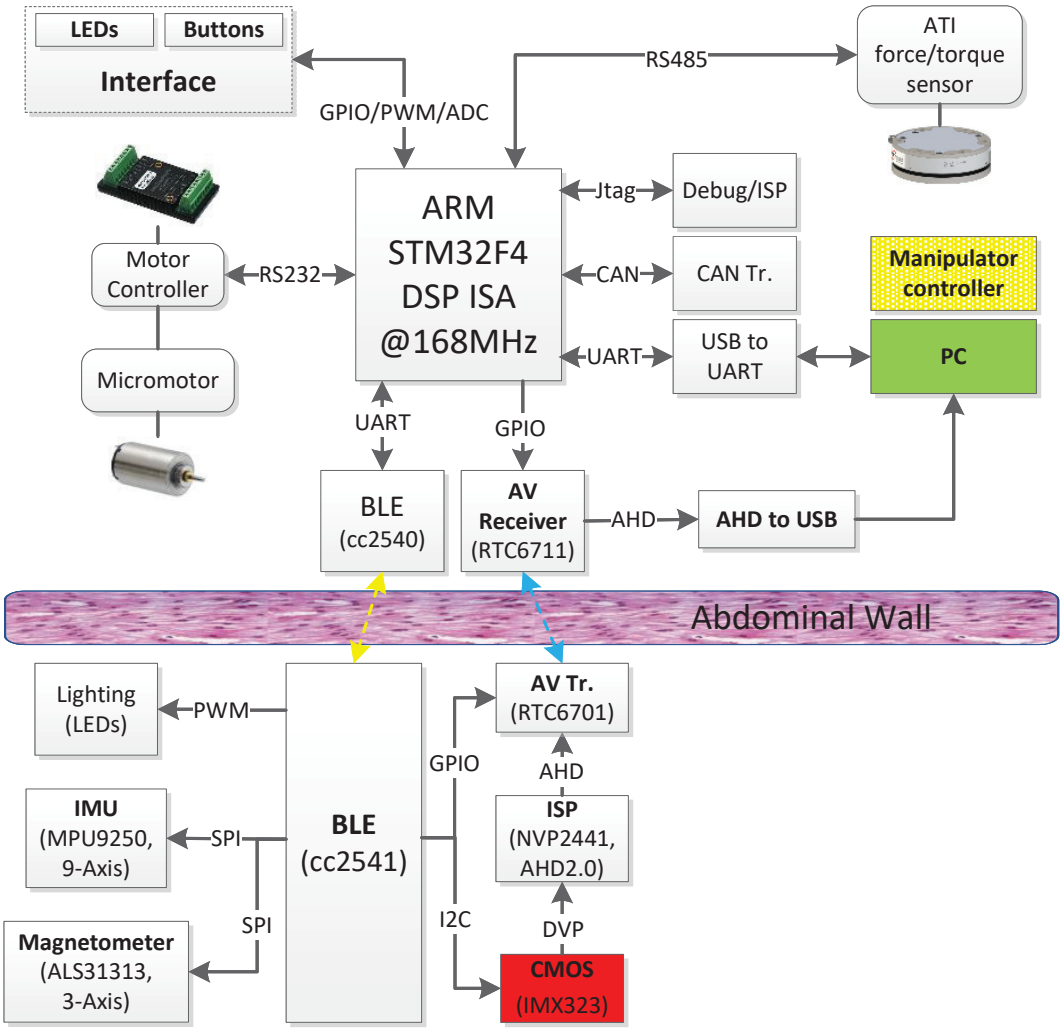

Figure 5.1: Overview of the electronic system architecture. The subsystem above the abdominal wall is the external actuator, while the bottom part is the internal camera. Wireless links including the BLE communication (yellow) and the AV transmission (blue) are indicated with dashed lines.

(BLE) applications, enabling wireless communication for camera control and managing all the onboard resources of internal camera including LEDs, sensors and AV transmission.

The imaging sensor captures images, which are then processed by the Image Signal Processor (ISP) to convert them from digital to analog format. These analog images are subsequently transmitted via an AV transmitter and an antenna. The cc2541 is responsible for online configuration and tuning of the imaging sensor using the I2C protocol, enhancing the camera's imaging performance. Additionally, the cc2541 is able to generates PWM signals to adjust the illumination strength of LED lights.

The cc2541 interfaces with an inertial measurement unit (IMU) and a magnetometer through the SPI interface, facilitating camera pose estimation. The design and implementation of the camera electronic system posed significant challenges, as all the onboard resources are constrained in a restricted space and have to maintain a low profile. The integration of these components onto two small PCB boards, connected by a flexible flat wire, is illustrated in Fig. 5.2. The figure also showcases the fabricated board and onboard power batteries, highlighting the successful implementation of the camera electronic system.

Wireless Communication Removing the onboard motors, a lightweight wireless MCU with essential on-chip peripherals is sufficient to manage the onboard resources and establish wireless communication. The feasibility of utilizing a 2.4GHz-based Zigbee solution for monitoring physiological parameters in the GI tract has been demonstrated in previous studies [90][91]. The TI cc2541, an SoC for BLE solutions, incorporates a 2.4GHz BLE compliant RF transceiver and other necessary peripherals, all integrated around a low-power 8051 microcontroller core. Packaged in a compact QFN format measuring $6mm \times 6mm$, it offers a minimum of 128KB programmable flash memory, making it a perfect option for the MCU of the internal camera. Additionally, the cc2541 features a built-in temperature sensor and a battery monitoring circuit, which allows for convenient monitoring of the battery and temperature within the system. To ensure efficient wireless communication, a

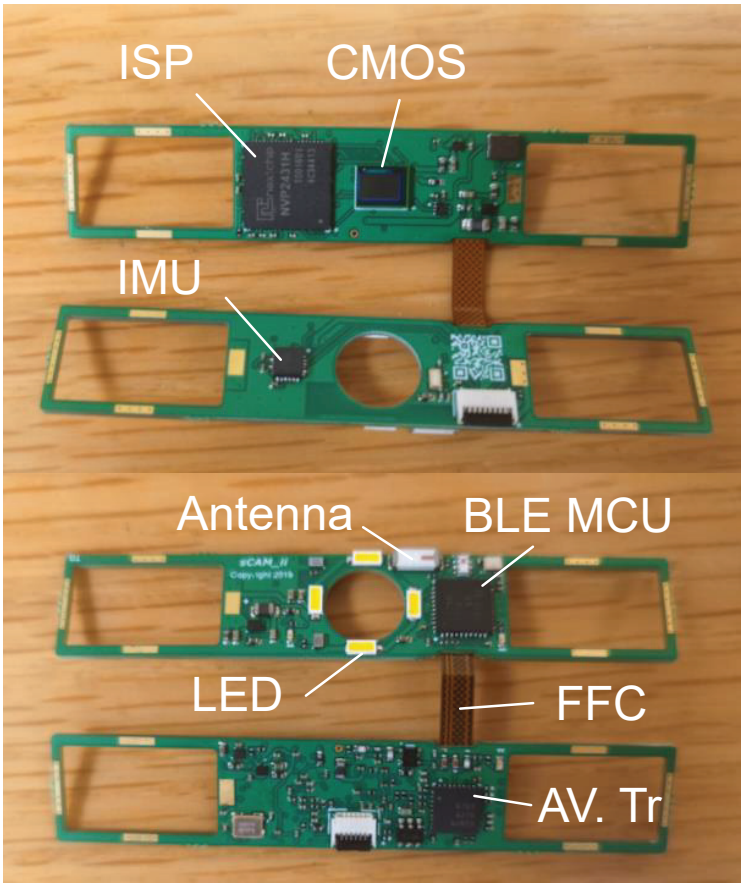

(a) Components on camera board.

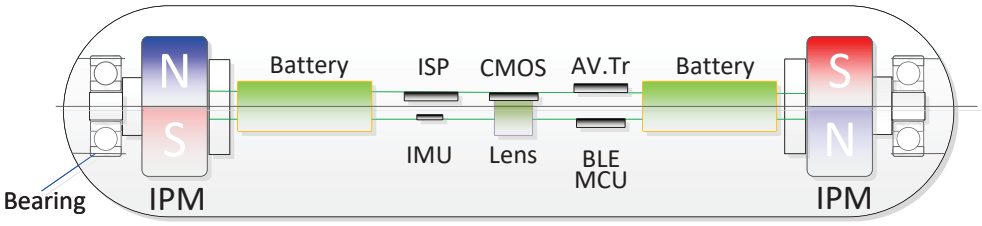

(b) Front view of the layout of the components.

Figure 5.2: Implementation and layout of camera onboard modules.

50Ω ceramic monopole chip antenna from Johanson Technology is employed.

Inertial and Magnetometer Sensors To enable closed-loop camera motion control and accurate pose tracking, the camera system incorporates inertial and magnetometer sensors. The chosen sensor unit is the MPU-9250 digital motion processing unit from InvenSense, which combines a triple-axis gyro and a triple-axis accelerometer in a compact $4 \times 4 \times 9mm$ QFN package. Additionally, the MPU-9250 includes an on-chip temperature sensor that can be accessed by the cc2541 MCU via the SPI interface, allowing for more precise estimation of the system temperature. Although the MPU-9250 features a built-in triple-axis magnetometer, it is unable to accurately calculate the yaw angle of the camera by relying solely on Earth's magnetic field as an absolute reference. This limitation is due to the strong magnetic field generated by the EPMs. To address this issue, a separate triple-axis magnetometer (ASL31313) is integrated into the camera system. This magnetometer has a measurement range of $\pm 100mT$ and a resolution of $0.05mT$ in each direction. It is specifically used to measure the magnetic fields generated by the EPMs. Further details regarding the localization process and the role of these sensors can be found in Chapter 3.

Imaging and Processing The choice of a digital imaging sensor is driven by the advantages it offers in terms of image quality and post-processing capabilities. The selected sensor for the camera system is the IMX323 from SONY, which is known for its superior low-light sensitivity, compact size ($7.55mm \times 5.75mm$), and high-quality digital imaging capabilities. This CMOS sensor, with a size of $1/2.9''$, provides HD1080p or HD720p video output and is accompanied by a low-profile all-plastic aspheric lens (DSL746, Sunnex) that offers a field of view of 60°. To facilitate transmission, the digital images captured by the sensor are first processed by an Image Signal Processor (ISP) (NVP2441, Nextchip Co,Ltd.). The ISP performs the necessary conversions to transform the digital images into analog composite video format. Additionally, the ISP provides various enhancement functions that

can improve the quality of the video output, further enhancing the overall imaging capabilities of the camera system.

AV Transmition The video transmitter module plays a critical role in the wireless camera system, and the RTC6701 2.4GHz FM transmitter has been carefully selected for its exceptional capabilities. This compact device, enclosed in a $5 \times 5mm$ QFN package, offers modulation of both video and audio signals, making it a versatile and efficient choice. Another key advantage of the RTC6701 is its flexibility in transmission settings. With four transmission frequency channels and two software-configurable output power levels, it provides adaptability to various operating environments and scenarios. To ensure effective transmission of the video and audio signals, a quarter wavelength wire antenna with a length of $30mm$ has been seamlessly integrated into the camera design. This antenna optimizes signal reception and transmission, resulting in stable and high-quality video streaming.

Illumination The illumination system of our laparoscopic camera is equipped with four high luminous flux LEDs sourced from TOSHIBA. These LEDs are strategically positioned on a circular layout, ensuring uniform distribution of light as depicted in Fig. 5.3. Each individual LED is designed to be low-profile, measuring $3.0 \times 1.4 \times 0.67mm$, and is capable of generating an impressive luminous flux of $22.9lm$ at a forward current of $65mA$. To accommodate the power requirements of the LEDs and optimize their performance, they have been organized into two parallel series. This configuration ensures efficient utilization of the onboard batteries, providing a reliable and consistent power supply to the illumination system. A distinctive feature is its adjustable illumination level. Unlike conventional insertable laparoscopes that typically offer simple on/off light control, our system allows for precise and continuous adjustment of the illumination intensity. Surgeons can manipulate the illumination level from zero to a maximum of $91.6lm$, corresponding to the combined output of all four LEDs ($4 \times 22.9lm$). This dynamic range of illumination empowers surgeons to actively optimize the imaging light based on the specific requirements of each surgical procedure, enhancing visibility and accuracy during operations.

Power Packs The onboard power system of our in vivo camera has been meticulously designed to ensure both reliability and safety. For this purpose, we have carefully selected six high-drain batteries, each with a compact size of $\phi 7.9 \times 2.6mm$. These batteries are FDA approved and boast an impressive capacity of $34mAh$ at a voltage of $1.55v$. To create a robust power source, these batteries have been organized into four parallel packs, providing a combined capacity of $204mAh$ at a nominal voltage of $4.65v$. This setup guarantees a steady and sufficient power supply to drive the entire camera's electronic components. Additionally, we have integrated two low-dropout (LDO) voltage regulators into the system to ensure a reliable current supply of $3.3v$ to power most of the onboard electronics. However, it's worth noting that the LEDs, which are integral to the illumination system, draw their power directly from the batteries.

5.2.3 External Actuator Board Design and Implementation

The design of the electronic system for the external actuator benefits from a larger available space and more resources compared to the internal camera system. In Fig. 5.1, the electronic system of the actuator is centered around a 32-bit ARM Cortex-M4 microcontroller (STM32F4). A cc2540 based Bluetooth Low Energy (BLE) module is connected to the STM32F4 processor through the UART serial port, enabling wireless control communication between the actuator and the camera. The STM32F4 processor is responsible for configuring the Audio-Video (AV) receiver using GPIO pins to support different operation frequencies of wireless AV transmission. The AV receiver receives the video signal, which can be accessed through an RCA connector and displayed for the surgeon's reference by the control unit.

For the tilt motion control of the camera, a motor controller board (MCDC 3002 S, FAULHABER) is integrated with the STM32F4 processor through RS232. This allows for closed-loop control of the tilt micromotor. Additionally, a two-axis joystick can be plugged in and connected to the analog-to-digital converter (ADC) of

the STM32F4 processor, enabling manual control of the camera's tilt motion. The actuator also includes several LEDs that provide emergency alerts and indicate the system's status for safety concerns. The external actuator communicates with the control unit via a mini USB port, facilitating data transfer and control between the actuator and the control unit.

Fig. 5.3 illustrates the AV Receiver board and the component layout on the Actuator board. The cc2540 BLE module is designed as a USB dongle with a compact package, allowing it to be soldered onto the actuator PCB for actuator-camera communication or plugged into a computer for BLE development and debugging. The actuator board is powered by an external 24V DC power supply.

The electronic system design for the external actuator has been strategically developed to leverage the advantages of a larger space and ample resources compared to the internal camera system. Key components of the actuator system include a powerful 32-bit ARM Cortex-M4 microcontroller (STM32F4) as its central processing unit. This MCU orchestrates the operation and control of various functions within the actuator. Facilitating seamless wireless communication between the actuator and the camera is a cc2540 BLE module, which interfaces with the STM32F4 through the UART serial port. To support wireless AV transmission, the STM32F4 processor configures an AV receiver using GPIO pins.

The tilt motion control of the camera is skillfully managed by integrating a motor controller board (MCDC 3002 S, FAULHABER) with the STM32F4 through RS232. This setup enables closed-loop control of the tilt micromotor, providing accurate and responsive control of the camera's tilt angle. In addition to automated control, manual control is also provided via a two-axis joystick that connects to the analog-to-digital converter (ADC) of the STM32F4 processor. This feature allows the surgeon to have direct and intuitive control over the camera's tilt motion, adding an extra layer of flexibility during procedures.

Ensuring safety is paramount, the actuator incorporates several LEDs that serve as emergency alerts and indicate the system's status. This enables prompt responses

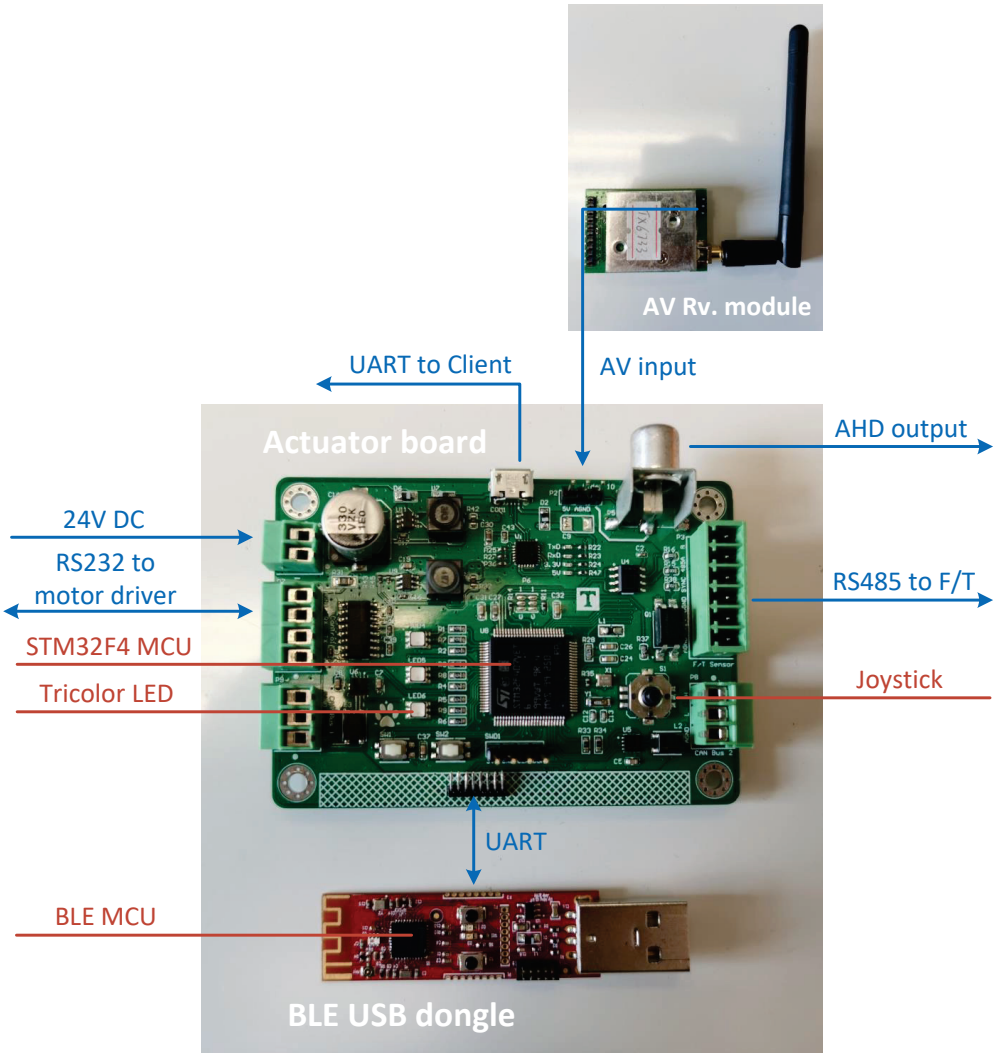

Figure 5.3: Implementation of the actuator board and AV receiver board

and heightened awareness of the system's operation during critical moments. Fig. 5.3 illustrates the AV Receiver board and the component layout on the Actuator board. The cc2540 BLE module is designed as a USB dongle with a compact package, allowing it to be soldered onto the actuator PCB for actuator-camera communication. Overall, the well-structured and thoughtfully designed actuator system, powered by an external 24V DC power supply, complements the camera system and contributes to the overall success and efficiency of the medical device.

5.3 Software

5.3.1 Bluetooth Low Energy (BLE) Communication and Profile

Bluetooth Low Energy (BLE), also known as Bluetooth Smart, is a component of the Bluetooth 4.0 standard designed for applications requiring low-power, low-latency, and low-throughput features. It is particularly suited for wireless healthcare and other energy-efficient applications. The use of frequency hopping across 40 channels defined by the Bluetooth protocol ensures resistance to RF interference and guarantees reliable connections. Texas Instruments (TI), as a member of the Bluetooth Special Interest Group (BT-SIG), has developed and provided their BLE stack and cc254x series wireless System-on-Chips (SoCs) for BLE application development. The camera system leverages Bluetooth Low Energy (BLE) technology for wireless communication and camera control. With the assistance of the TI BLE-Stack, a proprietary camera system application profile based on the Generic Attribute Profile (GATT) has been developed for seamless actuator-camera communication.

In the actuator-camera BLE connection, a central-peripheral role configuration is adopted, as depicted in Fig. 5.4. The cc2540 onboard the actuator serves as the central master, while the cc2541 onboard the camera operates as the peripheral slave. Upon power-up, the peripheral device periodically broadcasts advertisements until

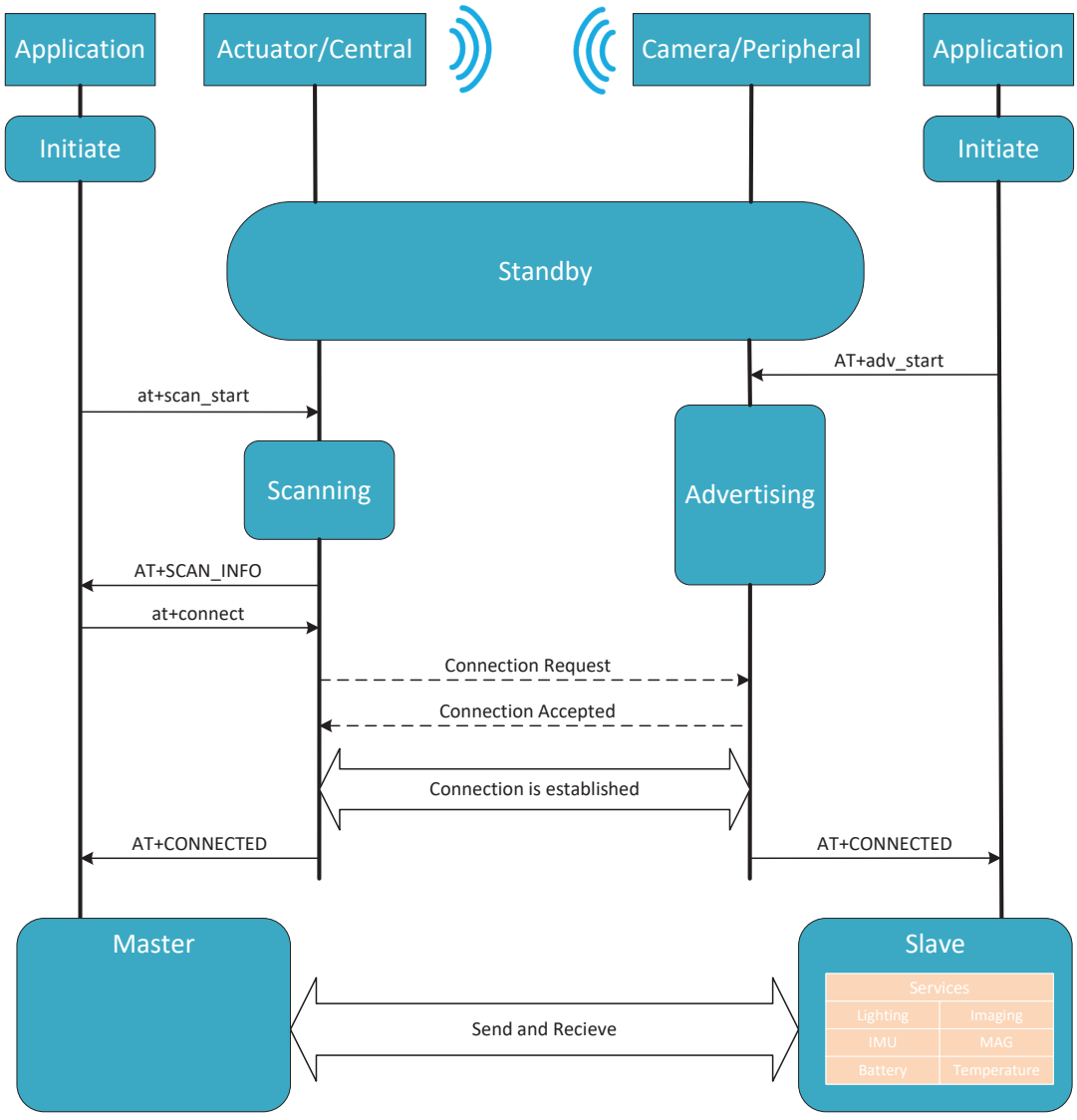

Figure 5.4: BLE profile and application flow chart.

a connection request is received from the central device. The central device, controlled by the STM32F4 microcontroller, communicates with the peripheral device via a UART serial port using AT commands, as illustrated in Fig. 5.1 and Fig. 5.4. The central device initiates a connection request to the peripheral device once it is detected. If the request is successfully accepted, a connection is established between the central and peripheral devices after a mutual parameter update. Subsequently, the central device functions as the data client, while the peripheral device operates as the data server. The peripheral device offers services related to the camera's onboard resources, such as lighting, imaging, IMU, magnetometer, temperature, and battery. The central device requests these services to enable wireless control of the camera. Importantly, multiple peripheral slave devices can be connected to a central master device, forming a star topology multi-camera network. This capability significantly enhances the system's overall functionality.

5.3.2 Architecture and Implementation of Real-Time Operating System (RTOS)

The selection of an appropriate real-time operating system (RTOS) is crucial for the successful development of the medical device. The system architecture diagram in Fig. 5.1 demonstrates that the STM32F4 ARM processor handles numerous low-level control and processing algorithms. These algorithms are too complex to be implemented within a single programming loop. Therefore, an RTOS becomes necessary to manage these tasks efficiently. In safety-critical applications like this, the timeliness of event responses is of utmost importance. Failure to respond within specified time constraints can lead to severe medical consequences. An RTOS, with its ability to schedule tasks and manage timing requirements, ensures that event responses occur within fixed time limits. This feature is crucial for the reliable operation of the medical device.

Another significant advantage of using an RTOS is the simplification of application programming and debugging. Developing software directly on a bare microcontroller unit (MCU) is time-consuming, error-prone, and often results in inefficient code. An RTOS supports multitasking, is time-sensitive, and provides system services and APIs that encapsulate hardware resources, streamlining software development.

To address these requirements, μC/OS-II from Micrium® (acquired by Silicon Labs® in 2016) was chosen as the embedded RTOS for the medical device. μC/OS-II is a lightweight and scalable RTOS known for its industrial-level reliability and application efficiency. Importantly, μC/OS-II has been extensively verified on various hospital devices used exclusively by medical professionals. These devices have successfully met the stringent medical software safety certification standard (IEC 62304) and obtained FDA (501k) clearance. The event-based preemptive multitasking kernel of μC/OS-II allows the scheduling of up to 256 tasks in real-time based on their statuses and priorities. As illustrated in Fig. 5.5, the RTOS resides on top of the hardware abstract layer (HAL) and efficiently manages all on-chip and onboard resources. The multitasking kernel enables the design of different functions of the sCAM as individual tasks, ensuring efficient utilization of the MCU resources. Furthermore, the modular nature of the RTOS facilitates the easy addition of new tasks in the future, if required.

Currently, six tasks have been developed to fulfill all the functions of the system: BLE communication task, USB communication task, joystick input processing task, AV receiver configuration task, DC motor control task, and LED task. Each task has been assigned a specific priority, and the RTOS kernel guarantees that the highest-priority task is executed promptly. Through careful priority assignment and task loop design, all tasks operate reliably and efficiently, mimicking the behavior of having dedicated CPUs for each task. Real-time event response and processing within fixed time constraints have thus been achieved, ensuring the reliability and safety of the running system.

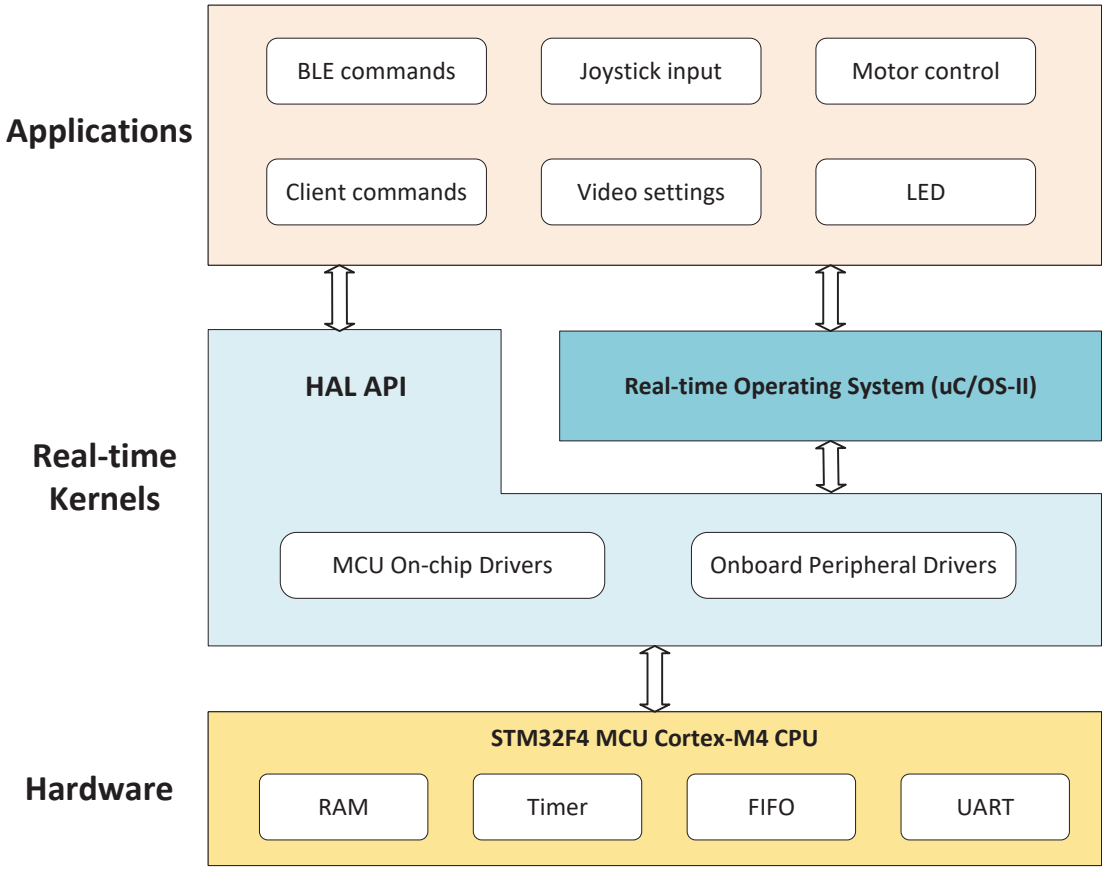

Figure 5.5: Real time framework.

5.4 Experiment Validation

5.4.1 Wireless Communication

The evaluation of tetherless camera control using BLE communication focused on two aspects: BLE profile services and received signal strength. In terms of BLE profile services, camera functions were implemented as individual services, including lighting, imaging, IMU, magnetometer, battery, and temperature. Each service had specific data bytes that could be accessed and manipulated by the BLE central device on the stator. The evaluation results confirmed the effective control of camera functions using these BLE services, demonstrating the successful implementation of tetherless camera control.

To assess the quality and stability of the BLE connection, the Received Signal Strength Indicator (RSSI) values were measured and recorded on the BLE central device. These values indicate the strength of the received BLE signal and were graphed as shown in Fig. 5.6. The camera was placed inside an enclosed synthetic abdomen model, while the actuator was positioned outside. The RSSI values at different actuator-camera distances provided insights into the radiation characteristics of the BLE signals and the overall connection stability. It was observed that all RSSI values were larger than $60dBm$ when the actuator-camera distance was $50mm$, indicating a strong and stable connection. This finding highlights the reliable nature of BLE communication and reinforces the importance of maintaining proximity between the actuator and camera during clinical applications.

5.4.2 Video Transmission

The experiment platform for evaluating the wireless video transmission capabilities of the laparoscopic surgical camera is depicted in Fig. 5.7. The camera was inserted through a trocar and positioned at the center of an abdomen model. A soft tissue suture pad was placed in the abdominal cavity to serve as a target for tracking. The

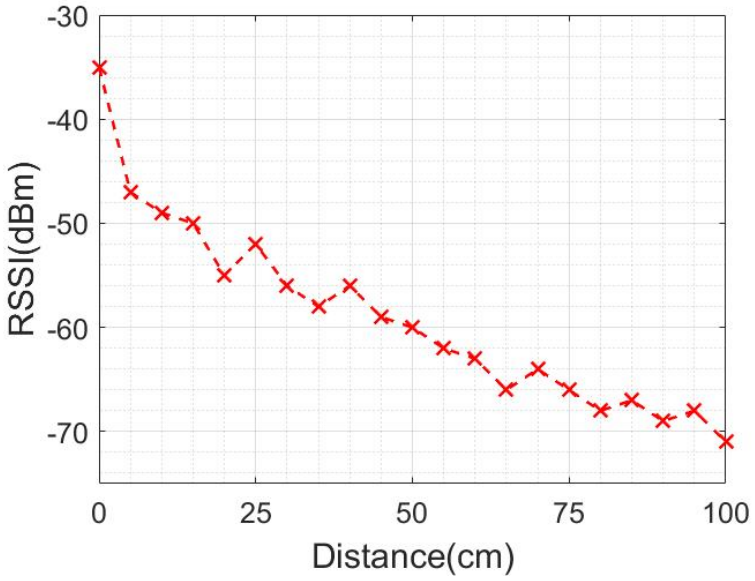

Figure 5.6: RSSIs with respect to actuator-camera distances.

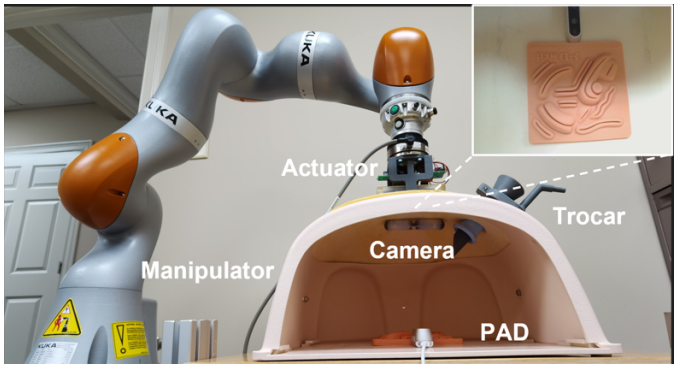

(a)

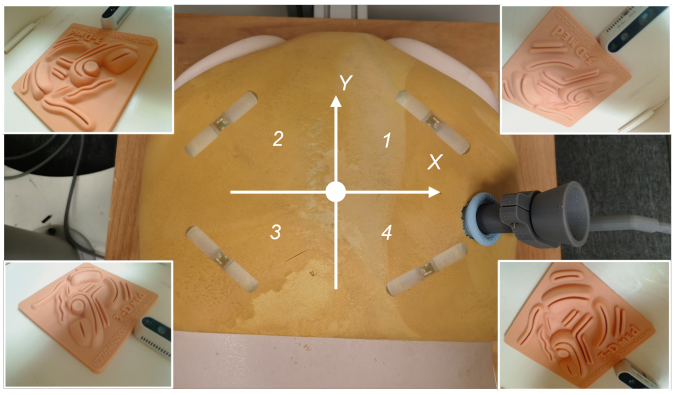

(b)

Figure 5.7: Wireless imaging performance test.

camera was then manipulated to capture desired field-of-views (FOVs) in each of the four quadrants. To receive the wireless video, an AV receiver was connected to the stator, and the received video signals were output to a video-to-USB converter (DFG/USB2pro) which was connected to the ECU (External Control Unit). The monitoring software and development APIs provided with the converter allowed for the display, processing, and storage of the received video streams.

During the test in the laboratory, no noticeable image distortion was observed by human eyes, indicating the high-quality transmission of the wireless video. The wireless connection remained stable throughout the 30-minute test duration. To assess the maximum signal coverage, the AV receiver was deliberately separated from the camera up to a distance of 10 meters, demonstrating the robustness and range of the wireless video transmission.

5.5 Summary

In this chapter, the design and implementation of the electronic systems for the internal camera and external actuator of the laparoscopic surgical camera have been presented. The evaluation encompassed two main aspects: BLE profile services accompanied by signal strength, and wireless video transmission.

Regarding BLE profile services, camera functions were implemented as individual services, enabling control and manipulation through the BLE central device. The successful implementation of these services demonstrated effective tetherless camera control. The evaluation of received signal strength provided insights into the quality and stability of the BLE connection. The Recorded Signal Strength Indicator (RSSI) values at different actuator-camera distances indicated a strong and stable connection, with all RSSI values exceeding $60dBm$ at a distance of $50mm$.

The wireless video transmission evaluation focused on the performance and stability of transmitting video wirelessly from the camera to the AV receiver. The results showed that the wireless video connection remained stable throughout the

30-minute test in the laboratory. No noticeable image distortion was observed, indicating reliable video transmission. Additionally, the AV receiver and camera were deliberately separated up to a distance of $10m$, demonstrating the maximum signal coverage.

Overall, the findings from this chapter validate the feasibility and effectiveness of tetherless camera control using BLE communication and high-quality wireless video transmission. The stable connection and absence of image distortion highlight the feasibility of utilizing wireless technology for video transmission in clinical applications.

Chapter 6

Conclusions and Future Work

6.1 Conclusions

This dissertation presents a groundbreaking fully insertable robotic laparoscopic surgical camera that eliminates the need for tethering wires. The camera system introduces wireless vision and control capabilities, along with non-contact transabdominal actuation, enabling a new level of freedom and flexibility in laparoscopic surgery. The robotic design and implementation of the camera system provide valuable references for the development of fully insertable medical devices and demonstrate the feasibility of an untethered fully insertable laparoscopic surgical camera.

The dissertation extensively explores the camera-tissue interaction process, addressing the challenges associated with force measurement. A non-invasive force measurement approach is proposed, implemented, and verified, allowing for accurate characterization of the camera-tissue contact force. The modeling and force analysis of the actuator-camera system are based on minimal kinematic or geometric assumptions, making the approach highly practical for clinical applications. Force measurement experiments confirm the effectiveness of the proposed approach, providing valuable insights into camera-tissue interaction dynamics.

Additionally, this work contributes an orientation estimation solution for the camera robot. By implementing a complementary filter specifically designed for this application, the camera's pose information is estimated. This marks a significant advancement as it enables the availability of pose information for a fully insertable laparoscopic surgical camera, facilitating closed-loop camera manipulation. Leveraging the force measurement and pose estimation, the dissertation realizes robotic-assisted closed-loop camera control within a double-loop control structure, allowing for shared autonomy between surgeons and the robotic controller. This approach ensures the precise maintenance of a comfortable laparoscopic view while guaranteeing surgical safety.

In summary, this dissertation introduces a revolutionary fully insertable robotic laparoscopic surgical camera, offering wireless vision and control capabilities, non-contact transabdominal actuation, and precise force measurement. The research outcomes provide valuable references for the development of fully insertable medical devices and validate the feasibility of untethered laparoscopic surgical cameras. The investigation of camera-tissue interaction, the proposed non-invasive force measurement approach, and the orientation estimation solution significantly contribute to enhancing the camera system's capabilities. The integration of force measurement and pose estimation enables robotic-assisted closed-loop camera control, ensuring a comfortable laparoscopic view with guaranteed surgical safety.

6.2 Future Work

The camera system described in the dissertation is currently in the proof-of-concept prototype stage, and its technical feasibility and functions have been successfully demonstrated through ex vivo experiments conducted in laboratory settings. However, before the camera system can be implemented in clinical practice, there are several open issues that need to be addressed. Future work will focus on

augmenting the developed prototype to overcome these challenges and improve its overall performance and usability.

Some of the key areas that require further attention and development include:

In vivo validation: The camera system needs to undergo rigorous in vivo testing to evaluate its performance and safety within a living organism. This will involve conducting experiments on animal models or human subjects to assess the camera's functionality, reliability, and compatibility with the surgical environment.

Biocompatibility: The materials and components used in the camera system must be biocompatible to ensure that they do not cause any adverse reactions or complications when in contact with biological tissues. Further research and testing are necessary to ensure the system's long-term biocompatibility and minimize the risk of tissue damage or inflammation.

Miniaturization and ergonomics: The size and ergonomics of the camera system should be optimized to facilitate easy insertion and maneuverability within the abdominal cavity. Efforts should be made to reduce the overall dimensions of the camera and improve its handling by surgeons, enhancing their dexterity and comfort during procedures.

System integration and reliability: The camera system should be seamlessly integrated with other surgical instruments and equipment, such as robotic surgical platforms or image-guided systems. Additionally, efforts should be made to enhance the system's reliability, robustness, and fault tolerance to ensure smooth operation during surgical procedures.

Clinical validation and regulatory approval: Extensive clinical trials and validation studies will be necessary to assess the camera system's efficacy, safety, and clinical outcomes. The system must comply with regulatory standards and obtain necessary approvals from regulatory bodies before it can be used in clinical practice.

User interface and control: The development of an intuitive user interface and control system is crucial to enable surgeons to effectively operate and manipulate

the camera system during surgery. The interface should provide real-time feedback, visualization, and precise control of the camera's movements.

Cost-effectiveness and scalability: Further research should focus on optimizing the cost-effectiveness of the camera system, making it affordable and accessible for a wide range of medical facilities. Scalability considerations should also be taken into account to enable mass production and widespread adoption of the technology.

In conclusion, while the dissertation's camera system has demonstrated promising results in laboratory settings, additional research and development efforts are required to address the open issues and advance the prototype toward clinical implementation. Future work will aim to overcome these challenges, enhance the system's performance, and ensure its readiness for real-world surgical applications.

Bibliography

[1] Stavros A Antoniou, George A Antoniou, Athanasios I Antoniou, and Frank-Alexander Granderath. Past, present, and future of minimally invasive abdominal surgery. *JSLS: Journal of the Society of Laparoendoscopic Surgeons*, 19(3), 2015. 1

[2] HS Himal. Minimally invasive (laparoscopic) surgery. *Surgical Endoscopy And Other Interventional Techniques*, 16:1647–1652, 2002. 1

[3] Prashanth P Rao, Pradeep P Rao, and Sonali Bhagwat. Single-incision laparoscopic surgery-current status and controversies. *Journal of minimal access surgery*, 7(1):6, 2011. 1

[4] SR Markar, A Karthikesalingam, S Thrumurthy, L Muirhead, J Kinross, and P Paraskeva. Single-incision laparoscopic surgery (sils) vs. conventional multiport cholecystectomy: systematic review and meta-analysis. *Surgical endoscopy*, 26:1205–1213, 2012. 1

[5] Michael F McGee, Michael J Rosen, Jeffrey Marks, Raymond P Onders, Amitabh Chak, Ashley Faulx, Victor K Chen, and Jeffrey Ponsky. A primer on natural orifice transluminal endoscopic surgery: building a new paradigm. *Surgical innovation*, 13(2):86–93, 2006. 1

[6] S Atallah, B Martin-Perez, D Keller, J Burke, and L Hunter. Natural-orifice transluminal endoscopic surgery. *Journal of British Surgery*, 102(2):e73–e92, 2015. 1

[7] Jeffrey Cadeddu, Raul Fernandez, Mihir Desai, Richard Bergs, Chad Tracy, Shou-Jiang Tang, Prashanth Rao, Mahesh Desai, and Daniel Scott. Novel magnetically guided intra-abdominal camera to facilitate laparoendoscopic single-site surgery: initial human experience. *Surgical endoscopy*, 23:1894–1899, 2009. 3, 5, 16

[8] Christian Di Natali, Jacopo Buzzi, Nicoló Garbin, Marco Beccani, and Pietro Valdastri. Closed-loop control of local magnetic actuation for robotic surgical instruments. *IEEE Transactions on Robotics*, 31(1):143–156, 2015. 3, 4

[9] Florence Leong, Alireza Mohammadi, Ying Tan, Denny Thiruchelvam, Pietro Valdastri, and Denny Oetomo. Magnetic interactions of neighbouring stator sets in multi dof local electromagnetic actuation for robotic abdominal surgery. In *2017 IEEE/RSJ International Conference on Intelligent Robots and Systems (IROS)*, pages 5723–5729. IEEE, 2017. 3, 4

[10] S Tognarelli, M Salerno, G Tortora, C Quaglia, P Dario, and A Menciassi. An endoluminal robotic platform for minimally invasive surgery. In *2012 4th IEEE RAS & EMBS International Conference on Biomedical Robotics and Biomechatronics (BioRob)*, pages 7–12. IEEE, 2012. 3, 17, 44, 45

[11] Irene Rivas-Blanco, Carmen López-Casado, Carlos Jesús Pérez-del Pulgar, F Garcia-Vacas, JC Fraile, and Victor Fernand Muñoz. Smart cable-driven camera robotic assistant. *IEEE Transactions on Human-Machine Systems*, 48(2):183–196, 2017. 3, 17

[12] Massimiliano Simi, Michele Silvestri, Carmela Cavallotti, Monica Vatteroni, Pietro Valdastri, Arianna Menciassi, and Paolo Dario. Magnetically activated stereoscopic vision system for laparoendoscopic single-site surgery. *IEEE/ASME Transactions on Mechatronics*, 18(3):1140–1151, 2012. 5, 10, 17, 47, 78

[13] Stephen R Platt, Jeff A Hawks, and Mark E Rentschler. Vision and task assistance using modular wireless in vivo surgical robots. *IEEE Transactions on Biomedical Engineering*, 56(6):1700–1710, 2009. 5, 10, 17, 47, 78

[14] Massimiliano Simi, N Tolou, P Valdastri, JL Herder, Arianna Menciassi, and P Dario. Modeling of a compliant joint in a magnetic levitation system for an endoscopic camera. *Mechanical Sciences*, 3(1):5–14, 2012. 5

[15] Nicolo Garbin, Piotr R Slawinski, Gregorio Aiello, Christina Karraz, and Pietro Valdastri. Laparoscopic camera based on an orthogonal magnet arrangement. *IEEE Robotics and Automation Letters*, 1(2):924–929, 2016. 5, 17, 44

[16] Beccani Marco, Susilo Ekawahyu, Natali Christian Di, and Valdastri Pietro. Smac—a modular open source architecture for medical capsule robots. *International Journal of Advanced Robotic Systems*, 11(11):188, 2014. 5

[17] Amy C Lehman, Jason Dumpert, Nathan A Wood, Lee Redden, Abigail Q Visty, Shane Farritor, Brandon Varnell, and Dmitry Oleynikov. Natural orifice cholecystectomy using a miniature robot. *Surgical endoscopy*, 23:260–266, 2009. 5

[18] Ning Li, Gregory J Mancini, and Jindong Tan. Hardware design for a cable-free fully insertable wireless laparoscopic robotic camera. In *2016 38th Annual International Conference of the IEEE Engineering in Medicine and Biology Society (EMBC)*, pages 5128–5131. IEEE, 2016. 5, 17, 18, 44, 78

[19] Ning Li, A Reza Yazdanpanah, Gregory J Mancini, and Jindong Tan. Initial design and results of an untethered insertable laparoscopic robotic surgical camera system. In *2017 IEEE International Conference on Robotics and Biomimetics (ROBIO)*, pages 959–964. IEEE, 2017. 5, 10, 17, 18, 44, 47, 78

[20] Nele Famaey, Erik Verbeken, Stefan Vinckier, Bert Willaert, Paul Herijgers, and Jos Vander Sloten. In vivo soft tissue damage assessment for applications in surgery. *Medical engineering & physics*, 32(5):437–443, 2010. 6, 17

[21] Chengli Song, Afshin Alijani, Tim Frank, GB Hanna, and Alfred Cuschieri. Mechanical properties of the human abdominal wall measured in vivo during insufflation for laparoscopic surgery. *Surgical Endoscopy And Other Interventional Techniques*, 20:987–990, 2006. 9

[22] H Xin, JS Zelek, and H Carnahan. Laparoscopic surgery, perceptual limitations and force: A review. In *First Canadian student conference on biomedical computing*, volume 144. Queen's University Kingston, ON, Canada, 2006. 9

[23] Xiaolong Liu, Gregory J Mancini, and Jindong Tan. Design and analysis of a magnetic actuated capsule camera robot for single incision laparoscopic surgery. In *2015 IEEE/RSJ International Conference on Intelligent Robots and Systems (IROS)*, pages 229–235. IEEE, 2015. 10, 17, 18, 44, 47, 78

[24] Haris Mateen, Rubel Basar, Afaz Uddin Ahmed, and Mohd Yazed Ahmad. Localization of wireless capsule endoscope: A systematic review. *IEEE Sensors Journal*, 17(5):1197–1206, 2017. 10, 48

[25] Amir Raeisi Nafchi, Shu Ting Goh, and Seyed A Reza Zekavat. Circular arrays and inertial measurement unit for doa/toa/tdoa-based endoscopy capsule localization: Performance and complexity investigation. *IEEE Sensors Journal*, 14(11):3791–3799, 2014. 10, 48

[26] Rohit Chandra, Anders J Johansson, and Fredrik Tufvesson. Localization of an rf source inside the human body for wireless capsule endoscopy. In *Proceedings of the 8th International Conference on Body Area Networks*, pages 48–54, 2013. 10

[27] Federico Carpi, Nathan Kastelein, Michael Talcott, and Carlo Pappone. Magnetically controllable gastrointestinal steering of video capsules. *IEEE Transactions on Biomedical Engineering*, 58(2):231–234, 2010. 10

[28] Trung Duc Than, Gursel Alici, Steven Harvey, Graeme O'Keefe, Hao Zhou, Weihua Li, Trent Cook, and Sharon Alam-Fotias. An effective localization method for robotic endoscopic capsules using multiple positron emission markers. *IEEE Transactions on Robotics*, 30(5):1174–1186, 2014. 10, 48

[29] Alexandros Karargyris and Anastastios Koulaouzidis. Odocapsule: next-generation wireless capsule endoscopy with accurate lesion localization and video stabilization capabilities. *IEEE Transactions on Biomedical Engineering*, 62(1):352–360, 2014. 10, 48

[30] Lok Yi Wu and CC Foo. Single-incision laparoscopic surgery: an update of current evidence. *Annals of Laparoscopic and Endoscopic Surgery*, 2016. 16

[31] Christian Di Natali, Tommaso Ranzani, Massimiliano Simi, Arianna Menciassi, and Pietro Valdastri. Trans-abdominal active magnetic linkage for robotic surgery: Concept definition and model assessment. In *2012 IEEE International Conference on Robotics and Automation*, pages 695–700. IEEE, 2012. 17, 44

[32] Benjamin S Terry, Zachary C Mills, Jonathan A Schoen, and Mark E Rentschler. Single-port-access surgery with a novel magnet camera system. *IEEE transactions on biomedical engineering*, 59(4):1187–1193, 2012. 17, 44, 45, 47

[33] Truman Cheng, Weibing Li, Calvin Sze Hang Ng, Philip Wai Yan Chiu, and Zheng Li. Visual servo control of a novel magnetic actuated endoscope for uniportal video-assisted thoracic surgery. *IEEE Robotics and Automation Letters*, 4(3):3098–3105, 2019. 17, 44, 78

[34] Mark Runciman, Ara Darzi, and George P Mylonas. Soft robotics in minimally invasive surgery. *Soft robotics*, 6(4):423–443, 2019. 18

[35] Fionnuala Connolly, Panagiotis Polygerinos, Conor J Walsh, and Katia Bertoldi. Mechanical programming of soft actuators by varying fiber angle. *Soft Robotics*, 2(1):26–32, 2015. 18

[36] Yahya Elsayed, Augusto Vincensi, Constantina Lekakou, Tao Geng, CM Saaj, Tommaso Ranzani, Matteo Cianchetti, and Arianna Menciassi. Finite element analysis and design optimization of a pneumatically actuating silicone module for robotic surgery applications. *Soft Robotics*, 1(4):255–262, 2014. 18

[37] Kit-Hang Lee, Denny KC Fu, Martin CW Leong, Marco Chow, Hing-Choi Fu, Kaspar Althoefer, Kam Yim Sze, Chung-Kwong Yeung, and Ka-Wai Kwok. Nonparametric online learning control for soft continuum robot: An enabling technique for effective endoscopic navigation. *Soft robotics*, 4(4):324–337, 2017. 18

[38] Benjamin Gorissen, Michael De Volder, and Dominiek Reynaerts. Chip-on-tip endoscope incorporating a soft robotic pneumatic bending microactuator. *Biomedical microdevices*, 20:1–7, 2018. 18

[39] Yingtian Li, Joseph Peine, Margherita Mencattelli, Jiaole Wang, Junhyoung Ha, and Pierre E Dupont. A soft robotic balloon endoscope for airway procedures. *Soft Robotics*, 9(5):1014–1029, 2022. 18

[40] Wenqi Hu, Guo Zhan Lum, Massimo Mastrangeli, and Metin Sitti. Small-scale soft-bodied robot with multimodal locomotion. *Nature*, 554(7690):81–85, 2018. 18

[41] Donghoon Son, Hunter Gilbert, and Metin Sitti. Magnetically actuated soft capsule endoscope for fine-needle biopsy. *Soft robotics*, 7(1):10–21, 2020. 18

[42] Lan N Pham, Jake A Steiner, Kam K Leang, and Jake J Abbott. Soft endoluminal robots propelled by rotating magnetic dipole fields. *IEEE Transactions on Medical Robotics and Bionics*, 2(4):598–607, 2020. 18

[43] Truman Cheng, Xue Zhang, Calvin Sze Hang Ng, Philip Wai Yan Chiu, and Zheng Li. Design and evaluation of a soft-bodied magnetic anchored and guided endoscope. *Journal of Medical Robotics Research*, 3(03n04):1841007, 2018. 18, 78

[44] Mark A Talamini, S Chapman, S Horgan, and William Scott Melvin. A prospective analysis of 211 robotic-assisted surgical procedures. *Surgical Endoscopy and Other Interventional Techniques*, 17:1521–1524, 2003. 19

[45] Long Qian, Jie Ying Wu, Simon P DiMaio, Nassir Navab, and Peter Kazanzides. A review of augmented reality in robotic-assisted surgery. *IEEE Transactions on Medical Robotics and Bionics*, 2(1):1–16, 2019. 19

[46] Ning Li, Gregory J Mancini, Amy Chandler, and Jindong Tan. Recovering stress distribution on deformable tissue for a magnetic actuated insertable laparoscopic surgical camera. In *2021 IEEE International Conference on Robotics and Automation (ICRA)*, pages 12314–12320. IEEE, 2021. 25, 62, 80

[47] Nicola Di Lorenzo, Livia Cenci, Massimiliano Simi, Claudio Arcudi, Valeria Tognoni, Achille Lucio Gaspari, and Pietro Valdastri. A magnetic levitation robotic camera for minimally invasive surgery: Useful for notes? *Surgical endoscopy*, 31(6):2529–2533, 2017. 46

[48] Jihad H Kaouk, Riccardo Autorino, Fernando J Kim, Deok Hyun Han, Seung Wook Lee, Sun Yinghao, Jeffrey A Cadeddu, Ithaar H Derweesh, Lee Richstone, Luca Cindolo, et al. Laparoendoscopic single-site surgery in urology: worldwide multi-institutional analysis of 1076 cases. *European urology*, 60(5):998–1005, 2011. 46

[49] Young-Sam Choi, Kwang-Sik Shin, Jin Choi, Ji-No Park, Yun-Sang Oh, and Tae-Eel Rhee. Single-port access laparoscopy-assisted vaginal hysterectomy: our initial experiences with 100 cases. *Minimally invasive surgery*, 2012, 2012. 46

[50] Matthew Kroh, Kevin El-Hayek, Steven Rosenblatt, Bipan Chand, Pedro Escobar, Jihad Kaouk, and Sricharan Chalikonda. First human surgery with a novel single-port robotic system: cholecystectomy using the da vinci single-site platform. *Surgical endoscopy*, 25(11):3566, 2011. 46

[51] Muhammad Ali Karim, Jamil Ahmed, Moustafa Mansour, and Abdulmajid Ali. Single incision vs. conventional multiport laparoscopic cholecystectomy: a comparison of two approaches. *International Journal of Surgery*, 10(7):368–372, 2012. 47

[52] Mark E Rentschler, Jason Dumpert, Stephen R Platt, K Lagnemma, Dmitry Oleynikov, and Shane M Farritor. Modeling, analysis, and experimental study of in vivo wheeled robotic mobility. *IEEE Transactions on Robotics*, 22(2):308–321, 2006. 47

[53] Giuseppe Tortora, Paolo Dario, and Arianna Menciassi. Array of robots augmenting the kinematics of endocavitary surgery. *IEEE/ASME transactions on mechatronics*, 19(6):1821–1829, 2014. 47

[54] Sara L Best and Jeffery A Cadeddu. Development of magnetic anchoring and guidance systems for minimally invasive surgery. *Indian journal of urology: IJU: journal of the Urological Society of India*, 26(3):418, 2010. 47

[55] Massimiliano Simi, Gianluca Sardi, Pietro Valdastri, Arianna Menciassi, and Paolo Dario. Magnetic levitation camera robot for endoscopic surgery. In *Robotics and Automation (ICRA), 2011 IEEE International Conference on*, pages 5279–5284. IEEE, 2011. 47

[56] M Silvestri, T Ranzani, A Argiolas, M Vatteroni, and A Menciassi. A multi-point of view 3d camera system for minimally invasive surgery. *Sensors and Actuators A: Physical*, 202:204–210, 2013. 47

[57] Haibo Feng, Dinghui Dong, Tengfei Ma, Jinlei Zhuang, Yili Fu, Yi Lv, and Liyi Li. Development of an in vivo visual robot system with a magnetic anchoring mechanism and a lens cleaning mechanism for laparoendoscopic single-site surgery (less). *The International Journal of Medical Robotics and Computer Assisted Surgery*, 2017. 47

[58] Cristian A Castro, Sara Smith, Adham Alqassis, Thomas Ketterl, Yu Sun, Sharona Ross, Alexander Rosemurgy, Peter P Savage, and Richard D Gitlin. Marvel: A wireless miniature anchored robotic videoscope for expedited laparoscopy. In *Robotics and Automation (ICRA), 2012 IEEE International Conference on*, pages 2926–2931. IEEE, 2012. 47

[59] Tie Hu, Peter K Allen, and Dennis L Fowler. In-vivo pan/tilt endoscope with integrated light source. In *Intelligent Robots and Systems, 2007. IROS 2007. IEEE/RSJ International Conference on*, pages 1284–1289. IEEE, 2007. 47

[60] P Valdastri, C Quaglia, E Buselli, A Arezzo, N Di Lorenzo, M Morino, A Menciassi, and P Dario. A magnetic internal mechanism for precise orientation of the camera in wireless endoluminal applications. *Endoscopy*, 42(06):481–486, 2010. 47

[61] Daniel J Mirota, Masaru Ishii, and Gregory D Hager. Vision-based navigation in image-guided interventions. *Annual review of biomedical engineering*, 13:297–319, 2011. 48

[62] Peter Mountney, Danail Stoyanov, and Guang-Zhong Yang. Three-dimensional tissue deformation recovery and tracking. *IEEE Signal Processing Magazine*, 27(4):14–24, 2010. 48

[63] Toby Collins and Adrien Bartoli. 3d reconstruction in laparoscopy with close-range photometric stereo. In *MICCAI (2)*, pages 634–642. Citeseer, 2012. 48

[64] Max Allan, Steve Thompson, Matthew J Clarkson, Sébastien Ourselin, David J Hawkes, John Kelly, and Danail Stoyanov. 2d-3d pose tracking of rigid instruments in minimally invasive surgery. In *International Conference on Information Processing in Computer-assisted Interventions*, pages 1–10. Springer, 2014. 48

[65] Weibing Li, Truman Cheng, Minxin Ye, Calvin Sze Hang Ng, Philip Wai Yan Chiu, and Zheng Li. Kinematic modeling and visual servo control of a soft-bodied magnetic anchored and guided endoscope. *IEEE/ASME Transactions on Mechatronics*, 25(3):1531–1542, 2020. 48, 78

[66] Trung Duc Than, Gursel Alici, Hao Zhou, and Weihua Li. A review of localization systems for robotic endoscopic capsules. *IEEE Transactions on Biomedical Engineering*, 59(9):2387–2399, 2012. 48

[67] Arthur W Mahoney and Jake J Abbott. Five-degree-of-freedom manipulation of an untethered magnetic device in fluid using a single permanent magnet with application in stomach capsule endoscopy. *The International Journal of Robotics Research*, 35(1-3):129–147, 2016. 48, 79

[68] Addisu Z Taddese, Piotr R Slawinski, Keith L Obstein, and Pietro Valdastri. Closed loop control of a tethered magnetic capsule endoscope. *Robotics science and systems: online proceedings*, 2016, 2016. 48, 79

[69] Bruno Scaglioni, Luca Previtera, James Martin, Joseph Norton, Keith L Obstein, and Pietro Valdastri. Explicit model predictive control of a magnetic flexible endoscope. *IEEE robotics and automation letters*, 4(2):716–723, 2019. 48, 79

[70] Duc Minh Pham and Syed Mahfuzul Aziz. A real-time localization system for an endoscopic capsule using magnetic sensors. *Sensors*, 14(11):20910–20929, 2014. 48

[71] Shuang Song, Baopu Li, Wan Qiao, Chao Hu, Hongliang Ren, Haoyong Yu, Qi Zhang, Max Q-H Meng, and Guoqing Xu. 6-d magnetic localization and orientation method for an annular magnet based on a closed-form analytical model. *IEEE Transactions on Magnetics*, 50(9):1–11, 2014. 48, 49

[72] Katie M Popek, Thomas Schmid, and Jake J Abbott. Six-degree-of-freedom localization of an untethered magnetic capsule using a single rotating magnetic dipole. *IEEE Robotics and Automation Letters*, 2(1):305–312, 2016. 48

[73] Christian Di Natali, Marco Beccani, and Pietro Valdastri. Real-time pose detection for magnetic medical devices. *IEEE Transactions on Magnetics*, 49(7):3524–3527, 2013. 48, 49

[74] Christian Di Natali, Marco Beccani, Nabil Simaan, and Pietro Valdastri. Jacobian-based iterative method for magnetic localization in robotic capsule endoscopy. *IEEE Transactions on Robotics*, 32(2):327–338, 2016. 49, 55

[75] Christopher J Fisher. Using an accelerometer for inclination sensing. *AN-1057, Application note, Analog Devices*, pages 1–8, 2010. 55

[76] James Diebel et al. Representing attitude: Euler angles, unit quaternions, and rotation vectors. *Matrix*, 58(15-16):1–35, 2006. 61

[77] Andrew J Petruska and Jake J Abbott. Optimal permanent-magnet geometries for dipole field approximation. *IEEE transactions on magnetics*, 49(2):811–819, 2012. 62

[78] Edward P Furlani. *Permanent magnet and electromechanical devices: materials, analysis, and applications*. Academic press, 2001. 62

[79] G Ciuti, R Donlin, P Valdastri, Alberto Arezzo, A Menciassi, Mario Morino, and P Dario. Robotic versus manual control in magnetic steering of an endoscopic capsule. *Endoscopy*, pages 148–152, 2009. 77

[80] Etern S Park, Jonathan W Shum, Tuan G Bui, R Bryan Bell, and Eric J Dierks. Robotic surgery: a new approach to tumors of the tongue base, oropharynx, and hypopharynx. *Oral and Maxillofacial Surgery Clinics*, 25(1):49–59, 2013. 77

[81] Stefan Mattheis, Pia Hasskamp, Laura Holtmann, Christina Schäfer, Urban Geisthoff, Nina Dominas, and Stephan Lang. Flex robotic system in transoral robotic surgery: the first 40 patients. *Head & neck*, 39(3):471–475, 2017. 78

[82] Marco Salerno, Rocco Rizzo, Edoardo Sinibaldi, and Arianna Menciassi. Force calculation for localized magnetic driven capsule endoscopes. In *2013 IEEE International Conference on Robotics and Automation*, pages 5354–5359. IEEE, 2013. 78

[83] O Onafeko and AR Reece. Soil stresses and deformations beneath rigid wheels. *Journal of Terramechanics*, 4(1):59–80, 1967. 80

[84] Tatsuro Muro. Tractive performance of a driven rigid wheel on soft ground based on the analysis of soil-wheel interaction. *Journal of Terramechanics*, 30(5):351–369, 1993. 80

[85] Mingjing Jiang, Yongsheng Dai, Liang Cui, and Banglu Xi. Experimental and dem analyses on wheel-soil interaction. *Journal of Terramechanics*, 76:15–28, 2018. 80

[86] Mark E Rentschler. *In vivo abdominal surgical robotics: Tissue mechanics modeling, robotic design, experimentation, and analysis*. The University of Nebraska-Lincoln, 2006. 80

[87] A Reza Yazdanpanah, Xiaolong Liu, and Jindong Tan. Modeling and analysis of a laparoscopic camera's interaction with abdomen tissue. In *2017 IEEE International Conference on Robotics and Automation (ICRA)*, pages 4227–4232. IEEE, 2017. 80, 81

[88] Yuan-cheng Fung. *Biomechanics: mechanical properties of living tissues*. Springer Science & Business Media, 2013. 81

[89] Susan Standring, H Ellis, J Healy, D Johnson, A Williams, P Collins, and C Wigley. Gray's anatomy: the anatomical basis of clinical practice. *American journal of neuroradiology*, 26(10):2703, 2005. 81

[90] Pietro Valdastri, Arianna Menciassi, Alberto Arena, Chiara Caccamo, and Paolo Dario. An implantable telemetry platform system for in vivo monitoring of physiological parameters. *IEEE Transactions on Information Technology in Biomedicine*, 8(3):271–278, 2004. 94

[91] Pietro Valdastri, Stefano Rossi, Arianna Menciassi, Vincenzo Lionetti, Fabio Bernini, Fabio A Recchia, and Paolo Dario. An implantable zigbee ready telemetric platform for in vivo monitoring of physiological parameters. *Sensors and Actuators A: Physical*, 142(1):369–378, 2008. 94

Vita

Hui Liu was born in Wuan, Hebei, China in 1993. He received the Bachelor degrees in Mechanical Engineering from Southwest Jiaotong University, China in 2015. He received his Master degree in Mechanical Engineering at Beihang University, China in 2018. In August 2018, he joined Dr. Jindong Tan's lab at University of Tennessee, Knoxville and became a Ph.D. candidate later in 2019. He worked as graduate teaching and research assistant during his Ph.D research. He graduated with a Doctor of Philosophy degree in Mechanical Engineering in August 2023.